

DIGITAL ACCESS TO SCHOLARSHIP AT HARVARD
DASH.HARVARD.EDU

HARVARD LIBRARY


Spatial Dynamics of the Bacterial Cell Wall Synthesis Machinery

Citation

Kapoor, Mrinal. 2017. Spatial Dynamics of the Bacterial Cell Wall Synthesis Machinery. Doctoral dissertation, Harvard University, Graduate School of Arts & Sciences.

Link

http://nrs.harvard.edu/urn-3:HUL.InstRepos:41142074

Terms of use

This article was downloaded from Harvard University's DASH repository, and is made available under the terms and conditions applicable to Other Posted Material (LAA), as set forth at

https://harvardwiki.atlassian.net/wiki/external/NGY5NDE4ZjgzNTc5NDQzMGIzZWZhMGFlOWI2M2EwYTg

Accessibility

https://accessibility.huit.harvard.edu/digital-accessibility-policy

Share Your Story

The Harvard community has made this article openly available.
Please share how this access benefits you. Submit a story

Spatial dynamics of the bacterial cell wall synthesis machinery

A dissertation presented

by

Mrinal Kapoor

to

The Department of Molecular and Cellular Biology

in partial fulfillment of the requirements

for the degree of

Doctor of Philosophy

in the subject of

Biology

Harvard University

Cambridge, Massachusetts

May 2017

© 2017 Mrinal Kapoor

All rights reserved.

Dissertation Advisor: Professor Ethan C. Garner Mrinal Kapoor

Spatial dynamics of the bacterial cell wall synthesis machinery

Abstract

The bacterial cell wall is a polymeric meshwork that is essential for cell shape. Cytoskeletal filaments spatially organize cell wall synthesis during growth and division. In this thesis, I first provide an introduction to cytoskeletal filaments in bacteria: I review the biochemistry of self-organizing machines that play crucial roles in subcellular organization, in the coordination of cell wall synthesis and DNA segregation, and in fundamental cellular processes like cell growth and division.

Next, I detail my study of the subcellular dynamics of the peptidoglycan synthesis machinery in *Escherichia coli and Bacillus subtilis*, finding that peptidoglycan biogenesis is carried out by two semi-autonomous systems – the Rod system, organized to move circumferentially around the rod-shaped cell by mobile filaments of MreB, and class A penicillin-binding proteins (aPBPs), which appear spatially unorganized, in comparison. This study also identified a new peptidoglycan polymerase, RodA, which is a part of the Rod system.

In the last chapter, I detail my studies of the contributions of these two systems to cell growth and cell shape, finding that the balance between them determines the diameter of *B. subtilis* cells, and that class B penicillin-binding proteins and RodA may also act outside the Rod system.

TABLE OF CONTENTS

Acknowledgements……...v

Chapter 1
An introduction to cell shape and the bacterial cell wall…….1

Chapter 2
An overview of self-organizing filament systems in bacteria…….8

Chapter 3
Two spatially distinct cell wall synthesis machineries……..…29

Chapter 4
Control of cell diameter in *Bacillus subtilis*……..…44

Chapter 5
Conclusion and future directions…….……..64

Appendix
Supplementary materials for Chapter 3…….……70
Supplementary materials for Chapter 4…….……..……104

References…….……..……....119

ACKNOWLEDGEMENTS

I would like to thank:

- My family.

- My adviser, Professor Ethan Garner, for his guidance and support.

- Members of my Quals and DAC committees: Professors Daniel Kahne, Thomas Bernhardt, Andrew Murray, Michael Laub, Richard Losick, and Daniel Needleman.

- My colleagues from the Garner Lab, and in particular, Dr. Ye Jin Eun, Dr. Carl Wivagg, and Mike Dion for their patience, knowledge, assistance, encouragement, and tutelage.

- Collaborators on various projects, especially Dr. Hongbaek Cho and Dr. Zachary Barry.

- The MCO administrative staff: Michael Lawrence, Patricia Perez, Debbie Maddalena, and Fanuel Muindi.

CHAPTER 1

An introduction to cell shape and the bacterial cell wall

The shape of a bacterial cell is determined by its cell wall - a meshwork-structure that in a vast majority of species is made of the heteropolymer peptidoglycan, also known as murein (Typas et al. 2012). Bacterial cell morphogenesis is therefore intimately tied to the process of cell wall synthesis; indeed, several cell wall synthesis genes were originally identified as cell shape-determining elements (Typas et al. 2012; Eun et al. 2015). The traditional view of these genetic determinants of shape placed significant emphasis on epigenetic contributions as well: it was held that the genetic program could only create and propagate the encoded cellular morphology in the context of the morphology itself (Harold 2007). It was proposed that spatial cues might be provided either by the existing rod shape of the cell, the curvature of the cell membrane, or by the old cell wall serving as a template for new synthesis (Harold 2007; Höltje 1998). Recently, however, particular emphasis has been placed on the organizational roles of cytoskeletal proteins found in bacteria that bear structural resemblance to eukaryotic actin and tubulin (Rudner & Losick 2010; Errington 2003), and newer models of cell wall synthesis attribute significant organizing roles to them. The goal of the work described in this dissertation is to understand the roles of these cytoskeletal proteins, and in particular, to learn how cytoskeleton-mediated spatial organization of cell wall synthesis enzymes, and their synthetic output, affects the shape of the cell. Questions about the shape of individual cells have far-reaching impacts on fields ranging from cell physiology and growth to evolutionary biology and antibiotic discovery (Koch 2000; Young 2007; Young 2010; Cavalier-Smith 2014).

The cell wall is essential in almost all bacteria because it both helps the cell resist osmotic

pressure and is required for cell shape, thus serving as a prominent target for antibiotic research (McKenna 2013; Garber 2015). In the face of increasingly widespread antibiotic resistance, there has been renewed interest in the peptidoglycan synthesis pathway and its regulation: researching the mechanisms of synthesis enzymes and the functions of non-enzymatic proteins holds promise for the development of new antibiotics (Garber 2015; Ling et al. 2015).

An overview of peptidoglycan synthesis

The monomer unit of peptidoglycan in *Bacillus subtilis* and *Escherichia coli* is a disaccharide-pentapeptide molecule that is synthesized in a multi-step pathway in the cytoplasm (Typas et al. 2012). The final steps of the pathway culminate in the attachment of the disaccharide-pentapeptide to a lipid carrier in the cytoplasmic leaflet of the cell membrane to create Lipid II, which is then transported across the membrane (Typas et al. 2012).

Once Lipid II is flipped, two distinct chemical reactions are needed to polymerize it into peptidoglycan. First, Lipid II is polymerized into glycan chains by a transglycosylation reaction catalyzed by glycosyltransferase enzymes. Second, nascent glycan chains are inserted into the existing cell wall by transpeptidase enzymes that cross-link the peptides. Both *E. coli* and *B. subtilis* contain the following two types of cell wall synthase enzymes: (1) bifunctional enzymes known as class A Penicillin-Binding Proteins (henceforth referred to as aPBPs) that contain glycosyltransferase 51 (GT51) and transpeptidase domains, and (2) monofunctional enzymes known as class B Penicillin-Binding Proteins (bPBPs) that are transpeptidases. In addition, *E. coli* also contains a monofunctional glycosyltransferase enzyme that has a GT51 domain (Typas et al. 2012).

Peptidoglycan synthesis during vegetative growth of *E. coli* and *B. subtilis* is carried out

by two distinct multi-protein complexes: the Rod system synthesizes peptidoglycan along the cylindrical surface of the cell during elongation and the divisome create septal peptidoglycan during cytokinesis (Typas et al. 2012). Newly synthesized peptidoglycan is chemically distinguishable from mature peptidoglycan (De Pedro & Schwarz 1981); a suite of enzymes exist to modify and hydrolyze peptidoglycan for a variety of purposes ranging from modification of glycan strand length (Smith et al. 2000) to peptidoglycan recycling (Park & Uehara 2008).

In *B. subtilis,* the Rod system is organized by filaments of the actin homologue MreB (and its two paralogues Mbl and MreBH) (Jones et al. 2001). In addition, it contains bPBPs, as well as several widely conserved essential proteins (MreC, MreD, RodA, and RodZ) whose functions were unknown when this work began, but are known to be essential for rod shape (Fig. 1.1). The divisome, on the other hand, is organized by filaments of two different kinds: FtsZ (a tubulin homologue) and FtsA (an actin homologue). It also contains aPBPs, bPBPs, and several other accessory proteins of known and unknown function (Eun et al. 2015).

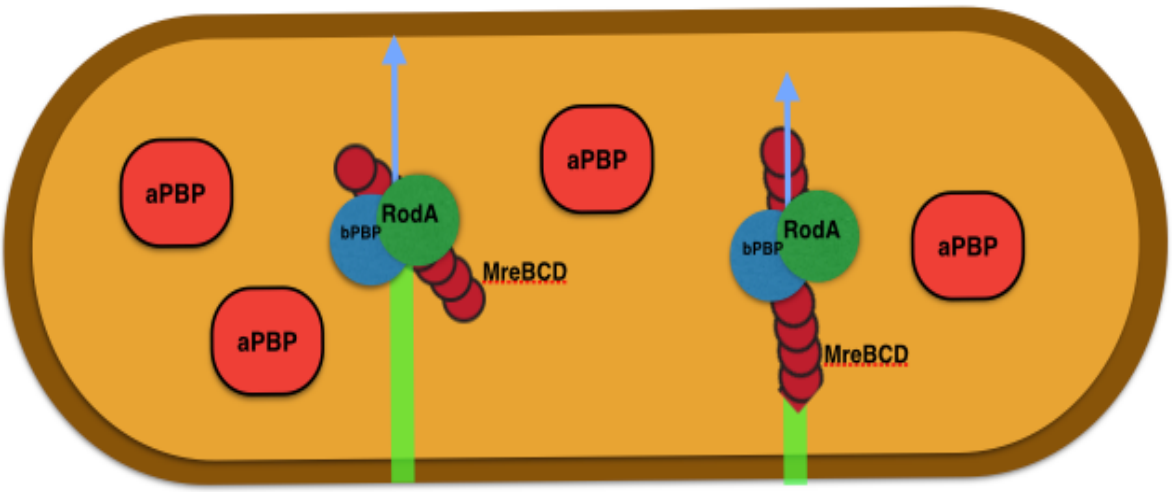


Figure 1.1. The Rod system synthesizes peptidoglycan during cell elongation. Diagram representing a rod-shaped bacterium enveloped in its rod-shaped sacculus. Depicted on the cell surface are aPBP enzymes, and some known members of the Rod complex: MreB filaments, bPBP enzymes, and shape determining proteins RodA, MreC, and MreD. The green stripes and blue arrows represent the circumferential path traversed by individual Rod complexes. aPBPs are spatially distinct from the Rod complex, although this model is debated (Cho et al. 2016; Pazos et al. 2017).

Spatial organization of peptidoglycan synthesis enzymes

Questions about the spatial organization of peptidoglycan synthesis remain the subject of debate, and are directly related to the issue of the architecture of peptidoglycan itself (Vollmer et al. 2008; Vollmer & Seligman 2010). While it is accepted that major differences exist between the gram-negative and gram-positive cell wall, several fundamental questions remain open. At the monomer length-scale, it is still not known how many disaccharides are contained in a single turn of the helical glycan chain. The orientation of the glycan chains themselves is also debated: the scaffold model posits that they run perpendicular to the cell membrane, while according to the layered model they run parallel to the cell membrane. The alignment of glycan strands in relation to each other is unknown; although a commonly accepted model shows them as parallel

hoops created perpendicular to the long axis of the rod-shaped cell, experimental evidence confirming this idea remains elusive (Vollmer et al. 2008; Vollmer & Seligman 2010).

Whatever the architecture of peptidoglycan may be, it must arise, at least in part, due to the spatial organization of the cell wall synthesis enzymes themselves (Höltje 1996; Höltje 1998). The Rod complex is key to this organization during cell elongation, and decades of study have shed light on the role played by MreB filaments. MreB was initially thought to be a long-range, helical cytoskeleton that provided mechanical support as well as physical/geographical cues to the cell wall biosynthetic process (Cabeen & Jacobs-Wagner 2010). The evidence for and against this hypothesis, as well as current ideas about the biophysical properties and functions of MreB are discussed in Chapter 2.

Is there collaboration between peptidoglycan synthesis enzymes?

The Rod complex contains several other widely conserved, essential, shape-determining proteins of unknown function. These include the single-pass transmembrane protein MreC; the polytopic integral membrane protein MreD; the single pass transmembrane protein RodZ, whose N-terminal cytoplasmic domain has been shown to interact with MreB, and whose C-terminal periplasmic domain is of unknown function, and the polytopic integral membrane protein RodA (Typas et al. 2012).

The function of RodA, which belongs to the widely conserved Shape Elongation Division and Sporulation (SEDS) family of proteins, has remained highly contentious. Although it has been shown to be required for rod shape and essential for viability, its precise biochemical function has been reported to be (1) a novel glycosyltransferase enzyme responsible for polymerization of glycan strands, (2) a flippase enzyme responsible for transport of Lipid II to

the outer leaflet of the cell membrane, or (3) a combination of these two activities (Meeske et al. 2016; Cho et al. 2016; Mohammadi et al. 2011; Emami et al. 2017).

In addition to these proteins, the Rod complex is thought to contain various aPBPs and bPBPs, which together perform the transglycosylation and transpeptidation of new peptidoglycan (Fay et al. 2010; Fraipont et al. 2011; Pazos et al. 2017). The precise contribution of these proteins, and why the Rod complex might contain biochemical redundancy between the transpeptidation activity of aPBPs and bPBPs, is currently unknown. Although the activity of PBPs has been demonstrated to have an impact on cell diameter, size, and shape (McPherson & Popham 2003; Henriques et al. 1998; Murray et al. 1998; Denome et al. 1999), we lack a detailed understanding how different PBPs modulate these parameters, and whether they function independently or are interdependent. As the cell grows, the cell wall must be constantly remodeled: synthesis and insertion of new material into the cell wall requires hydrolysis and breakdown of older material to create space (Typas et al. 2012). The kinetics of these two processes must be tied to the overall rate of cell growth in order to have robust growth without lysis (Koch 2000). Consistent with this idea, mutations in several important cell wall synthesis genes have been reported to cause defects in growth rate and fitness, and studying them remains a valuable resource in the search for novel, effective, antibiotics (McPherson & Popham 2003; Pazos et al. 2017).

Structure of this thesis

In Chapter 2, I provide an introduction to the biochemistry and biophysics of bacterial cytoskeletal filaments. By providing historical context, I demonstrate how MreB and FtsZ, in particular, play crucial roles in peptidoglycan synthesis during bacterial growth and division. This chapter has been adapted from a review article previously published in *Journal of Biological Chemistry*.

Chapter 3, adapted from a work previously published in *Nature Microbiology*, details a collaborative study (with Thomas Bernhardt's laboratory) that identified RodA as peptidoglycan polymerase, and provides support a unified view of the spatial organization of cell wall synthesis in gram-positive and gram-negative species.

Chapter 4 covers my unpublished work on the contributions of spatially organized (MreB associated) and unorganized (non-MreB associated) peptidoglycan synthesis to cell size, cell diameter, and cell growth.

Finally, Chapter 5 summarizes the findings of this thesis and describes important questions that remain open for future research.

CHAPTER 2

An overview of self-organizing filament systems in bacteria

This chapter was previously published as:

Y.-J. Eun*, M. Kapoor*, S. Hussain, E. C. Garner, Bacterial Filament Systems: Toward Understanding Their Emergent Behavior and Cellular Functions. *Journal of Biological Chemistry*. **290**, 17181–17189 (2015).

**These authors contributed equally to this work.*

Overview and motivation

The study of cell shape and cell wall synthesis has been greatly influenced by the discovery of cytoskeletal elements in bacteria. The existence of internal organization within bacterial cells, and evidence for the intimate involvement of filamentous structures in peptidoglycan synthesis posed a challenge to the traditional view that the only source of heritable structural information/templating for peptidoglycan synthesis is the sacculus itself.

This chapter provides a historical perspective on the discovery of these self-organizing filament systems, with a particular focus on their roles in DNA segregation, cell morphogenesis, and cell division.

Abstract

Bacteria use homologs of eukaryotic cytoskeletal filaments to conduct many different tasks, controlling cell shape, division, and DNA segregation. These filaments, combined with factors that regulate their polymerization, create emergent self-organizing machines. Here, we summarize the current understanding of the assembly of these polymers and their spatial

regulation by accessory factors, framing them in the context of being dynamical systems. We highlight how comparing the *in vivo* dynamics of the filaments to those measured *in vitro* has provided insight into the regulation, emergent behavior, and cellular functions of these polymeric systems.

Introduction

The use of fluorescent proteins changed our view of the bacterial cell – rather than being homogeneous mixtures, bacterial cells are spatially organized, placing components at specific locations. With the discovery that bacteria contain structural homologs of eukaryotic actin and tubulin (Erickson 1995; van den Ent et al. 2001), it was proposed that these polymers might have organizational and structural roles similar to their eukaryotic counterparts (Margolin 1998; Graumann & Defeu Soufo 2004).

The first homologs of the eukaryotic cytoskeleton discovered in bacteria are some of the most conserved. FtsZ is a tubulin that localizes to the cleavage plane and is essential for cell division (Bi & Lutkenhaus 1991). MreB is an actin distributed along the length of the cell, and it is essential in many bacteria for both rod-shape maintenance and elongation (Jones et al. 2001). Although these two proteins have less than 15% sequence identity to their eukaryotic counterparts, they show a high conservation of tertiary structure (van den Ent et al. 2001; Löwe & Amos 1998), and also hydrolyze and polymerize with the same nucleotides – FtsZ with GTP, and MreB with ATP (van den Ent et al. 2001; Mukherjee & Lutkenhaus 1994).

Filaments are also encoded by extra-chromosomal elements; low copy plasmids use polymers to bias segregation to both daughter cells. Examples include actins such as ParM found on *Escherichia coli* plasmids (Dam & Gerdes 1994), AlfA on *Bacillus subtilis* plasmids (Becker

et al. 2006), and many others (Derman et al. 2009). Additionally, tubulin homologs, like TubZ, have been found on *Bacillus* plasmids (Tinsley & Khan 2006). Even bacteriophages use tubulin filaments, such as PhuZ, to organize nascent phage particles to the host mid-cell (Kraemer et al. 2012).

We are all snowflakes: the diversity of bacterial polymers.

Ultra-structural studies of these distant homologs revealed that the actin and tubulin folds are capable of assembling into a wide variety of filaments. ParM forms two-stranded left-handed filaments (Orlova et al. 2007). AlfA forms large bundles composed of short, mixed-polarity, left-handed filaments (Polka et al. 2009). Unlike all other actins, MreB forms flat, anti-parallel protofilaments, with laterally adjacent monomers in register, rather than staggered (van den Ent et al. 2014).

Among tubulins, FtsZ forms short, single-stranded filaments (Romberg et al. 2001) that are straight or curved depending on conditions (Erickson et al. 1996), while PhuZ forms three-stranded filaments with a right-handed twist (Zehr et al. 2014). Interestingly, TubZ initially forms right-handed double filaments that transition into a four-stranded form following GTP hydrolysis (Montabana & Agard 2014).

In addition to the filaments listed above, there are many other families of bacterial filaments (extensively reviewed elsewhere (Cabeen & Jacobs-Wagner 2010)), including bactofilins, intermediate filament proteins, and metabolic enzymes. Collectively, these bacterial polymers have been termed the "prokaryotic cytoskeleton" (van den Ent et al. 2001; Cabeen & Jacobs-Wagner 2010), a phrase historically based on the structural homology of FtsZ and MreB to the eukaryotic actin and tubulin folds.

This review summarizes the current understanding of how these polymers behave in isolation, and also how they are spatially regulated by other factors to create emergent biological machines. We highlight how comparisons of polymer dynamics *in vitro* and *in vivo* have shed light on both the regulation and cellular function of these filaments. We start by reviewing "case studies" of the minimal plasmid-segregation systems and detail how the same approaches have been used to study FtsZ and MreB.

Easy to understand because there are only three things to look at.

Plasmid-segregation systems contain only three components; the dynamic properties of their filaments both in isolation and in combination with the other two components have been well characterized. These systems are single operons, encoding a polymer, a DNA-binding protein, and a centromeric DNA sequence. From these parts, *ParMRC* builds two structures: ParM filaments, and a ring-like kinetochore created by ParR binding to sequence repeats in *parC* (Møller-Jensen et al. 2007; Schumacher et al. 2007). Two pieces of *in vivo* and *in vitro* data suggested that ParR/*parC* modulates ParM dynamics to make a plasmid-segregating spindle. *In vivo*, long ParM filaments extend through the length of the cell with plasmids at each end. Filaments were visible only when there was more than one plasmid (Møller-Jensen et al. 2003). In contrast, ParM creates short, transient polymers *in vitro*. Assembly proceeds by rapid nucleation followed by growth from both ends. Filaments depolymerize from either end via hydrolysis-mediated dynamic instability (Garner et al. 2004). The discrepancy between the long, stable filaments *in vivo* and the short, unstable filaments *in vitro* was explained by combining all three components, which showed that ParR/*parC* stabilizes ParM filaments to the ATP state, inhibiting filament catastrophe at bound ends (Garner et al. 2007). This suggested that filaments,

stabilized at both ends, elongate by insertional polymerization (Garner et al. 2007) (Fig. 2.1, top spindles in b and c). The turnover of unattached filaments provides free monomers to favor growth at ParR/*parC.* A later study found that interactions between ParM filaments can also stabilize them (Gayathri et al. 2012), suggesting that two filaments, each attached to a single kinetochore, can form a productive spindle, elongating only at the ParR/*parC* bound ends (Fig. 2.1, bottom spindles in b and c). This study also observed that ParR/*parC* can bias the growth of ParM filaments assembled in AMPPNP to the ParR/*parC* bound end, a behavior noted in previous work (26). This biased growth led the authors to a model where 1) ParR/*parC* can bind to only one end of ParM filaments, and 2) like eukaryotic formins, ParR/*parC* increases the monomer on-rate at the bound end. However, this model creates a kinetic dilemma: ParR/*parC* accelerates polymerization of AMPPNP filaments only at the bound end (Gayathri et al. 2012), yet ATP ParM filaments ends elongate at the same rate (at both ends) both when they are free or ParR/*parC* bound (Garner et al. 2004; Garner et al. 2007; Petek & Mullins 2014). This rate of ATP filament elongation matches the rate of spindle elongation observed *in vivo* (Garner et al. 2007; Campbell & Mullins 2007). This kinetic discrepancy (which likely arises due to the difference in free monomer concentrations between the nucleotide conditions) remains to be resolved. The *TubZRC* system is remarkably similar to *ParMRC*, despite using a tubulin. First, the TubR/*tubC* kinetochore structure strongly resembles ParR/*parC* (Aylett & Löwe 2012). Second, TubZ polymers treadmill *in vivo* (Larsen et al. 2007), indicating they are also unstable, though less so than ParM. Third, TubR/*tubC* stabilizes polymers, allowing TubZ filaments to form beneath their normal critical concentration (Aylett & Löwe 2012) (Fig. 2.1).

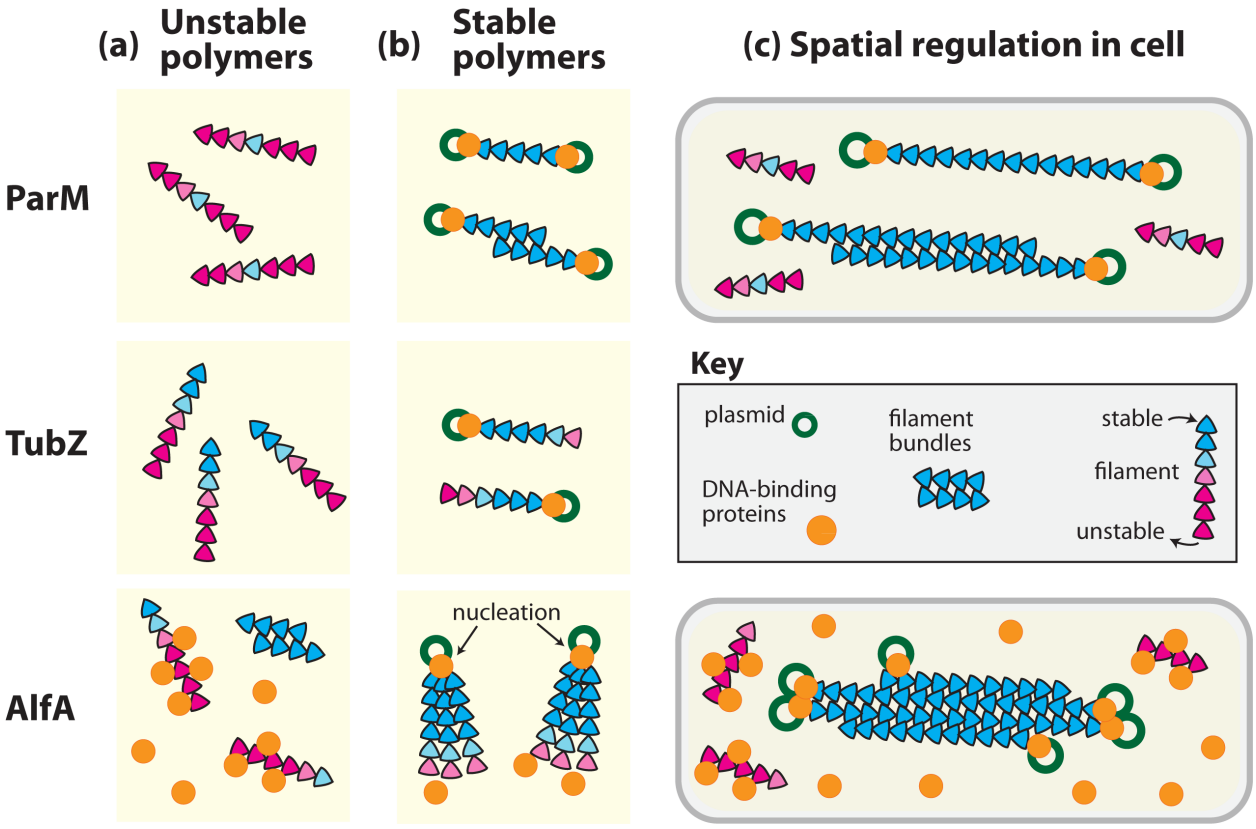


Figure 2.1. Summary of three-component plasmid segregation systems. A common theme among the ParM, AlfA, and TubZ spindles is the spatial regulation of polymer stability. (a) The polymers have differing degrees of inherent instability (stable in blue, unstable in red). ParM is dynamically unstable, TubZ treadmills, and AlfA is stable over minutes, although it is destabilized by free AlfB. (b) Polymers within the spindle are stabilized in two ways: 1) Interactions with the DNA-binding protein and plasmid DNA, and 2) Lateral interactions with neighboring filaments. (c) The native properties of each polymer combined with the regulation conferred by the other factors cause filaments in the spindle to be stable relative to those elsewhere in the cell, which favors filament elongation at kinetochores. The black arrows depict the direction of traveling plasmids.

The Alf system uses alternative means to achieve the same goal. It comprises the actin AlfA, the DNA-binding AlfB, and the *parN* centromere. *In vivo,* AlfA forms large filament bundles that recover from photobleaching from both ends of the bleached region (Becker et al. 2006). However, bundles formed *in vitro* are stable over several minutes (Polka et al. 2009). This difference can be explained by AlfB's opposing effects on AlfA: Free AlfB binds to the sides of AlfA filaments, inhibiting bundling and increasing filament turnover. In contrast, AlfB

complexed with *parN* nucleates AlfA filaments, which form stable bundles via lateral interactions. AlfB/*parN* also lowers the critical concentration of AlfA, favoring growth at *parN.* Reconstitution of all three components *in vitro* demonstrated that AlfB/*parN* complexes ride on the ends of elongating bundles, and also move along existing bundles in both directions. Continued growth at AlfB/*parN* is ensured by free AlfB repressing AlfA polymerization elsewhere in the cell (Polka et al. 2014) (Fig. 2.1).

In all the above cases, nucleation of these polymers by themselves is rapid and appears unregulated in space. Although the inherent polymer dynamics and regulation thereof vary greatly between these systems, they follow a common principle – the subset of filaments attached to the kinetochore are stabilized relative to free filaments. This allows the stable spindle to elongate using the monomer pool provided by the turnover of unattached filaments (Fig. 2.1). We wish to note that it is possible that nucleation may also occur at the kinetochores of all these systems. While AlfA is the only bacterial polymer found to be regulated by nucleation, it has not been proven that the other polymers are also nucleated at the plasmids.

Dear eukaryotic cytoskeleton: I may look like you, but I'm different.

Unlike the eukaryotic cytoskeleton, FtsZ and MreB do not directly impose cellular geometry themselves; they influence bacterial cell wall synthesis, a complex process involving many proteins (Typas et al. 2012). FtsZ and MreB in the cytoplasm control the activity of the cell wall-synthesizing enzymes on the opposite face of the membrane, defining the cellular location of cell wall synthesis and thus the shape of the cell (Fig. 2.2a and 2.3b). Therefore, to understand bacterial growth and division, we must understand how these filaments and their accessory factors function as complete systems.

FtsZ – The closer we look, the weirder it gets.

FtsZ is required for localization of all other proteins that form the 'divisome' (Adams & Errington 2009) (Fig. 2.2a). Divisome proteins assemble in a hierarchical, two-step fashion: 'early' and 'late'. Early proteins tether FtsZ to the membrane, and regulate its polymerization and structure. Late proteins synthesize the cell wall, and segregate any chromosomes trapped at the constriction (Adams & Errington 2009) (Fig. 2.2a).

In vivo, FtsZ can form multiple structures: A tight ring at the mid-cell (i.e. Z-ring), and shorter spirals or arcs near the division site (Michie et al. 2006). FtsZ was reported to form long helices spanning the cell length (Ma et al. 1996), but these structures are likely artifacts caused by conditions that increase polymer formation (Meier & Goley 2014); they appear when the cellular FtsZ levels are increased, or the rate of GTP hydrolysis is reduced (Addinall et al. 2005; Fu et al. 2010). It is currently thought that the Z-ring represents a productive divisome, and the shorter spirals/arcs may be less stable Z-rings or intermediates (Erickson et al. 2010).

Filament organization within the Z-ring is still under debate (Fig. 2.2b). Two contrasting models have resulted from multiple studies using super-resolution microscopy and cryo-EM. One model suggests FtsZ forms a continuous ring of connected filaments (Fu et al. 2010; Szwedziak et al. 2014). The other model holds that the Z-ring is composed of short (50-500 nm) filaments that are connected by a few lateral contacts, and are irregularly distributed around the division plane (Si et al. 2013; Holden et al. 2014; Li et al. 2007).

Z-rings are very dynamic and their turnover is regulated by GTP hydrolysis (Anderson et al. 2004; Geissler et al. 2007). The halftime for turnover of filaments *in vivo* (8-11s) is similar to that measured for filaments *in vitro* (3.5-7s) (Erickson et al. 2010).

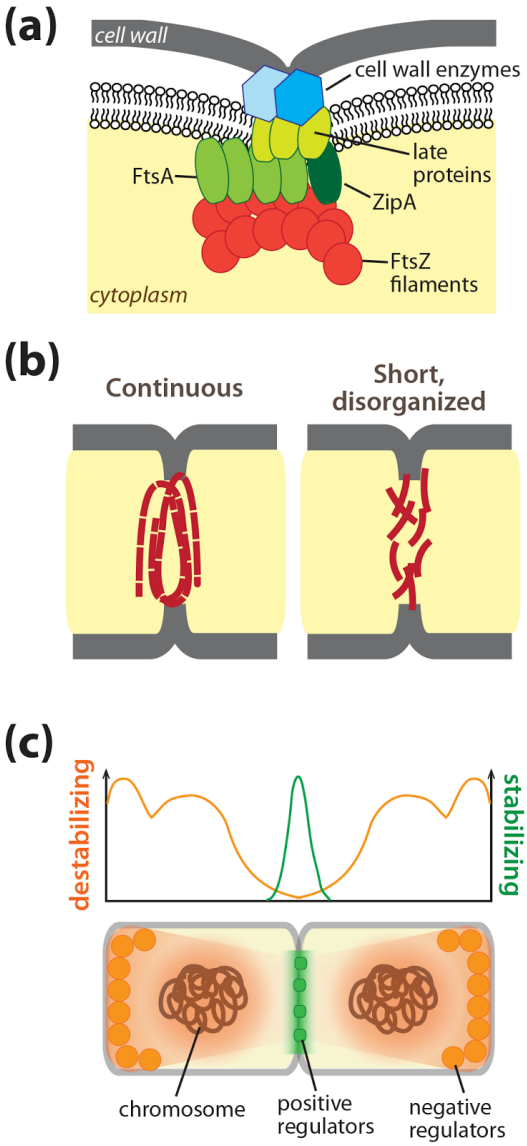


Figure 2.2. (a) Schematic of proteins at the division site. FtsZ polymers are anchored to the membrane through 'early' divisome proteins (e.g. ZipA and FtsA). Other early proteins (e.g. ZapA and FzlA) that stabilize the Z-ring are not shown. Subsequently, 'late' proteins (e.g. FtsKQLNBIW) including cell wall synthesis enzymes, arrive to continue divisome assembly. **(b) Two models of Z-ring structure.** The first model (left) suggests that FtsZ filaments form a continuous ring or compressed helix. The second model (right) proposes that the ring is made of short, disorganized polymers with a few lateral contacts. **(c) Spatial regulation of FtsZ polymerization in the cell.** Both positive and negative regulators are spatially organized in the cell to focus the Z-ring. The concentrations of regulators along the cell length are plotted, showing that destabilizing factors are located at the poles and over the chromosome, while stabilizing factors are at the division plane. This cartoon reflects the overall spatial organization in *E. coli* and *C. crescentus*.

Single molecule studies suggest that FtsZ monomers within the Z-ring are frozen in position for at least 3-4 seconds (Niu & Yu 2008). Combined, these results imply that each monomer is immobile for a substantial fraction of its lifetime in the Z-ring.

How accessory factors focus the Z-ring in space.

In vitro, FtsZ rapidly forms single-stranded filaments, 30-50 subunits long (Erickson et al. 2010). While these properties indicated FtsZ assembly is isodesmic (Romberg et al. 2001), polymerization is in fact cooperative; FtsZ monomers are first "activated" via GDP release and subsequently dimerize to form a nucleus for polymerization (Chen et al. 2005). These results indicate that FtsZ filaments alone should polymerize everywhere throughout the cytoplasm. Instead, cells create a precisely positioned and stable ring at the membrane, indicating the stability of FtsZ filaments must be spatially regulated in the cell.

Bacteria position their Z-ring with remarkable precision, within an error of 2.9% of the cell length in *E. coli* (Guberman et al. 2008). A properly positioned Z-ring must fulfill two criteria: it should not close around the nucleoid, and it should be positioned at the mid-cell. Both tasks are accomplished by negative regulation of polymerization. To avoid the nucleoid, bacteria use DNA-binding proteins, such as Noc and SlmA, that locally inhibit filament formation (Wu & Errington 2012) (Fig. 2.2c); Noc associates with both DNA and the membrane to physically block Z-ring formation. SlmA antagonizes FtsZ polymerization, although its exact mechanism of inhibition remains controversial (Wu & Errington 2012).

For the second task of finding the middle of the cell, cells create spatial gradients of depolymerizing factors – maximal at the poles, minimal at mid-cell (Fig. 2.2c). These gradients can be positioned in different ways. In *Caulobacter crescentus*, the FtsZ inhibitor MipZ

associates with ParB, which binds near the origin of replication on the chromosome. Before replication, MipZ is held only at one cell pole (Thanbichler & Shapiro 2006). As the DNA replicates, one origin segregates to the opposing pole, while the other remains in place. Positioning the MipZ maxima at poles creates a bipolar gradient minimal at the mid-cell, where the Z-ring forms(Thanbichler & Shapiro 2006). In contrast, in *E. coli,* the gradient establishes itself using a reaction-diffusion system (Loose et al. 2008). This system has three components: MinD is an ATPase that self-assembles on the membrane, and also binds the FtsZ depolymerizer MinC. MinE promotes ATP hydrolysis by MinD, causing it to detach from the membrane. Together, these activities cause all three components to oscillate between cell poles, creating a time-averaged minimum of MinC at mid-cell (Raskin & de Boer 1999).

Reconstitutions of MinCDE and FtsZ in three-dimensional cell-shaped compartments demonstrated that MinCDE together form a time-averaged bipolar gradient, confining FtsZ filaments to the middle region. Interestingly, this biochemical system responds to its surrounding geometry, creating multiple MinC minima in compartments of varying lengths (Zieske & Schwille 2014). These experiments show another result: Although confined, the filaments within these minima do not form a focused Z-ring, indicating that positive regulation is required for Z-ring formation.

Many proteins are known to stabilize FtsZ filaments (Fig. 2.2c). FtsA, which itself can form filaments (Szwedziak et al. 2012), is one of the few proteins known to bring FtsZ to membranes. *In vitro* reconstitutions have shown two effects of FtsA. First, it co-assembles with FtsZ polymers onto membranes. Second, shortly after co-assembly, FtsA destabilizes FtsZ, causing monomers to detach from the filaments (Loose & Mitchison 2014). These time-delayed properties cause FtsZ filaments to "move" in linear paths by treadmilling along the membrane, as

monomers remain immobile with respect to the treadmilling filament (Loose & Mitchison 2014).

Other membrane proteins, such as ZipA and ZapA, positively regulate FtsZ polymerization by reducing the rate of filament turnover. ZipA accomplishes this by promoting FtsZ bundling, as shown by reconstitution on lipid bilayers (Loose & Mitchison 2014). In another study, ZapA-mediated bundling protected FtsZ from the depolymerizing effects of MinC (Bisicchia et al. 2013).

Other proteins modulate the superstructure of FtsZ filaments. FzlA bends *C. crescentus* FtsZ into helical bundles, and in doing so, might contribute to the constriction of the septum (Goley et al. 2011). In *B. subtilis*, SepF makes rings and arcs that wrap around FtsZ filaments(Gundogdu et al. 2011), perhaps further anchoring FtsZ to the membrane (Duman et al. 2013).

We are just beginning to explore the effects of each individual divisome protein on FtsZ filaments. Future *in vitro* studies may reveal more complex behaviors when multiple regulators are combined. Deconvoluting the complexity of the divisome may be assisted by studying FtsZ dynamics *in vivo* in the absence of each factor; this could also be done at different stages of divisome maturation and Z-ring constriction.

How does the Z-ring divide the cell?

It is not known which component of the cell division machinery exerts the force required for division, but many models propose that it is FtsZ. Some models do not require a continuous Z-ring around the cell.

One early suggestion was that a change in FtsZ filament curvature upon GTP hydrolysis could pinch the cell (Lu et al. 2000). To test if this occurs *in vitro*, FtsZ was fused to a membrane

targeting sequence and encapsulated inside lipid tubes (Osawa et al. 2008). FtsZ rings formed within these tubes could slide along their length. When sliding rings coalesced, they slightly constricted the tubes (Osawa et al. 2008). However, follow-up studies cast doubt on this model, since membrane deformations occurred even when FtsZ could not hydrolyze GTP (Osawa et al. 2009; Osawa & Erickson 2011).

A second model proposes that FtsZ filaments are always more curved than the membrane they bind to, regardless of their nucleotide state. The repeated attachment of these short, bent filaments would deform the membrane, and the iterative local pinches could be coordinated by lateral interactions into a cell-scale constriction. This model was supported by studies showing that attachment of an artificial amphipathic helix to either side of the bent filament could deform liposomes in opposite directions (Osawa et al. 2009).

A third model is that the ring constricts by contiguous filaments sliding past each other, tightening like a coiling spring (Lan et al. 2009; Hörger et al. 2008). This model relies on the idea that the Z-ring is composed of long, continuous filaments. The energy driving constriction arises from increasing the number of lateral interactions as the rings further condense (Lan et al. 2009; Hörger et al. 2008). This model was supported by a recent cryo-EM study showing continuous rings of FtsA/FtsZ filaments going around the entire septa of both *E. coli* and *C. crescentus* (Szwedziak et al. 2014). Additionally, FtsA and FtsZ contained inside liposomes co-polymerized into filaments that encircled the inner face of the membrane. These filaments laterally associated, constricting the liposomes. The authors proposed that membrane constriction is initiated by the formation of a closed Z-ring and is continued by filaments sliding along with ongoing FtsA/FtsZ co-polymerization.

A fourth, divergent model proposes that FtsZ filaments do not exert force, but simply

serve as a scaffold to localize the cell wall enzymes to the septum. The enzymes could then orient their synthesis inward to divide the cell. Although this model is difficult to test, cell wall synthesis is required for cell division, as its inhibition via mutagenesis or antibiotics leads to incomplete constriction (Egan & Vollmer 2013). Furthermore, depletion of a endopeptidase (*dipM*) in *C. crescentus* causes pre-existing constrictions to relax, while FtsZ still remains at the division site (Poggio et al. 2010).

The two most frequently discussed models are 1) local bending by short filaments and 2) filament sliding within a continuous ring. When considered individually at its conceptual extreme, each model can be easily invalidated. For example, recent work has suggested that FtsZ filaments may be too flexible to bend membranes except at low surface tensions (Arumugam et al. 2012), calling into question the local bending model. Evaluating the other extreme, if filaments slide past each other, monomers should move across the septum, yet *in vivo* they are immobile (Niu & Yu 2008).

These models need not be exclusive, as the physical principles underlying each model may work together to divide the cell. The basis of the bending model is that membranes deform to match filament curvature. The basis of the sliding model is that increasing the lateral interactions induces constrictions (Kirchhausen 2012). It has recently been shown that local crowding of any membrane protein, even GFP, can induce membrane deformation (Stachowiak et al. 2012). These two forces may work together: Membrane constriction via local bending could be reinforced by lateral associations that further deform the membrane.

There is a remaining "energetic difficulty" with the filament sliding model (Erickson et al. 2010). To add even one more lateral bond, the filaments must break *all* existing lateral ones as they slide relative to each other. We suggest this difficulty may be resolved by the recent

observation of FtsA/FtsZ treadmilling (Loose & Mitchison 2014). This may reduce the energetic barrier for filaments to "move" relative to each other, increasing contacts via new growth without breaking existing bonds.

We also suggest that a similar, multi-model view can be taken regarding the filament structure within the Z-ring; it is possible that different filament organizations exist at each stage of divisome maturation and constriction.

MreB, the bacterial problem child.

Although MreB has been extensively studied, we know very little about the dynamics and cellular function of MreB filaments. In concert with a small group of other proteins, MreB both encodes and maintains the width (i.e. diameter) of rod-shaped bacteria as they elongate (Doi et al. 1988). Initial *in vivo* observations painted a picture of MreB that persisted for a decade: MreB was seen to form long, cell-spanning helices (Shih et al. 2005; Jones et al. 2001) (Fig. 2.3a). These helices were proposed to localize the cell wall synthesis enzymes, directing a helical pattern of cell wall growth (Daniel & Errington 2003).

Although the overall MreB helices appeared mostly static in Gram-negative bacteria, single molecule approaches in *C. crescentus* revealed that MreB monomers move linearly in both directions around the cell, traveling a short distance before dissociating (Kim et al. 2006). These motions, at the time, were attributed to monomers treadmilling through short filaments within a static helix. In *B. subtilis*, entire filaments were reported to move in helical tracks around the cell, a motion also attributed to polymer dynamics (Defeu Soufo & Graumann 2004).

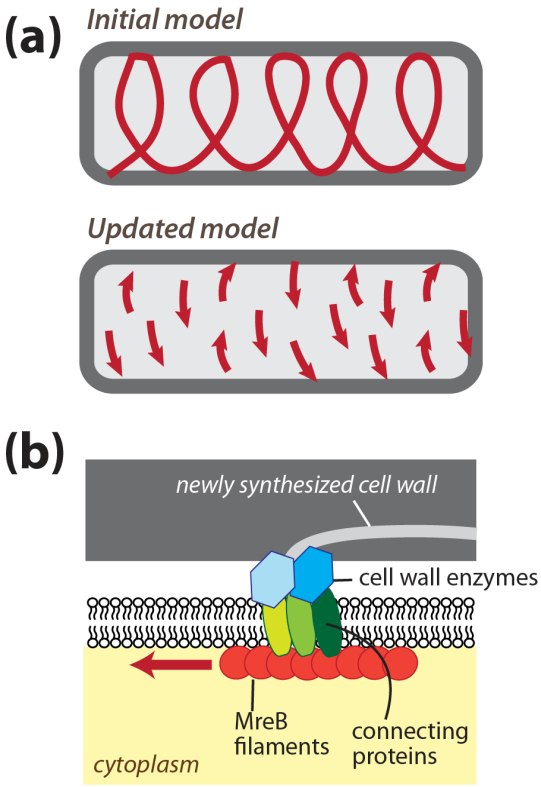


Figure 2.3. (a) Models of MreB polymer organization *in vivo*. The initial model proposed that MreB polymers make up a cell-spanning helix. The updated model suggests that disconnected polymers move circumferentially around the rod-shaped cell; their motions are otherwise uncoordinated. Moving MreB is shown as arrows. **(b) Schematic of proteins involved in elongation.** MreB filaments bind to the membrane and interact with peptidoglycan synthesis enzymes in the periplasm through transmembrane connector proteins. Cell wall synthesis drives MreB motion, indicated by the red arrow.

The observation of cell-spanning structures created by this actin homolog suggested that it might have cytoskeletal functions as well as a role in cell wall synthesis. It was proposed that MreB, like actin, could function as a polymerization motor to transport cargo (Graumann & Defeu Soufo 2004), or segregate newly replicated origins to the cell poles (Gitai 2005). MreB was also suggested to organize not only the proteins involved in cell wall synthesis, but many other unrelated proteins as well, as evidenced by co-localization and protein interaction studies (reviewed in (Chastanet & Carballido-Lopez 2012)).

Although MreB is notoriously difficult to work with *in vitro*, its assembly dynamics presented two features distinct from actin: Both its nucleation and its polymerization are rapid (Bean & Amann 2008; Mayer & Amann 2009), first forming short filaments that later coalesce into large bundles (Esue et al. 2006).

A series of recent findings has prompted a re-evaluation of our understanding of nearly every aspect of MreB: 1) its biochemical properties and assembly kinetics, 2) its *in vivo* structure and dynamics, and 3) its roles in the cell. This calls into question whether any analogies can be made between this prokaryotic filament and its eukaryotic doppelgänger.

First, it was discovered that MreB polymerizes on membranes, forming short, antiparallel filaments, rather than the bundles that form in solution (Salje et al. 2011; van den Ent et al. 2014). Not only does this finding explain why previous *in vitro* studies were stymied by protein aggregation (Nurse & Marians 2013), it also indicates that the results from these initial kinetic studies need to be reassessed.

Next, the "cell-spanning helix" was found to be an artifact. In *E. coli*, N-terminal fluorescent fusions gave rise to the static MreB helices, which were revealed to be large bundles when imaged by cryo-EM (Swulius et al. 2011). When the fluorophore was moved into an internal loop of MreB, no bundles were observed, and filaments could be seen to move across the cell (van Teeffelen et al. 2011). Further studies of MreB motion in *B. subtilis* indicated that MreB is a series of disconnected filaments that move radially around the cell circumference (Garner et al. 2011; Domínguez-Escobar et al. 2011; Reimold et al. 2013). These circumferential motions were found to be driven not by polymer dynamics, but by cell wall synthesis: They halt upon chemical inhibition or genetic depletion of the cell wall synthesis enzymes (van Teeffelen et al. 2011; Garner et al. 2011; Domínguez-Escobar et al. 2011), which themselves move around

the cell in the same manner as MreB (Garner et al. 2011; Domínguez-Escobar et al. 2011) (Fig. 2.3a).

Different lengths of MreB filaments *in vivo* have been reported: One study described small "patches" (Domínguez-Escobar et al. 2011) in *B. subtilis*, while another reported filaments up to 3 μm long (Reimold et al. 2013). These differences in length may arise from the expression level of MreB, or perhaps by the oligomerization caused by fluorescent fusions (see below). While the length of MreB filaments remains controversial, it has been shown that MreB filaments are disconnected. Two different studies indicated no coordination between filament motions along the cell length at any resolvable scale (Garner et al. 2011; Olshausen et al. 2013) (Fig. 2.3a).

Combined, these findings necessitate a reappraisal of the roles of MreB in the cell. As MreB forms short (relative to the cell length), uncoordinated filaments that move around the cell width, MreB must create shape locally, rather than at the cell-length scale. Furthermore, the other proposed cellular functions of MreB require re-evaluation: 1) Such filaments cannot spatially organize other cellular components over long distances, and 2) their polymerization cannot be harnessed to move cargo within in the cell, as they are extremely stable (Domínguez-Escobar et al. 2011), lack structural polarity (a feature that rules out directed filament growth) (van den Ent et al. 2014), and their cellular motions are driven by cell wall synthesis, not by polymerization (Garner et al. 2011).

Regulation of MreB.

As is the case with most biological filaments, the polymerization of MreB appears to be regulated. In *B. subtilis,* MreB filament association with the membrane is regulated via Lipid II,

the lipid-linked precursor for cell wall synthesis. If Lipid II levels are decreased, filaments disappear off the membrane (Schirner et al. 2014). While the factors mediating this process (or any other regulation) have not been identified, there are many candidates given the long list of proteins reported to be associated with MreB (Chastanet & Carballido-Lopez 2012). However, many of these interactions were assayed using fluorescence colocalization – often with the artifactual MreB "helix" – and thus warrant re-examination. Furthermore, it was found that MreB is a common contaminant in affinity pulldowns (Rueff et al. 2014), indicating that many interactions identified by immunoprecipitation or affinity-tags may also be suspect.

Like the divisome and FtsZ, proteins that interact with MreB - including MreC, MreD, RodA, and RodZ (Chastanet & Carballido-Lopez 2012) - may regulate filament levels. Of these, RodZ is an appealing regulatory candidate because its cytoplasmic domain has been crystallized with MreB (van den Ent et al. 2010), and expression of this domain alone can partially restore cell shape and MreB localization in *rodZ*-null cells (Muchová et al. 2013). Other candidates have been found, but require further study. These include DapI, a cell wall synthesis enzyme in *B. subtilis* that interacts with cytoplasmic MreB (Rueff et al. 2014), and MbiA, a protein in *C. crescentus* that affects cell shape by interacting with MreB, although its biological function remains unknown (Yakhnina & Gitai 2012).

How does MreB define cell width?

It remains a mystery how this disconnected system of rotating filaments imparts a robust width to rod-shaped cells. These filaments influence the insertion of cell wall locally, yet uniformly over long distances, giving a constant radius along the cell length.

Some studies have used MreB mutants to approach this question. By examining *C. crescentus* with MreB mutated near the ATP-binding site, Dye and colleagues found that alterations in MreB polymerization dynamics affect its cellular distribution, which then affects the shape of the cell (Dye et al. 2011). One of these MreB mutants created irregularly shaped cells, fat in some areas and very thin in others. This mutant MreB preferentially localized to the thinner regions of the cell, causing those areas to elongate while the other regions bulged (Harris et al. 2014). This led to the proposal that MreB filaments serve to maintain the cell radius, not to encode it.

Any bends or defects in a growing rod-shaped bacterium need to be straightened out. Two different studies have found that MreB filaments localize to regions of negative curvature, which are small "inward dimples" along the cell length (Ursell et al. 2014), and the inner (more curved) face of a sharply bent cell (Renner et al. 2013). Thus, the MreB-mediated insertion of new cell wall material at these areas would flatten out small local defects, or straighten bent cells.

The filaments are short, disconnected, and mobile. How is that a 'skeleton'?

Although actin and tubulin homologs are used by eukaryotes and prokaryotes to accomplish similar tasks (e.g. cell shape maintenance, cell division, and DNA segregation), they differ in their filament structure, assembly kinetics, and spatial regulation. Even among the prokaryotic filaments there is a wide diversity of properties, demonstrating that biology can solve similar problems using many different strategies.

Eukaryotic and prokaryotic filaments also differ in the length scales they coordinate. The eukaryotic cytoskeleton is a system of interconnected fibers – a mechanically coherent structure that is persistent over long distances, setting up a global cellular coordinate system. In contrast,

the most conserved bacterial filaments of the "prokaryotic cytoskeleton," MreB and FtsZ, confer cell shape by locally influencing cell wall synthesis. These filaments are short and disconnected (debated for FtsZ), and thus cannot globally organize the cell. Moreover, recent studies showed that protein localization patterns could be dramatically altered by the fluorescent tag used (Wang et al. 2014; Landgraf et al. 2012). In one study, constructs with 14 different fluorescent proteins fused to a common target (ClpXP) were compared, demonstrating that some fusions induce clustering of soluble proteins. Given these worrisome findings, it will be interesting to see how organized bacterial cells really are.

CHAPTER 3

Two spatially distinct cell wall synthesis machineries

This chapter was previously published as:

H. Cho*, C.N. Wivagg*, M. Kapoor* et al., 2016. Bacterial cell wall biogenesis is mediated by SEDS and PBP polymerase families functioning semi-autonomously. *Nature Microbiology*, 1, p.16172.

**These authors contributed equally to this work.*

Overview and motivation

The reevaluation of MreB's function as a long-range cytoskeleton had a major impact on our understanding of cell wall synthesis. Far from being a static track for cell wall synthesis enzymes to traverse, MreB filaments were instead dynamic, mobile, and restricted to having local rather than global effects. In turn, this reevaluation called into question the prevailing models about the organization of cell synthesis. MreB had been thought to spatially organize the entire process: from the synthesis of cytoplasmic precursors, to their flipping across the cell membrane, to the polymerization of peptidoglycan and even the hydrolysis of old cell wall material (Rueff et al. 2014; White et al. 2010; Divakaruni et al. 2005; Carballido-Lopez et al. 2006; Eun et al. 2015).

The new studies demonstrated that in *B. subtilis,* bPBPs, the crosslinking enzymes, participated in Rod complexes, showing characteristic MreB-like circumferential motion when viewed by fluorescence microscopy. Because bPBPs do not polymerize glycan chains, it was hypothesized that Rod complexes must also contain aPBPs as a source of glycosyltransferase

activity, a prediction that was weakly supported by older reports that aPBPs displayed helical localization in *B. subtilis* (Kawai et al. 2009).

However, this model was complicated by the fact that *B. subtilis* is viable in the absence of all four known aPBP-like transglycosylase enzymes (McPherson & Popham 2003). This suggested that there exists a missing transglycosylase that had not yet been identified - and indeed, given the rod shape of the quadruple-null mutant cells, it could participate in Rod complexes. A promising candidate was RodA, a protein belonging to the Shape Elongation Sporulation & Division (SEDS) family. RodA was known to be essential, required for rod-shape, and display MreB-like motion, suggesting its participation in Rod complexes. Although RodA had previously been thought to be a flippase enzyme responsible for transporting Lipid II across the cell membrane, recent reports that MurJ and AmJ were the flippase enzymes left RodA without an assigned function (Sham et al. 2014; Meeske et al. 2015).

In this study, we developed a new *in vivo* assay to study the glycosyltransferase activity of RodA in *E. coli*. We also demonstrated by fluorescence microscopy and single molecule tracking that RodA and PBP2 (a bPBP) form part of the Rod complex in *E. coli*, and demonstrate through biochemical as well as microscopy assays that aPBPs and the Rod system constitute two spatially separate, semi-autonomous cell wall biogenesis machineries in both *B. subtilis* and *E. coli*.

Abstract

Multi-protein complexes organized by cytoskeletal proteins are essential for cell wall biogenesis in most bacteria. Current models of the wall assembly mechanism assume class A penicillin-binding proteins (aPBPs), the targets of penicillin-like drugs, function as the primary

cell wall polymerases within these machineries. Here, we use an *in vivo* cell wall polymerase assay in *Escherichia coli* combined with measurements of the localization dynamics of synthesis proteins to investigate this hypothesis. We find that aPBP activity is not necessary for glycan polymerization by the cell elongation machinery as is commonly believed. Instead, our results indicate that cell wall synthesis is mediated by two distinct polymerase systems, SEDS-family proteins working within the cytoskeletal machines and aPBP enzymes functioning outside of these complexes. These findings thus necessitate a fundamental change in our conception of the cell wall assembly process in bacteria.

Introduction

An essential cell wall surrounds most bacteria protecting their cytoplasmic membrane from osmotic rupture (Typas et al. 2012). This structure is built from the heteropolymer peptidoglycan (PG), which consists of glycan chains with attached peptides used to form inter-strand crosslinks that generate a matrix-like shell. PG biogenesis is disrupted by many of our most effective antibiotics and remains an attractive target for the development of new therapies to counter the growing problem of drug-resistant infections (McKenna 2013).

Rod-shaped bacteria typically use two essential cell wall biogenesis machines to grow and divide (Typas et al. 2012). Cell elongation is promoted by the Rod system, which consists of several integral membrane proteins, including RodA, a SEDS-family protein, and PBP2, a class B penicillin-binding protein (bPBP) with transpeptidase (TP) activity that forms cell wall crosslinks. The Rod system is organized by dynamic filaments of the actin homolog MreB that are thought to direct new cell wall synthesis to establish and maintain rod shape (Typas et al. 2012; Jones et al. 2001; Garner et al. 2011; Domínguez-Escobar et al. 2011; van Teeffelen et al.

2011; Ursell et al. 2014) (**Fig. 3.1A**). Cell division is mediated by a different multi-protein machine, the divisome, organized by the tubulin homolog FtsZ (Typas et al. 2012; Bi & Lutkenhaus 1991). The proteins composing the divisome are largely distinct from that of the Rod system, but it contains homologous factors for PG synthesis like the SEDS-family protein FtsW and PBP3, a bPBP related to PBP2 (Typas et al. 2012).

Due to the lack of specific *in vivo* assays, the enzymes that synthesize PG glycans within the MreB- and FtsZ-directed machines have not been clearly defined. The generally accepted model is that glycan polymerization by these systems is mediated by the class A PBPs (aPBPs), which are bifunctional enzymes possessing both PG glycosyltransferase (PGT/polymerase) and TP (crosslinking) activity (Typas et al. 2012). In support of this idea, aPBP activity is indispensable for growth in many organisms (Yousif et al. 1985; Hoskins et al. 1999; Paik et al. 1999). Additionally, aPBP-like PGT domains have been the only factors known to possess PG polymerase activity (Sauvage et al. 2008). However, this functional assignment fails to account for the observation that certain gram-positive bacteria, including *Bacillus subtilis* and some species of *Enterococcus,* are viable and continue producing PG in the absence of identifiable aPBP-like domains (McPherson & Popham 2003; Rice et al. 2009). Moreover, it has remained unclear whether this unidentified polymerase activity is unique to certain gram-positive species or broadly distributed in bacteria.

A novel *in vivo* assay for PG polymerase activity

To determine if PG synthesis by the Rod system is dependent on aPBP function, we developed an *in vivo* assay to monitor PG polymerase activity. The assay is based on our observation that TP inactivation by beta-lactams in *E. coli* leads to the formation of

uncrosslinked PG glycans that are rapidly degraded into turnover products, which can then be quantified as an indirect measure of PG polymerase activity (Cho et al. 2014; Uehara & Park 2008) (**Fig 3.1B**).

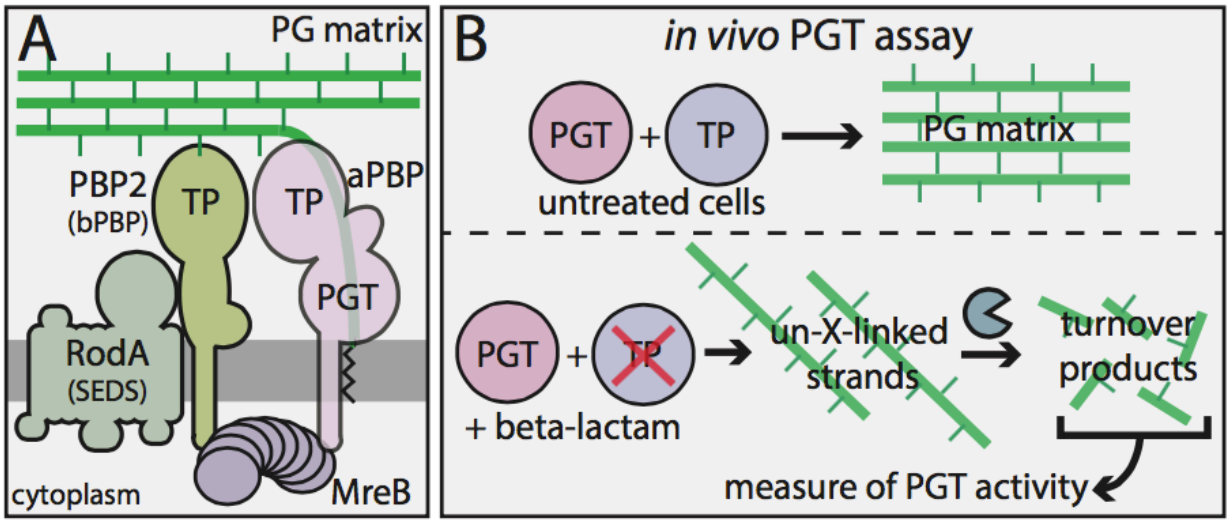


Figure. 3.1. The Rod system and an *in vivo* assay of peptidoglycan (PG) polymerase activity. A. Diagram of the currently accepted model for PG biogenesis by the Rod system. Polymers of the actin-like MreB protein organize a complex of membrane proteins including RodA, PBP2, and an aPBP. Glycan polymerization and crosslinking by this complex is thought to be promoted primarily by the peptidoglycan glycosyltransferase (PGT) and transpeptidase (TP) activities of aPBPs with additional TP activity provided by PBP2. **B.** In untreated cells, PG polymerization and crosslinking by PGT and TP enzymes, respectively are tightly coupled to form the PG matrix (upper panel). When TP activity is inhibited by a beta-lactam, the polymerase working with the blocked TP continues to produce uncrosslinked glycans that are rapidly degraded into fragments that can be isolated and quantified as a measure of polymerase activity (lower panel).

Because it specifically targets PBP2, the beta-lactam mecillinam facilitates the measurement of polymerase activity within the Rod system (Cho et al. 2014). In this assay, cells are first blocked for divisome function, thus eliminating its contribution to synthesis and focusing the measurement on Rod system activity. Under these conditions, mecillinam treatment reduces the ability of cells to incorporate the radiolabeled PG precursor [^{3}H]-diaminopimelic acid ([^{3}H]-DAP) into the PG matrix. Instead, a dramatic increase in labeled turnover products is

observed, which reflects PG polymerization by the Rod system (Cho et al. 2014) (**Fig. 3.2A-B, samples 1 and 2**). Consistent with this interpretation, simultaneous mecillinam treatment and inactivation of the Rod system with A22, an MreB polymerization antagonist, dramatically reduces both synthesis and turnover (**Fig. 3.2A-B, samples 1 and 6**) (Cho et al. 2014).

PG polymerization by the Rod system does not require aPBP activity

The effect of aPBP inactivation on Rod system activity was investigated using an *E. coli* strain (HC533) producing a modified PBP1b as its only aPBP. This variant of PBP1b, referred to as ^{MS}PBP1b, harbors a Ser247Cys substitution in its PGT domain allowing specific inhibition of its polymerase activity using the cysteine-reactive reagent MTSES (2-sulfonatoethyl methanethiosulfonate) (Sham et al. 2014). In the absence of MTSES, HC533 cell growth and morphology were indistinguishable from WT cells, and PG biogenesis activity was similar to cells producing an unaltered copy of PBP1b (**Fig. A.1A-C**). Treatment of [^{3}H]-DAP labeled, division-inhibited HC533 cells with MTSES reduced PG synthesis without stimulating turnover (**Fig. 3.2A-B, sample 3**). This level of PG synthesis inhibition was similar to that observed upon treatment of an outer-membrane defective strain with the canonical PGT inhibitor moenomycin (**Fig. A.1D**). Surprisingly, however, these MTSES-treated cells retained significant (~20%) PG synthetic activity (**Fig. 3.2A-B, sample 3**).

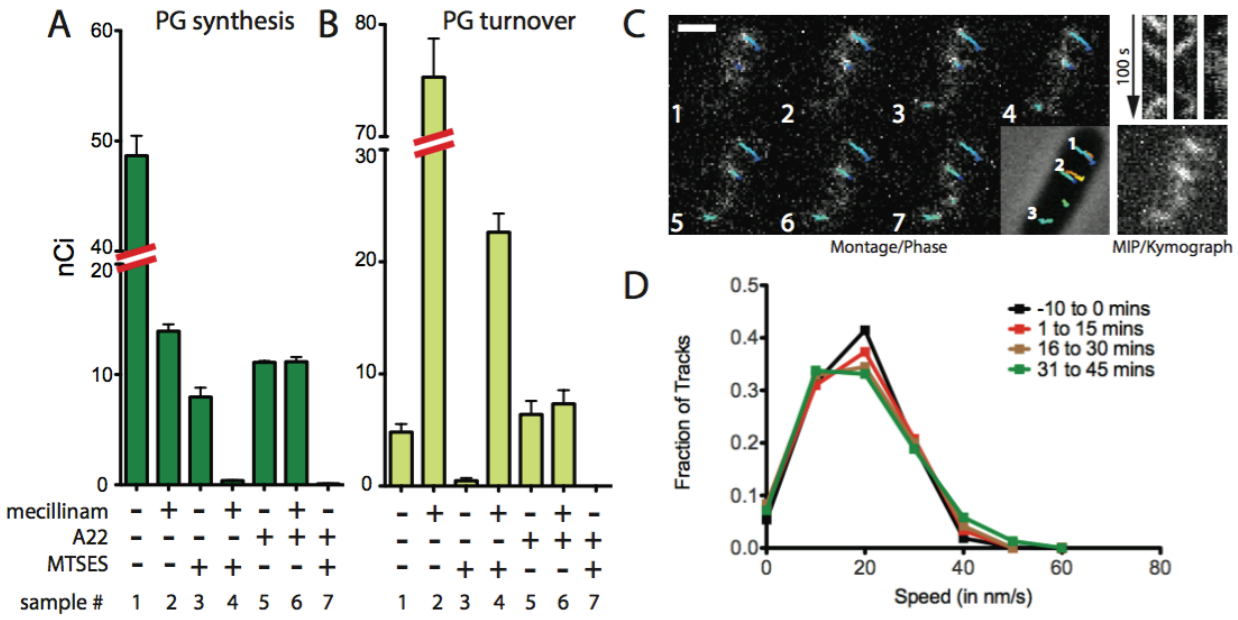


Figure. 3.2. PG polymerization by the Rod complex does not require aPBP activity. A-B. Cells of HC533(attλC739) [Δ*lysA* Δ*ampD* Δ*ponA* Δ*pbpC* Δ*mtgA* ^{MS}*ponB* (P_{tac}::*sulA*)] producing SulA to block cell division were pulse labeled with [^{3}H]-mDAP following treatment with the indicated compound(s). Turnover products were extracted with hot water and quantified by HPLC and in-line radiodetection. PG incorporation was determined by digesting the pellets resulting from the hot water extraction with lysozyme and quantifying the amount of label released into the supernatant by scintillation counting. Compound concentrations used were: mecillinam (10 µg/ml), A22 (10 µg/ml), MTSES (1 mM). Results are the average of three independent experiments with the error bars representing the standard error of the mean (SEM). **C**. *Left:* Montage with overlaid tracks highlighting MreB movement in HC546(attλHC897) [Δ*ponA* Δ*pbpC* Δ*mtgA* ^{MS}*ponB* (*P_{lac}::mreB-*^{SW}*mNeon)*] after 30 min MTSES inactivation of PBP1b showing continuing MreB motion. Frames 2 s apart, scale bar = 1 µm. Original time-lapse movies are 1 sec/frame. *Right top*: Kymographs drawn along trajectories indicated on phase contrast image (1, 2, 3, left to right). Each tracked particle is highlighted with a colored trajectory with the color of the track (blue to red) indicating the passage of time. **D.** Distribution of velocities of MreB motion taken at different points after aPBP inhibition with MTSES (1 mM). For the tracks that we can accurately calculate a particle's velocity, the fraction of moving particles only declines slightly (from 76% to 66%) during the time course following MTSES treatment. Microscopy results are representative of at least two independent experiments.

This synthesis was not due to residual ^{MS}PBP1b activity as analysis by mass spectrometry indicated that the protein was fully modified by MTSES (**Table A.1 and Fig. A.2**), and experiments with the beta-lactam cefsulodin (described below) show that this treatment completely disrupts aPBP-mediated PG polymerization. Thus, the observed MTSES-resistant synthesis suggests that, like gram-positive bacteria, *E. coli* also encodes a non-aPBP-mediated PGT activity. This MTSES-resistant synthesis was inhibited by co-treatment with A22 and fully converted to PG turnover products with mecillinam co-treatment (**Fig. 3.2A-B, samples 4 and 7**), indicating that the non-aPBP PGT enzyme resides in the Rod system.

Fluorescently-tagged MreB displays a dynamic subcellular localization with many discrete foci rotating around the circumference of the cell cylinder (Garner et al. 2011; Domínguez-Escobar et al. 2011; van Teeffelen et al. 2011). As MreB rotation is halted by beta-lactams and other PG synthesis inhibitors, this motion is thought to reflect new cell wall synthesis (Garner et al. 2011; Domínguez-Escobar et al. 2011; van Teeffelen et al. 2011). To monitor the effect of aPBP inactivation on MreB dynamics, we followed the motion of a functional mNeonGreen-MreB sandwich fusion (MreB-^{SW}mNeon) (**Fig. A.3**) in cells possessing ^{MS}PBP1b as the sole aPBP. MreB-^{SW}mNeon foci continued rotating following aPBP inhibition by MTSES at a speed undifferentiable from untreated cells (20 nm/s) until the lack of aPBP activity caused cell lysis (**Fig. 3.2C-D**). Thus, both radiolabeling and imaging indicate that aPBPs are not required for PG polymerization by the Rod system in gram-negative bacteria as is widely believed.

RodA and PBP2 display MreB-like circumferential motion in *E. coli*

Results from a parallel *B. subtilis* study indicate that RodA functions as a PG polymerase (Meeske et al. 2016). We therefore hypothesized that RodA might also be responsible for the aPBP-independent PG synthesis we observed in *E. coli*. If true, we reasoned that *E. coli* RodA should display MreB-like circumferential motion as has been observed in *B. subtilis* (Domínguez-Escobar et al. 2011). Imaging of a mostly functional sfGFP-RodA fusion (**Fig. A.4 A and B**) revealed both fast, non-directionally moving particles consistent with molecules diffusing in the membrane, and particles moving slowly and directionally at the same rate and angle as MreB (**Fig. 3.3 and A.5**). SEDS-family proteins form complexes with partner bPBPs (Typas et al. 2012; Fay et al. 2010; Fraipont et al. 2011), suggesting that RodA is likely to function in conjunction with PBP2. We therefore also investigated PBP2 dynamics using a functional msfGFP-PBP2 fusion (**Fig. A.4A, C, and D**). Imaging at fast acquisition rates (50 or 100 msec/frame) showed what appeared to be particles rapidly diffusing within the membrane as reported previously (Lee et al. 2014). However, imaging with longer acquisition times (1 sec/frame), which blurs the motion of rapidly diffusing particles across many pixels, revealed a subpopulation of PBP2 foci moving slowly and directionally around the cell circumference at the same rate and angle as MreB and RodA (**Fig. 3.3 and A.6**). These two types of PBP2 motions are analogous to what has been observed in *B. subtilis* for PBP2a (Garner et al. 2011). Similarly, we interpret the slow, rotating particles of RodA and PBP2 as those engaged in active, MreB-associated PG synthesis. To investigate whether RodA PGT activity is required for MreB motion, we monitored the effect of a dominant-negative RodA variant (D262N) (**Fig. A.7**) on MreB-^{SW}mNeon dynamics.

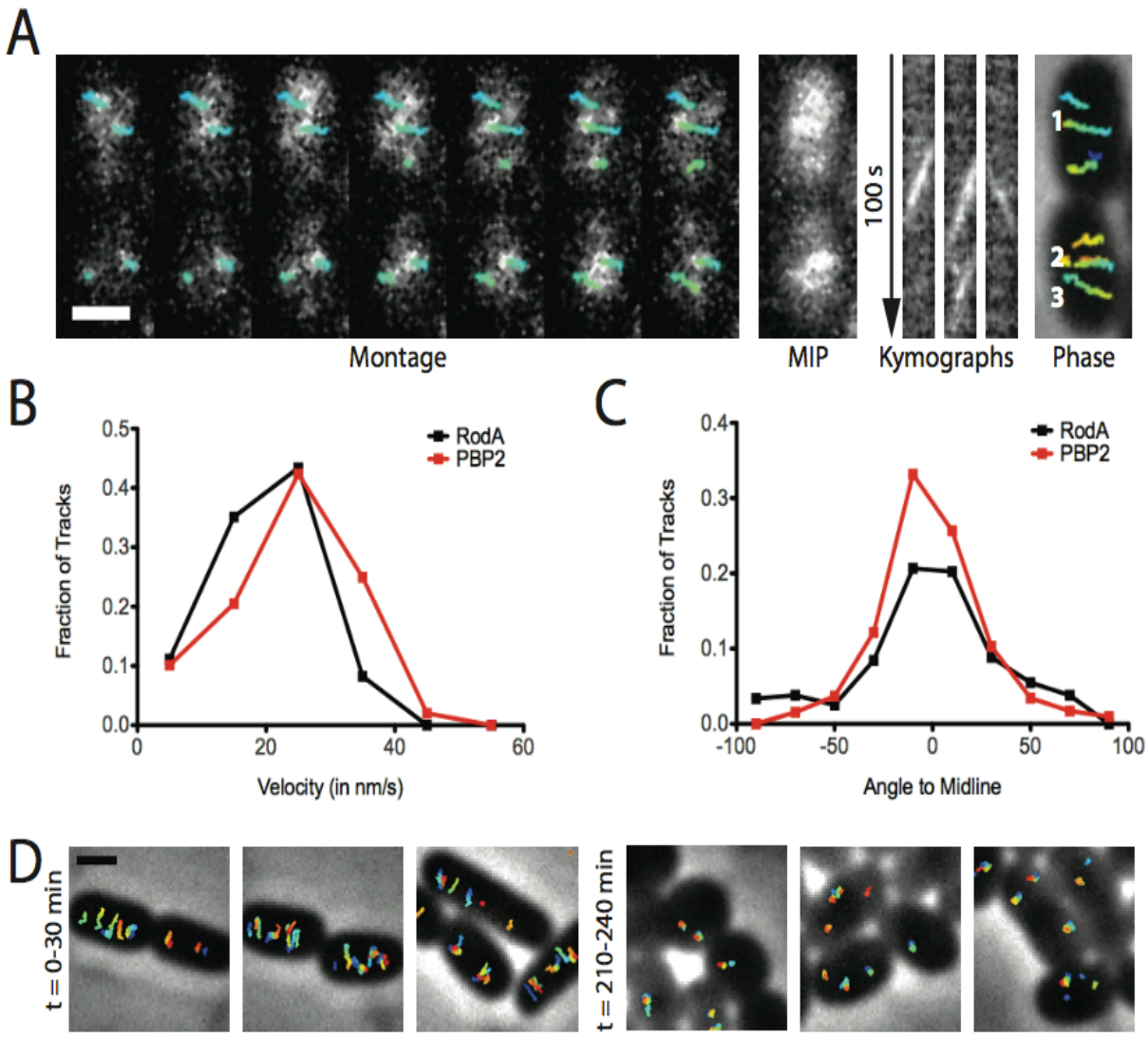


Figure. 3.3. PBP2 and RodA display directed, circumferential motions similar to MreB. A. *Left to right*: Montage of PBP2 movement with overlaid tracks in HC596(attHKHC943) [Δ*ponA* Δ*pbpC* Δ*mtgA* Δ*pbpA* (P_{lac}::*msfgfp-pbpA*)]. Frames 2 s apart. Each tracked particle is highlighted with a colored trajectory as in **Figure 3.2C**. Trajectories 1, 2, and 3 in kymographs are in order left to right. **B**. Distribution of velocities of tracked particles of MreB (n = 807), PBP2 (n=1234) and RodA (n=243). **C**. Distribution of angles of PBP2 and RodA trajectories relative to the cell midline. **D.** Tracked particles of MreB-^{SW}mNeon at 0-30 or 210-240 min after induction of RodA(D262N) from strain TB28(attHKHC929)/pHC938 [WT(P_{tetA}::*mreB-*^{SW}*mNeon*)/P_{lac}::*pbpA-rodA(D262N)*]. Each tracked particle is highlighted with a different color trajectory overlaid on a phase contrast image. All scale bars are 1 μm. In all cases, original time-lapse movies are 1 sec/frame. Microscopy results are representative of at least two independent experiments.

This RodA derivative contains an amino acid change in a periplasmic loop residue critical for PGT activity (Meeske et al. 2016). Strikingly, production of RodA(D262N) but not RodA(WT) led to a gradual, filament by filament cessation of MreB-^{SW}mNeon motion (**Fig. 3.3D**). We therefore infer that RodA and PBP2 function as the core PGT/TP pair of the Rod system in both *E. coli* and *B. subtilis* (Meeske et al. 2016).

aPBPs function outside of cytoskeletal complexes in *E. coli* and *B. subtilis*

In current models of PG biogenesis, aPBPs are associated with either the MreB- or FtsZ-directed synthetic machineries (Typas et al. 2012), implying that they function primarily within these complexes and may require cytoskeletal association for activity. However, cell growth and cell wall synthesis by an uncharacterized activity was previously observed in cells blocked for both FtsZ and MreB function (Varma et al. 2007; Tan et al. 2011), suggesting a possible cytoskeleton-independent mode of PG synthesis. Indeed, when PG synthesis and turnover were measured in HC533 cells blocked for both FtsZ and MreB activity by SulA and A22, respectively, significant PGT activity was still detected (**Fig. 3.2A, sample 5**). This activity was completely inhibited upon MTSES treatment to inactivate ^{MS}PBP1b, indicating that cytoskeleton-independent synthesis is mediated by aPBPs (**Fig. 3.2A, sample 7**). To further test the dependence of aPBP polymerase activity on cytoskeletal function, we employed the aPBP-specific beta-lactam cefsulodin (Curtis et al. 1979), which induces increased glycan degradation similar to mecillinam (Cho et al. 2014). This turnover likely reflects PGT activity promoted by aPBP molecules with a drug-inactivated TP active sites (**Fig. 3.1B**). Consistent with this interpretation, treatment of ^{MS}PBP1b-producing (HC533) cells with MTSES completely blocked cefsulodin-induced glycan degradation (**Fig. 3.4A-B, samples 1 vs. 3, and 2 vs. 4**).

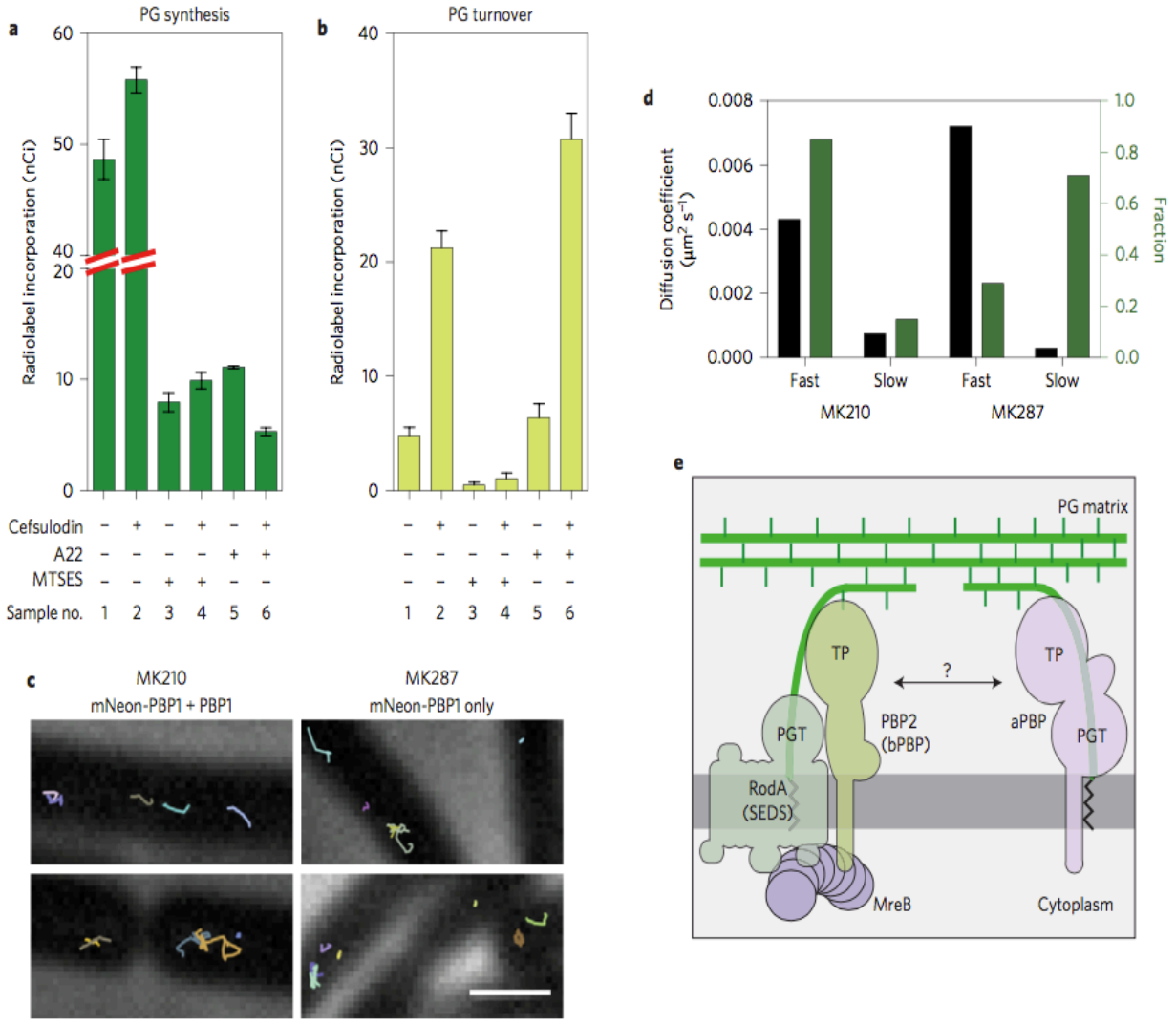


Figure. 3.4. aPBPs can function independently from the cytoskeletal machinery. A-B. PG matrix assembly and turnover were measured as in **Figure 3.2** using strain HC533(attλC739) [Δ*lysA* Δ*ampD* Δ*ponA* Δ*pbpC* Δ*mtgA* ^{MS}*ponB* (P_{tac}::*sulA*)]. Cefsulodin was used at 100 μg/ml. Results are the average of three independent experiments with the error bars representing the SEM. **C**. Tracks of mNeon-PBP1 expressed as (right) the only copy or (left) in addition to native untagged protein in *B. subtilis.* Each continuously tracked particle is highlighted with a different color trajectory. Note that although no MreB-like directional motion was observed, particles occasionally travel rapidly in one direction for a few frames as expected for membrane diffusion. **D.** Graph showing diffusion constants, and fraction of particles tracked in each diffusion state as determined by CDF analysis. Microscopy results are representative of at least two independent experiments. **E.** Schematic view of a new model for PG biogenesis involving two different classes of PG polymerases working semi-autonomously. SEDS PGTs and partner bPBPs perform PG polymerization and crosslinking in the context of the Rod system and divisome (not shown) while aPBPs function outside of these complexes. Collaboration between the synthases likely occurs but the mechanism remains to be defined.

This result also supports the conclusion that ^{MS}PBP1b PGT activity is completely inactivated upon MTSES treatment. In contrast to MTSES addition, cefsulodin-induced turnover was stimulated by MreB depolymerization with A22 in cells already blocked for FtsZ activity by SulA (**Fig. 3.4A-B, sample 5-6**). Thus, glycan synthesis by PBP1b proceeds robustly in cells lacking all functional cytoskeletal filaments. Similarly, PG synthesis and turnover assays using cefsulodin and a strain where PBP1a was the sole remaining aPBP also detected cytoskeleton-independent glycan polymerization by PBP1a (**Fig. A.8**). The functionality of aPBPs in the absence of cytoskeletal filaments suggests that aPBPs may operate in a spatially distinct manner from the MreB- and FtsZ-directed machineries. To investigate this possibility, we followed aPBP subcellular dynamics in both *E. coli* and *B. subtiils*. In *E. coli*, a functional msfGFP-PBP1b (**Fig. A.9**) was produced as the sole aPBP. At the lowest induction level capable of supporting growth (13 μM), imaging at both long (1 sec) and short (100 msec) acquisition times like those used for PBP2 and RodA did not reveal any directional motion. We verified this result using single-molecule imaging of a functional Halo-tagged PBP1b fusion (Halo-PBP1b) labeled with low concentrations of JF-549 (Grimm et al. 2015; Vrljic et al. 2002). Only motion consistent with membrane diffusion was observed. Likewise, imaging msfGFP-PBP1b motion during its depletion also did not reveal any MreB-like directional motion even under conditions where depletion resulted in cell lysis. Furthermore, an msfGFP-PBP1a fusion produced as the sole aPBP in the cell also did not display MreB-like dynamics.

To determine if aPBPs also display dynamics distinct from the Rod system in gram-positive bacteria, we imaged a functional mNeon-PBP1 fusion (**Fig. A.10**) produced in *B. subtilis* as the sole copy of PBP1 or alongside the native protein. No directional motion was observed either when the fusion was produced from its native promoter or at low levels that

allowed single molecule tracking (**Fig. 3.4C-D, A.11**). Rather, analysis of single-molecule trajectories using cumulative distribution functions (CDF) indicated that PBP1 exists in two states: diffusive (D = 0.004-0.007 $\mu m^2/s$) and immobile (D = 0.0003-0.0007 $\mu m^2/s$) (**Fig. 3.4C-D, A.11**). The slow, immobile particles predominated in cells producing mNeon-PBP1 as the sole source of PBP1. When the fusion was expressed in addition to native PBP1, the fraction of faster diffusing molecules increased. This observation suggests a saturable number of available sites for the immobile particles that may reflect a functional state of PBP1. We conclude that aPBP polymerases from two different and evolutionarily distant model organisms display *in vivo* dynamics distinct from the circumferential motions observed for Rod system components.

A new view of PG biogenesis in bacteria

Overall, our results indicate that the aPBPs are not essential components of the Rod system in *E. coli* and suggest that these enzymes are performing significant roles in PG biogenesis apart from the complex. Instead of the aPBPs, the SEDS-protein RodA appears to supply the PG polymerase activity crucial for Rod system function (Meeske et al. 2016). The RodA polymerase, in turn, likely works in complex with PBP2, which provides crosslinking activity. By extension, the SEDS-family FtsW protein and its partner PBP3 are likely providing PG polymerase and crosslinking activity within the divisome. These findings necessitate a fundamental change in our view of the mechanism of cell wall assembly in bacteria and furthermore raise intriguing questions about the relative roles of the different types of PG polymerases in the process (**Fig. 3.4E**).

Inactivation of aPBP activity reduces total cell wall synthesis to approximately 20% normal levels, indicating that these enzymes play major roles in PG biogenesis. The same is true

when the cytoskeletal systems are inactivated and aPBPs remain functional; only about 20-30% of normal PG synthesis activity is detected. Thus, even though the aPBPs and Rod system components show distinct subcellular dynamics and are unlikely to be working stably together within the same complex, full cell wall synthesis efficiency requires that both systems be functional. Therefore, although our data support the idea that there is a division of labor between the aPBPs and the cytoskeleton-directed SEDS/bPBP systems, they appear to be only semi-autonomous and are likely collaborating with each other at some level. This partial interdependence may indicate that the two systems specialize in distinct but related aspects of the wall biogenesis process similar to how different DNA polymerases work together to properly complete chromosome replication. For example, the more broadly conserved SEDS/bPBP systems (Meeske et al. 2016) may build the primary structural foundation for the PG matrix while the aPBPs support this foundation by adding to it and filling in gaps that arise during normal expansion and/or as the result of damage. Testing this and other possibilities in the context of the new framework provided in this and our companion report (Meeske et al. 2016) will pave the way for a better mechanistic understanding of bacterial cell wall assembly and the discovery of novel ways to disrupt this process for antibiotic development.

CHAPTER 4

Control of cell diameter in *Bacillus subtilis*

This chapter was a manuscript in preparation for submission:

M. Kapoor*, M. F. Dion*, and E. C. Garner, 2017. Control of cell diameter in *Bacillus subtilis*.

**These authors contributed equally to this work.*

Abstract

The peptidoglycan cell wall of *Bacillus subtilis* helps the cell to resist osmotic pressure and maintain rod shape. Two spatially distinct, semi-autonomous peptidoglycan biogenesis machineries synthesize new peptidoglycan as the cell elongates: the Rod system, organized by MreB filaments, is circumferentially patterned while the class A penicillin-binding proteins appear spatially unorganized. It remains a mystery how the combined contributions of these machineries create a uniform rod-shaped cell. Although MreB is responsible for maintaining cell diameter, it is unknown how this diameter is generated. Here, we use genetics and fluorescence microscopy to show that the balance between organized and unorganized synthesis determines the diameter of the cell. Further, we find that enzymes of the Rod system, when present in excess, also function independently and create spatially unorganized synthesis. These findings reveal new relationships and redundancies between the two machineries, and raise questions about the extent to which they collaborate.

Introduction

How cells control their size and shape is a foundational biological question that integrates topics ranging from cell physiology and growth to antibiotic discovery (Young 2007; Young 2010). For the bacterium *Bacillus subtilis*, which requires its cell wall to maintain its rod-shaped morphology throughout growth and division, cell shape is intimately linked to the process of cell wall synthesis (Typas et al. 2012). A major component of the *B. subtilis* cell wall is peptidoglycan: a heteropolymer of glycan strands woven into a meshwork-structure via cross-linking of their peptide stems (Vollmer et al. 2008).

Independent, essential, cell wall synthesis machineries perform specialized roles during the processes of cell elongation and cytokinesis (Typas et al. 2012). Until recently, all PG-synthesis activity was assigned to the penicillin-binding proteins (PBPs); the bifunctional class A PBPs (aPBPs) both polymerize and cross-link glycan strands *in vitro*, while the monofunctional class B PBPs (bPBPs) are transpeptidases that only cross-link strands (Barrett et al. 2007; Lebar et al. 2014; Banzhaf et al. 2012). It was thought that cell elongation is mediated by a group of proteins called the Rod complex, composed of both class A and class B PBPs along with several other integral membrane proteins, all of which are directed by filaments of the actin homologue MreB (Typas et al. 2012).

This model was challenged by our recent report that another essential, widely conserved, component of the Rod system - RodA - is a peptidoglycan polymerase (Cho et al. 2016; Meeske et al. 2016). Moreover, we showed that aPBP activity is not required for Rod system function; indeed, single molecule tracking demonstrates that aPBPs are spatially separable from MreB and bPBPs, functioning outside the Rod system (Cho et al. 2016). While the bPBPs and RodA move around the rod width with MreB, the aPBPs either move diffusively on the membrane, or show

transient periods of immobility (with a diffusion coefficient of 0.0003–0.0007 $\mu m^2 s^{-1}$) (Cho et al. 2016). However, this finding raises new questions: what are the distinct contributions of aPBPs and the Rod system to cell shape, and overall cell growth, and to what extent do the two systems collaborate or overlap in function?

In light of the discovery that bPBPs are spatially organized by MreB while aPBPs are not, it remains unknown how the two machineries work together to create a regular, rod-shaped sacculus of a defined diameter. Prevailing models of cell diameter homeostasis place paramount importance on the role of MreB filaments: various biophysical parameters such as filament curvature, filament angle/orientation, filament number, and filament length have been granted sole explanatory status (Ursell et al. 2014; Tropini et al. 2014; Desmarais et al. 2015). However, these models neglect the contribution of peptidoglycan synthesis enzymes, and do not account for the contribution of unorganized synthesis by aPBPs.

Here, we seek to develop a comprehensive understanding of how both organized and unorganized peptidoglycan syntheses influence cell shape and diameter, as well as how they contribute to cell growth. We show that the organized and unorganized synthesis of new cell wall has opposing effects on cell diameter, and their balance determines steady state diameter. Although aPBPs are not essential in *B. subtilis*, they were previously reported to be required for robust growth, with numerous reports of growth defects in mutants that lack one or more of these enzymes (Murray et al. 1998; Popham & Setlow 1996; McPherson & Popham 2003; Meeske et al. 2016). To the contrary, we find that, when assayed at the single-cell level, the loss of Rod system activity does negatively affect the rate of cell elongation, while that of aPBPs does not.

Results

The Rod system and aPBPs have opposing effects on cell diameter

To investigate the relationship between cell diameter and the cellular levels of peptidoglycan synthesis enzymes, we chose to study one growth condition - exponential growth in CH medium - and measured cell diameter by fluorescence microscopy (Fig. A.12). First, we modulated the expression levels of the two spatially distinct peptidoglycan synthesis systems, by controlling expression of *ponA* (encoding the major aPBP - PBP1) and the *mreBCD* operon (encoding three essential proteins of the Rod complex: MreB, MreC, and MreD).

We created strain bMD598 (*yhdH*:: P_{spa}-*ponA*::*cat* Δ*ponA::kan*), which contains a single copy of the *ponA* allele under the control of an IPTG-inducible promoter. Different induction levels of *ponA* revealed that the mean steady-state diameter of a population of cells could be titrated (Fig 4.1): In the absence of IPTG, cells were on average ~30% thinner than wild type cells (McPherson & Popham 2003). Conversely, strong induction of *ponA* caused an increase in diameter compared to wild type, and stronger overexpression of *ponA* in the merodiploid strains bMD554 (*yhdH*:: P_{hyp}-*ponA*::*cat*) and bMD586 (*yhdH*:: P_{hyp}-*ponA*::*cat* Δ*ponA::kan*) produced cells of nearly twice the wild type diameter.

We next created the strain bMD545 (*amyE*::P_{xyl}-*mreBCD*::*erm* Δ*mreBCD::spec*), which contains a single copy of the *mreBCD* operon under the control of a xylose-inducible promoter we found that the expression level of *mreBCD* had the opposite relationship to cell diameter (Fig. 4.2). In the lowest xylose concentration that supported growth, mean cell diameter was approximately twice that of wild type, with some cells losing rod shape. Conversely, overexpression of *mreBCD* produced cells that were thinner than wild type. This effect that was

even more pronounced in the merodiploid strain bMK355 (*amyE*::P_{xyl}-*mreBCD*::*erm*).

Because these two peptidoglycan synthesis systems appeared to have opposing effects on cell diameter, we hypothesized that a balance between the levels of spatially unorganized aPBPs and the organized, circumferentially moving Rod system might produce wild type diameter cells. Therefore, we combined the IPTG-inducible *ponA* and xylose-inducible *mreBCD* alleles into a single strain, bMD620 (*amyE*::P_{xyl}-*mreBCD*::*erm* Δ*mreBCD::spec yhdH*:: P_{spa}-*ponA*::*cat* Δ*ponA::kan*), where each system was expressed only from one inducible locus. This strain allowed us to identify five different pairs of inducer concentrations (and a sixth in the merodiploid bMD622 (*amyE*::P_{xyl}-*mreBCD*::*erm yhdH*:: P_{spa}-*ponA*::*cat* Δ*ponA::kan*)) that produce rods of wild type diameter, even though, individually, all of these inducer levels, when tested alone in the parental strains, resulted in perturbed (wider or thinner) cell diameter (Fig. 4.3). Importantly, measuring the growth rate of cells under these inducer concentrations demonstrated that the rate of cell growth was greatly slowed at the lowest induction conditions, going up at each increasing set of induction conditions (the first three bars of Fig. 4.4C).

The Rod system is required for robust growth, while aPBPs are not

We next measured how modulating *ponA* and *mreBCD* expression affected the growth rates of cells. To do this, we used single-cell microscopy to follow the increase in surface area of single chains over time. This revealed several unexpected relationships between cell wall synthesis and cell growth. First, contrary to previous reports, this demonstrated that absence of aPBPs does not affect the rate of cell growth, only the rate of cell lysis. Previous studies have reported that the absence of PBP1 decreases cell growth, as assayed by bulk OD measurements (Murray et al. 1998; Popham & Setlow 1996; McPherson & Popham 2003; Meeske et al. 2016).

To test this, we held the expression of *mreBCD* constant, while modulating the expression of *ponA*. This revealed that cells add surface area at a rate indistinguishable from wild type, regardless of *ponA* expression level. However, as previously reported, they do lyse more frequently as *ponA* expression is lowered, explaining the phenotypes observed by bulk OD measurements (Fig. 4.4A).

mreBCD showed a similar trend, where increasing expression had no effect on cell growth, save at the lowest point of induction, which showed a marked growth defect (Fig. 4.4b). Towards the lower end of the titration curve, imbalance between *ponA* and *mreBCD* expression does have a deleterious effect on the physiology of the cell - depletion of Rod complexes alone has a more severe growth defect than simultaneous depletion of Rod complexes and aPBPs together (Fig. A.13).

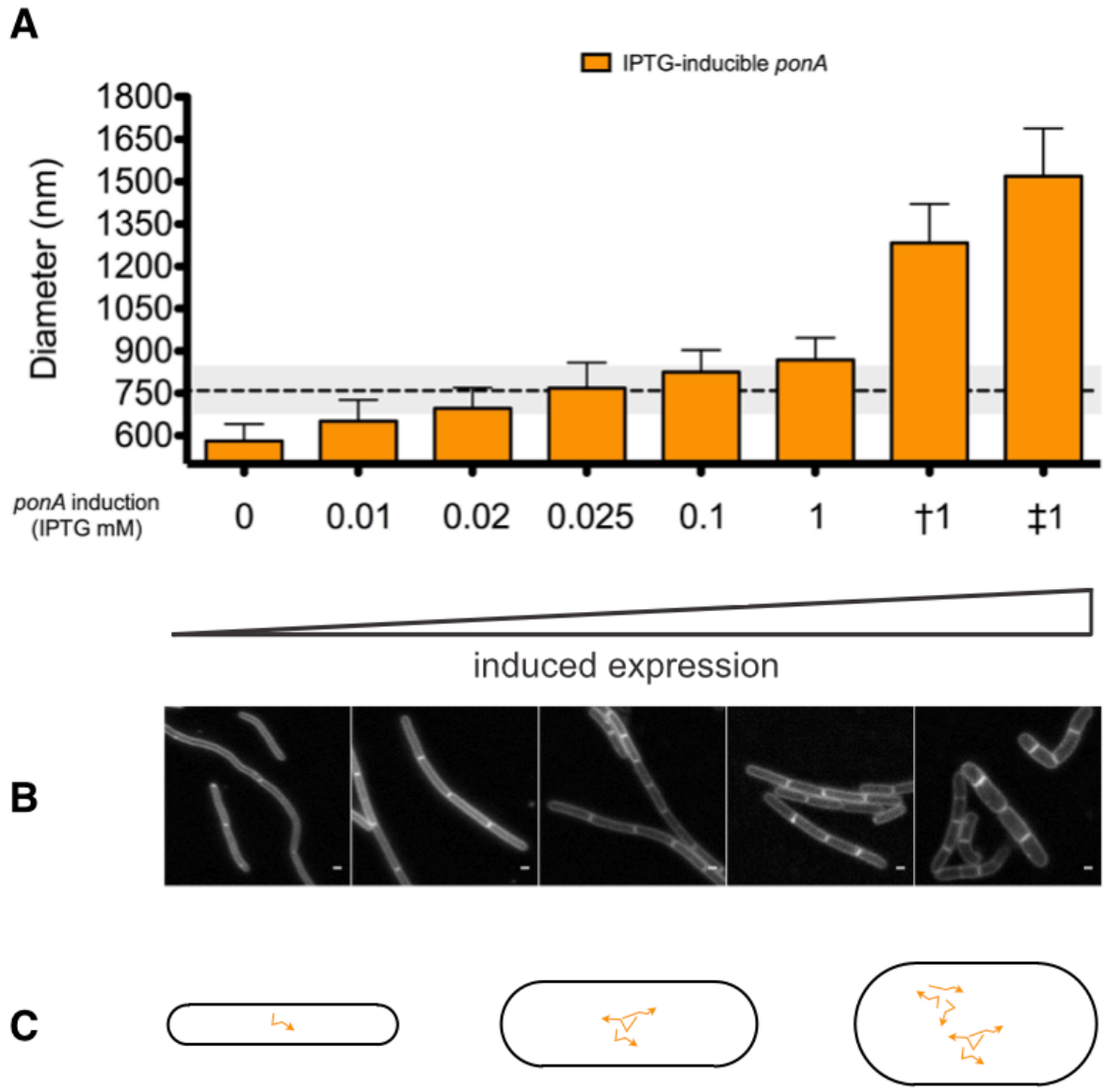


Figure 4.1. Steady-state diameter of cells increases as the expression level of *ponA* increases. A, The mean diameter of a population of cells increases as the expression level of *ponA* is increased. All data presented is from the strain bMD598, except for the data points marked † (bMD586) and ‡ (bMD554), in which *ponA* expression can be dialed to a level higher than in bMD598. The dashed line depicts the mean steady state diameter of PY79 (wild type) cells measured in Fig. A.12, and gray shaded area represents the standard deviation. Error bars represent standard deviation. **B**, Representative micrographs of FM 5-95 stained cells at five different *ponA* expression levels. **C**, Schematic of a model to explain these observations. Orange lines represent spatially unorganized synthesis; as the level of PBP1 increases, cell diameter increases. Scale bar = 1 μm

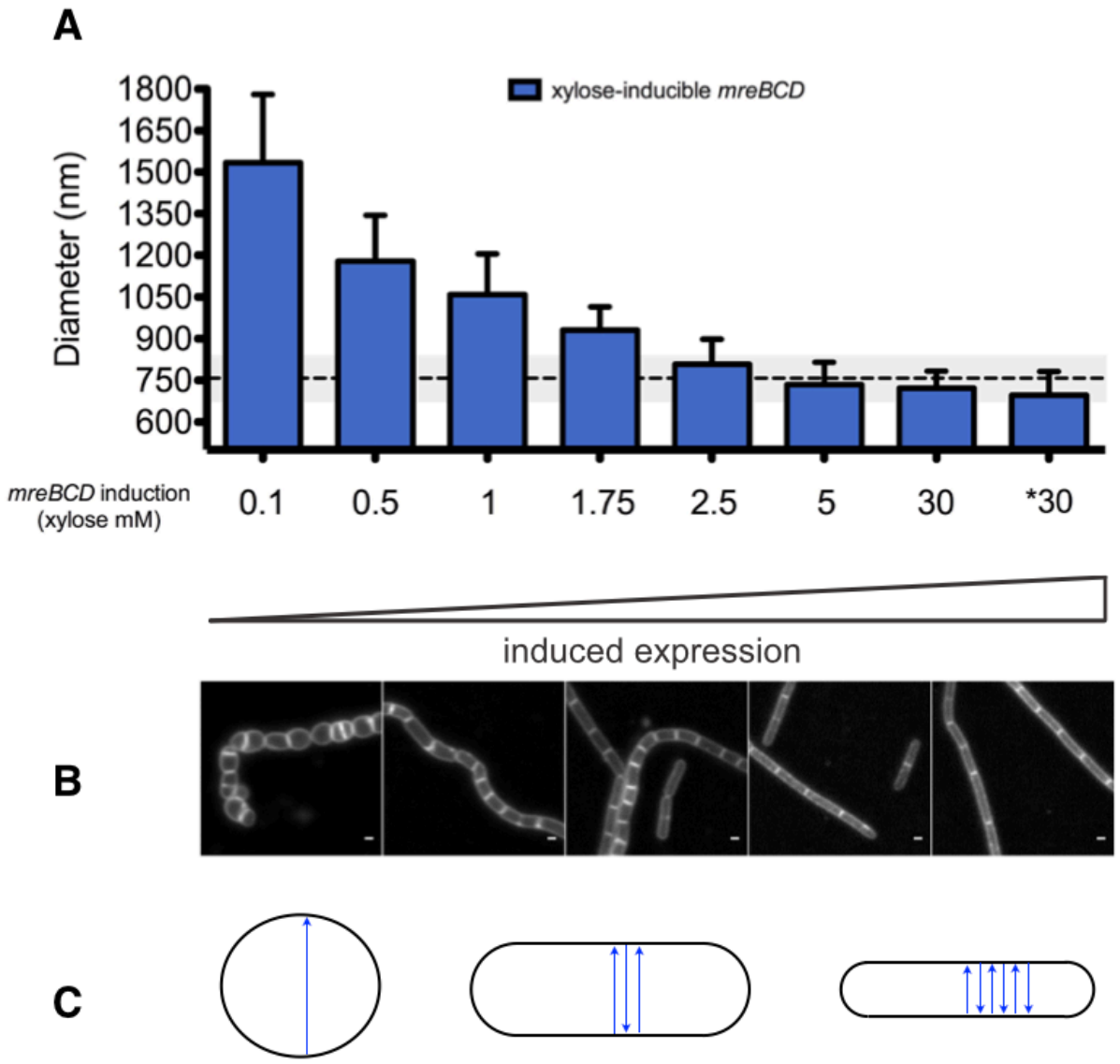


Figure 4.2. Steady-state diameter of cells decreases as the expression level of *mreBCD* increases. A, The mean diameter of a population of cells increases as the expression level of *mreBCD* is increased. All data presented is from the strain bMD545, except for the data point marked *****, which is from bMK355, a merodiploid strain in which *mreBCD* expression can be dialed to a level higher than in bMD545. The dashed line depicts the mean steady state diameter of PY79 (wild type) cells and the gray shaded area represents the standard deviation of the data. Error bars represent standard deviation. **B**, Micrographs of FM 5-95 stained cells, representative of five different expression levels of *mreBCD*. **C**, Schematic view of a model to explain these observations. Blue lines represent spatially organized synthesis; as the number of Rod complexes increases, cell diameter decreases. Scale bar = 1 μm.

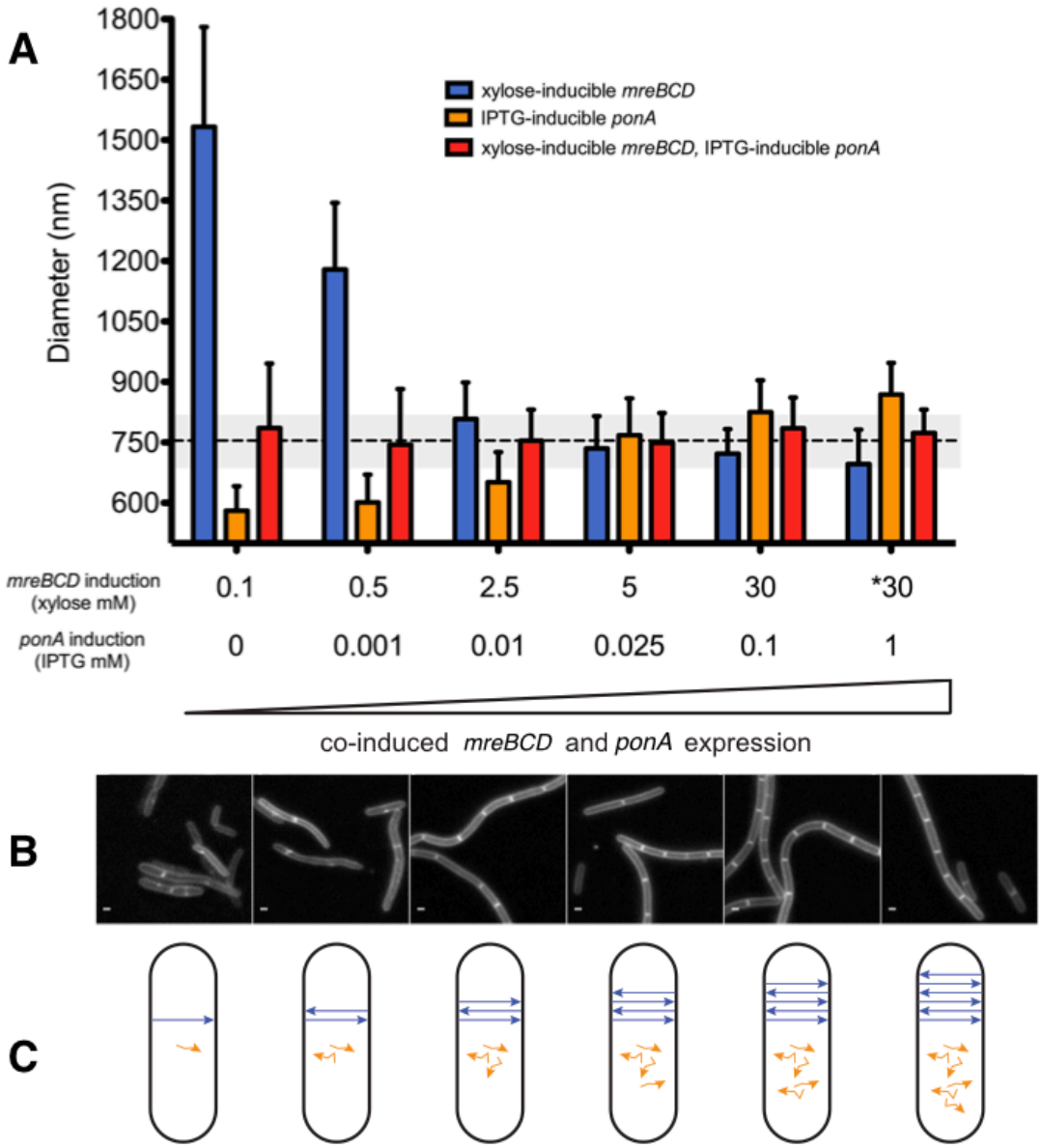


Figure 4.3. The balance between the Rod system and aPBPs determines cell diameter, across a range of expression levels. A, The mean diameter of a population of cells remains constant as the expression levels of *mreBCD* and *ponA* are concurrently increased.
The red bars represent the steady state diameter of bMD620 at five different combinations of xylose and IPTG levels, and of bMD622 (marked with *****) at a sixth combination. The blue and orange bars are data from **Figs. 4.1** and **4.2**, presented here for comparison: they represent the diameter produced by the specified IPTG or xylose levels in a singly inducible *ponA* or *mreBCD* strain. The dashed line depicts the mean steady state diameter of PY79 (wild type) cells, and the gray shaded area represents the standard deviation of the data. **B**, Micrographs of FM 5-95 stained cells, representative of all six conditions. **C**, Schematic view of a possible model to explain these observations. Blue lines represent spatially organized synthesis and orange lines represent spatially unorganized synthesis; as the levels of both syntheses are simultaneously raised, cell diameter remains constant. Scale bar = 1 μm

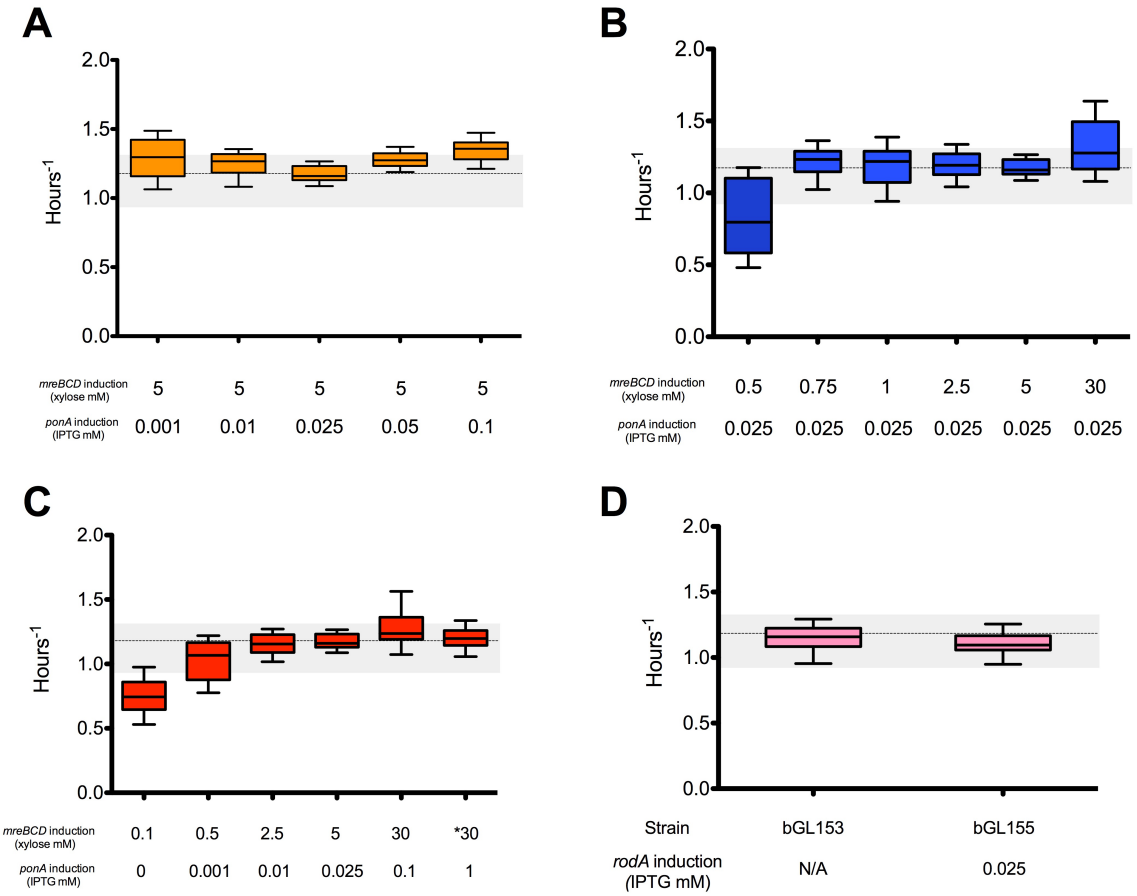


Figure 4.4. Relationships between single-cell growth rate and the expression levels of various cell wall synthesis enzymes. A, The surface area growth rate of single cells of bMD620 is unchanged over a range of *ponA* expression levels (at a constant *mreBCD* expression). **B**, At all but the lowest level (where growth rate was reduced), the single-cell growth rate of bMD620 was unchanged across a range of *mreBCD* expression levels. **C**, For the conditions previously demonstrated to have similar cell diameters in **Fig. 4.3**, the single-cell growth rate increased as the expression levels of *ponA* and *mreBCD* were simultaneously increased up to a point, after which it plateaued. The dashed line and the gray shaded area represent the mean and standard deviation of the growth rate of PY79 (wild type) cells.

RodA and PBP2 can function outside the Rod system

In light of our recent discovery that SEDS proteins work with bPBPs to synthesize peptidoglycan in the Rod system (Cho et al. 2016), we predicted that RodA and PBP2A

expression levels would bear the same relation to cell diameter as that of the MreBCD proteins. To test this, we created strains bMD590 (*pbpA*:: P_{xyl}-*pbpA*::*erm*) and bMD592 (*rodA*:: P_{xyl}-*rodA*::*erm*), in which *pbpA* and *rodA* respectively, are under the control of a xylose-inducible promoter. In both strains, at xylose concentrations that produced less RodA and PBP2A than wild type cells, cell diameter was larger than wild type, as expected from our results with bMD545 (Fig. 4.5), and consistent with previous studies (Henriques et al. 1998). However, instead of decreasing as upon *mreBCD* overexpression, when we overexpressed either RodA, cell diameter increased to be larger than wild type. This effect was even stronger in the merodiploid strains bMD556 (*yhdH*:: P_{hyp}-*rodA*::*cat*) and bMD580 (*yhdH*:: P_{hyp}-*rodA*::*cat* Δ*rodA::kan*). A similar, but apparently weaker effect was observed with PBP2A in the strains bMD572 (*yhdH*:: P_{hyp}-*pbpA*::*cat* Δ*pbpA::erm*) and bMD563 (*yhdH*:: P_{hyp}-*pbpA*::*cat*) (Fig. 4.5). This result suggested that bPBPs and RodA might also be functioning outside of Rod complexes when present in excess of wild type levels.

Meeske et al reported that elevated RodA levels could restore wild type width and growth rate in strains lacking aPBPs (Meeske et al. 2016). To examine this claim, we overexpressed RodA in the absence of all aPBPs in the strain bGL155 (Δ*pbpF* Δ*pbpG* Δ*pbpD amyE*::P_{hyp}-optRBS-*rodA-His10*::*spec*, *ponA*::*kan*); although elevated RodA levels did restore cell diameter to wild type levels at a given induction (Meeske et al. 2016), we found that when examined at the single-cell level, the surface area growth rate of induced bGL155 was identical to that of bGL153 (Δ*pbpF* Δ*pbpG* Δ*pbpD ponA*::*kan*), and of wild type cells (Fig. 4.4D). We conclude that the bulk growth rate increase reported by Meeske et al can be attributed to the observed reduction in the frequency of lytic death (Meeske et al. 2016).

The similar effects of PBP1 and PBP2A/RodA overexpression on cell diameter and

growth rate led us to wonder if excess PBP2A/RodA might be functioning outside of the Rod complexes in a spatially unorganized manner similar to aPBPs, that is, not associated with the directionally moving MreB complexes. Previous studies of PBP2A and RodA in both B. subtilis and E. coli have reported that there are both directionally moving as well as diffusive molecules of both proteins (Garner et al. 2011; Dominguez-Escobar et al. 2011; Cho et al. 2016).

We hypothesized that MreBCD levels affect the amount of directionally moving PBP2A, and that. To test this hypothesis, we created a functional HaloTag fusion to PBP2A expressed from the native promoter at the native locus, and placed it into strain bMD545 which has *mreBCD* expression controlled by xylose. In this strain bMK385 (*amyE*::P_{xyl}-*mreBCD*::*erm* Δ*mreBCD::spec pbpA::HaloTag-11aa-pbpA*), we found that PBP2A dynamics were dependent on the amount of MreBCD induction. At very low levels of MreBCD, the majority of PBP2A molecules moved diffusively across the surface of the cell. At intermediate levels of MreBCD induction, there was a mixed population of diffusively and directionally moving PBP2A molecules, and higher MreBCD induction overexpression of caused the fraction of circumferentially moving PBP2A molecules to increase further (Fig. 4.6A, B).

This suggests that MreBCD levels are directly related to how many PBP2A molecules can participate in directionally moving Rod complexes: at low MreBCD levels, most PBP2A molecules are diffusive, and the frequency of directionally moving PBP2A increases as MreBCD levels increases, possibly because more binding sites become available for PBP2A.

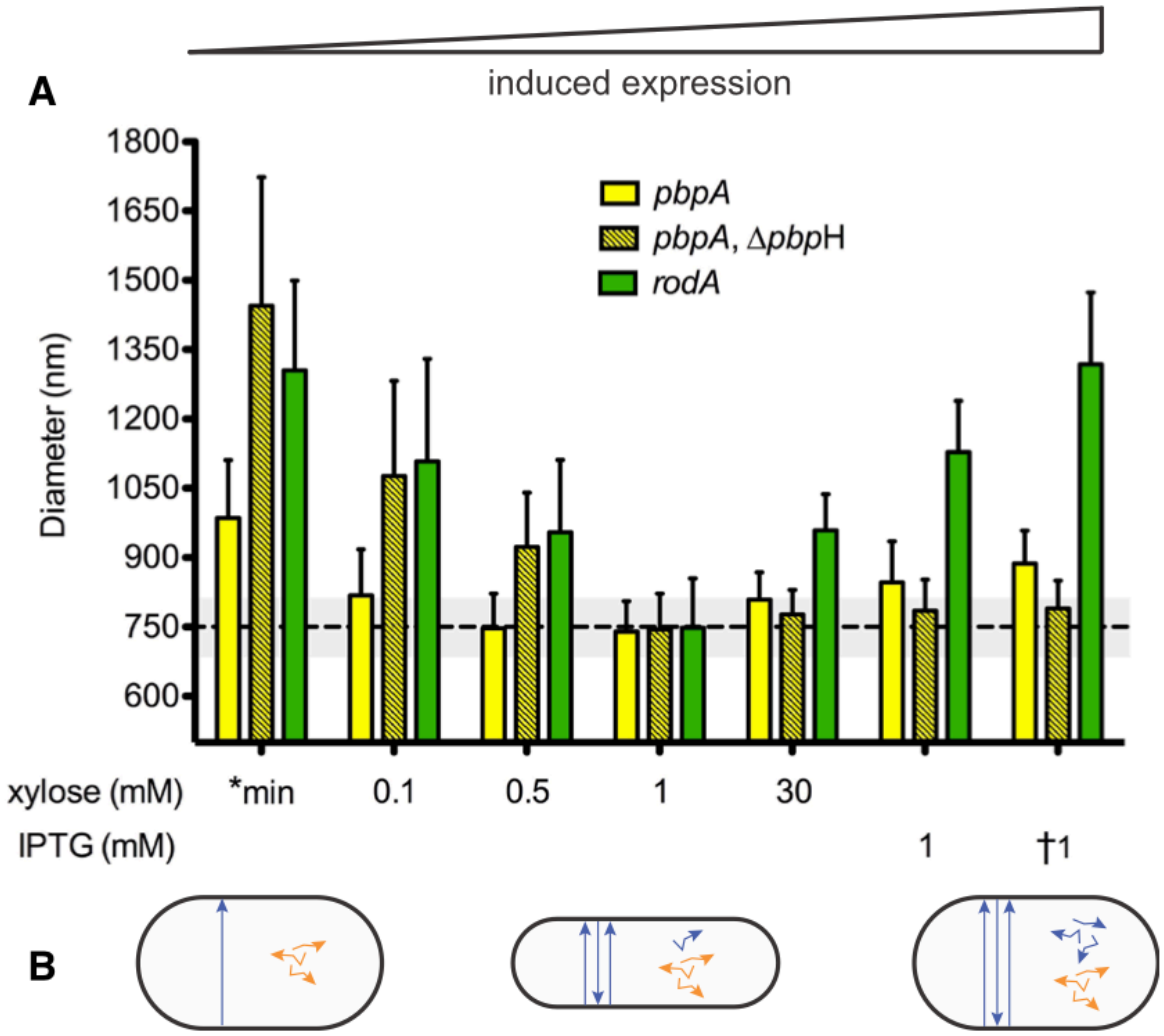


Figure 4.5. Steady-state diameter of cells increases when RodA/PBP2A expression is raised or lowered from wild type. a, The mean diameter of a population of cells decreases up to a point as the expression levels of *rodA* or *pbpA* are increased, beyond which cell diameter increases with rising expression levels. Green bars represent the steady state diameter of bMD592 at five different concentrations of xylose, and bMD580 and bMD556 (†**)** induced with IPTG. Yellow bars represent the steady state diameter of bMD590 at five different concentrations of xylose, and bMD572 and bMD563 (†**)** induced with IPTG. Yellow (shaded) bars depict the steady state diameter of bMD597 at five different concentrations of xylose, and bMD574 and bMD573 (†**)** induced with IPTG. The dashed line depicts the mean steady state diameter of PY79 (wild type) cells, and the gray shaded area represents the standard deviation of the data. For bMD592 and bMD597, *min represents 0.025 mM xylose, and for bMD590 *min represents 0 mM xylose. **b**, Schematic view of a possible model to explain these observations. Blue lines represent spatially organized synthesis and orange lines represent spatially unorganized synthesis; at low *rodA* or *pbpA* levels, organized synthesis is reduced; as *rodA* or *pbpA* levels are increased, Rod system synthesis increases, and beyond a point RodA and PBP2A also contribute to unorganized synthesis outside the Rod system.

If this hypothesis is correct, then providing more MreBCD for excess RodA/PBP2A to bind to should recruit their activity to the directed Rod system and thus lead to a narrowing of cell diameter. Indeed, when we simultaneously overexpressed RodA or PBP2A with MreBCD in the strains bMD557 (*yhdH*:: P_{hyp}-*rodA*::*cat amyE*::P_{hyp}-*mreBCD*::*erm*) and bMD571 (*yhdH*:: P_{hyp}-*pbpA*::*cat amyE*::P_{xyl}-*mreBCD*::*erm*), cell diameter returned to wild type, even at a RodA/PBP2A expression level that led to a significant increase in the diameter of the parental strains (Fig 4.6C). This suggests the "widening" activity of PBP2A/RodA takes place only once their expression level exceeds that of MreBCD, and when their participation in Rod complexes is saturated.

Past work by others and us has suggested that RodA and PBP2A must form complexes in order to synthesize peptidoglycan (Fay et al. 2010; Fraipont et al. 2011). While both proteins have been observed to move directionally around the rod-shaped cell with MreB, we wondered if, at higher levels, exceeding the amount of MreB, the "widening" activity of RodA required PBP2A. To create strain bMD627 (*rodA*:: P_{xyl}-*rodA*::*erm* Δ*pbpH::spec*), we placed the xylose-inducible *rodA* allele in a genetic background where PBP2A was the only elongation-specific bPBP (a strain lacking *pbpH*). In this background, as in wild type, depletion or overexpression of RodA caused cell diameter to increase, similar to results in Fig 4.5. However, simultaneously placing *pbpA* under an IPTG-inducible promoter in bMD631 (*rodA*:: P_{xyl}-*rodA*::*erm yhdG*::P_{spa}-*pbpA::phleo* Δ*pbpH::spec*) revealed that when PBP2A levels are limiting, RodA overexpression does not cause cell diameter to increase (Fig. 4.7). When PBP2A expression was held at the lowest level sufficient to produce wild type diameter (15 μM IPTG), and RodA was simultaneously overexpressed, cells remained at wild type diameter. Increasing PBP2A expression to the maximum level that still produces wild type cells removed this limitation, and

RodA overexpression now produced wider cells. This suggests that the "widening" activity of RodA requires PBP2A.

Discussion

The steady-state cell volume of *B. subtilis*, like that of several other microbial species, increases as a function of nutrient-imposed growth rate (Sharpe et al. 1998; Vadia & Levin 2015). However, *B. subtilis* is notable for the fact that it maintains a constant diameter across different growth conditions, only altering its steady-state length in response to changes in nutrient availability (Sharpe et al. 1998). Although MreB has been assigned a diameter-maintenance function in a variety of rod-shaped bacteria (Typas et al. 2012), this assigned function does not explain what determines the diameter that MreB filaments maintain (Harris et al. 2014). Here we show that the balance between spatially organized peptidoglycan synthesis by the Rod system and unorganized synthesis by aPBPs determines the steady-state diameter of *B. subtilis*.

The shape and diameter of *B. subtilis* cells arises from the shape and diameter of their cell walls; our results suggest that the two distinct, spatially separable cell wall synthesis machineries contribute differently to create these features. The Rod system, by dint of its MreB-mediated circumferential motion, creates radial hoops of cell wall around the rod, and our data suggest this activity serves to squeeze the cell, reducing the rod diameter. By contrast, the motion of aPBPs does not appear to be spatially patterned, and thus their activity widens the cell. They may serve to provide bulk material for the sacculus and/or fill in holes and gaps that have appeared due to damage.

We propose that the balance between these two kinds of syntheses is what creates a

uniform, rod-shaped cell of a given width: aPBPs create bulk material that tend to enlarge the sacculus isotropically into a sphere, while radial hoops created by the Rod system enforce structural anisotropy, forcing the meshwork into a cylindrical shape and reducing its diameter.

When the balance between these two systems is disturbed, the shape of the sacculus is altered. This explains why loss-of-function mutations, genetic depletions, and chemical treatments disrupting Rod system activity all result in cells that swell isotropically to become spherical (Henriques et al. 1998; Lee & Stewart 2003; Leaver & Errington 2005; Dye et al. 2011; Harris et al. 2014; Meeske et al. 2016): in the absence of belting/tightening hoops made by the Rod system, aPBP-mediated synthesis adds new peptidoglycan uniformly over the surface of the cell. Indeed, we found that simultaneously depleting aPBP activity in cells depleted for Rod activity prevented cells from swelling. Importantly, lower levels of both aPBPs and Rod components can support growth as rods of wild type diameter, just at a slower rate – we presume the rod shape and diameter comes from a balanced level of enzymes, and the reduction in growth rate comes from the overall total reduction in PG synthetic activity. This finding explains why *ponA* mutations can rescue *mreB* knockouts: crippling each system can lead to normal shape and viability (Kawai et al. 2009).

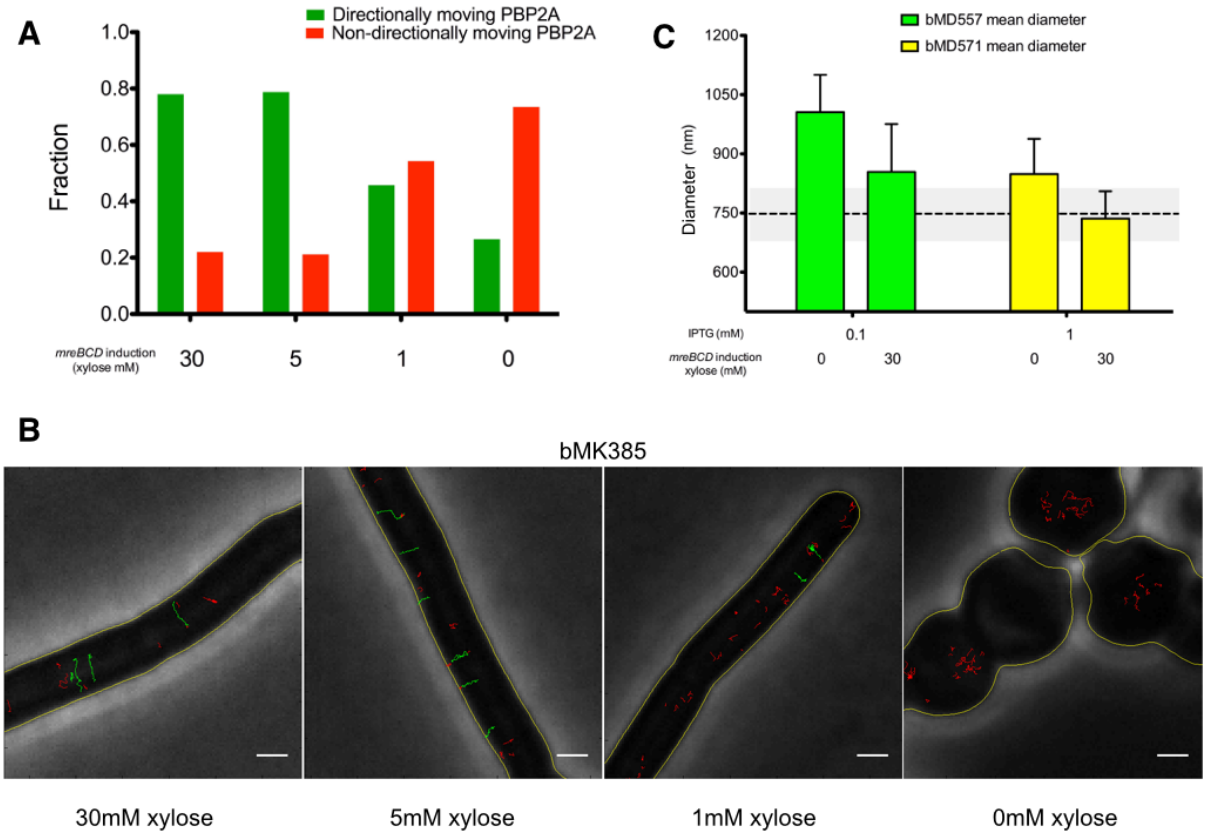


Figure 4.6. RodA/PBP2A participation in the rod complex is dependent on the expression level of *mreBCD*. A, The directionally moving fraction of all Halo-PBP2A molecules that can be reliably tracked increases with *mreBCD* expression. At very low expression, most molecules are non-directional; at highest expression, most molecules are directional. Halo-PBP2A was labeled with JF-549 and cells were imaged by TIRF microscopy using 300 msec continuous exposures. **B,** Representative montage of tracks of Halo-PBP2A under different levels of *mreBCD* induction in bMK385. Tracks that passed cutoffs to be designated as directionally moving are labeled in green; all other tracks are labeled in red. Scale bar = 1 μm. **C**, The increase in cell diameter caused by overexpression of *rodA* (green bars) in bMD557 or *pbpA* (yellow bars) in bMD571 is restored by simultaneous overexpression of *mreBCD*. The dashed line depicts the mean steady state diameter of PY79 (wild type) cells, and the gray shaded area represents the standard deviation of the data.

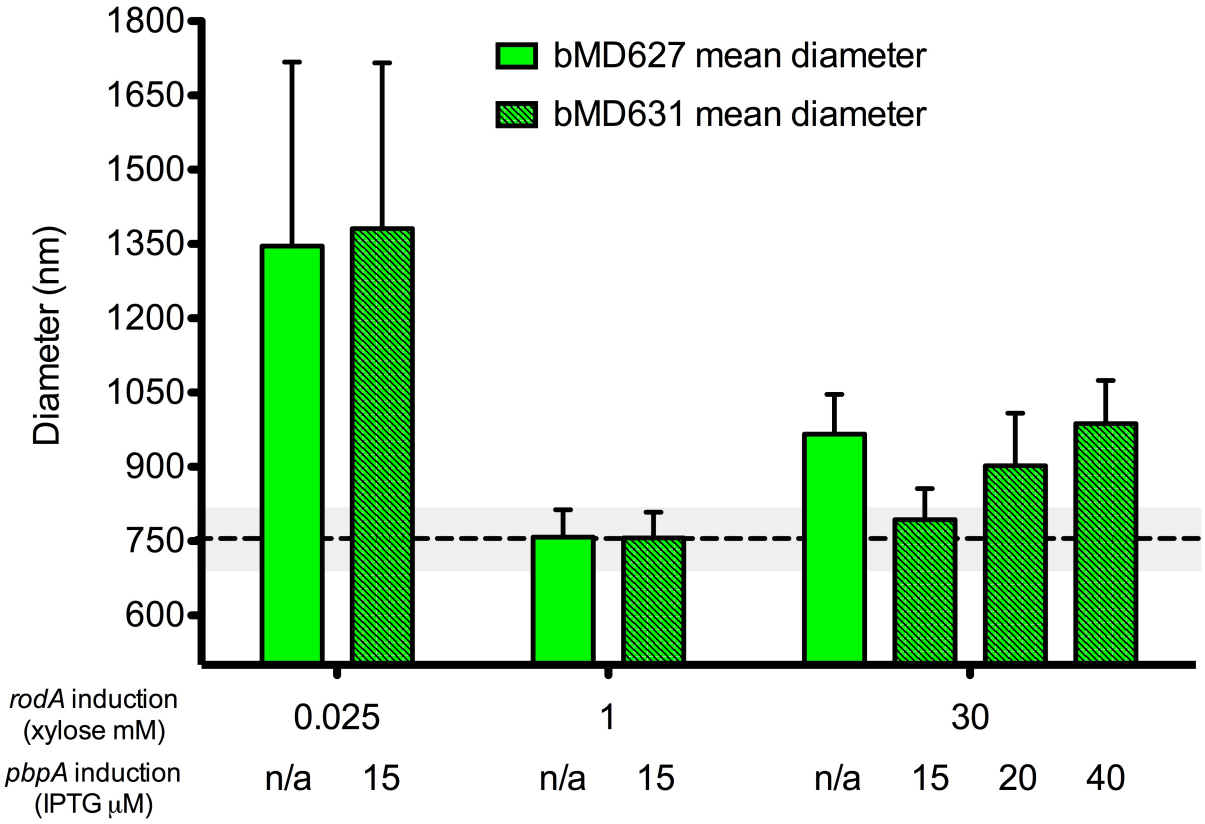


Figure 4.7. Rod-system independent activity of RodA and PBP2A requires both enzymes. Overexpression of *rodA* only causes cell diameter to increase when *pbpA* expression is also sufficiently high. Light green bars represent the steady state diameter of bMD627 at specified concentrations of xylose. Dark green bars represent the steady state diameter of bMD631 at the specified concentrations of xylose and IPTG. The dashed line depicts the mean steady state diameter of PY79 (wild type) cells, and the gray shaded area represents the standard deviation of the data. Error bars represent standard deviation.

Furthermore, this model can also explain the decades-old observation that aPBP activity, though essential in most species, is not required to maintain rod shape. *Escherichia coli* cells disrupted for aPBP activity lyse as rods (Cho et al. 2016), possibly because of their inability to repair damage or to expand the sacculus at a rate sufficient to match that of cell expansion; moreover, cells do not swell or lose shape even though Rod system activity continues unabated until death (Cho et al. 2016), because the effect of this activity on the shape of the sacculus is to

"squeeze" it inwards.

Our results also offer an explanation for the observation that RodA overexpression compensates for aPBP activity in *B. subtilis* (Meeske et al. 2016): as RodA expression is increased beyond the point where all binding sites in the Rod system are occupied, excess RodA/PBP2A can function independently outside the Rod system. This creates unpatterned peptidoglycan in the manner of aPBPs, providing bulk material, filling gaps, and restoring the balance of undirected and directed synthesis to restore cell diameter. Finally, these observations explain why *B. subtilis* is viable without aPBPs. In their absence, RodA expression is upregulated via the σM-response (Meeske et al. 2015; Meeske et al. 2016) to provide unpatterned synthesis; further overexpression bolsters this contribution, restoring the diameter of the sacculus to a state resembling wild type. Crucially, depleting RodA in the absence of aPBPs was recently shown to result in lytic death without swelling (resembling death of *E. coli* lacking aPBPs), likely due to the complete absence of unpatterned synthesis (Emami et al. 2017).

The data presented here offers suggestions as to the relationship between aPBPs and the Rod system. Both machineries utilize the same precursor, Lipid II, and are thus dependent on the same underlying chemical pathway (Typas et al. 2012). The output of both machineries is required to expand the sacculus at a rate sufficient to keep up with the rate of cytoplasmic and membrane expansion. When one system is partially disrupted, the precursor pool flows through the other (perhaps at an increased rate of flux) so the sacculus expansion proceeds at the same rate. Indeed, even upon deletion of all aPBPs, the single-cell growth rate is not significantly reduced; crucially, overexpression of RodA restores width, possibly by providing unpatterned synthesis and rebalancing the flux of precursors through the two machineries, but does not increase the growth rate of the sacculus. Only upon simultaneous depletion of aPBPs and the

Rod system is the single-cell growth rate significantly reduced. Further studies to measure the synthetic output of the two systems in the various conditions described in this report, as well as investigation of the follow-on effects of these conditions on the Lipid-II synthesis pathway will be required for a complete understanding of the regulation of the peptidoglycan synthesis system.

CHAPTER 5

Conclusion and future directions

A unified view of cell wall synthesis

At the time this research began, it was thought that the organization of cell wall synthesis differed in the gram-negative and gram-positive model organisms *E. coli* and *B. subtilis*. Besides the key role of MreB filaments in forming short, dynamic filaments that traverse the cell in circumferential paths, there were major disparities between the models for cell wall synthesis in the two species. In *B. subtilis*, several other shape-determining proteins such as MreC, MreD, RodA, and the bPBPs (PBP2A and PBPH) had been shown to move circumferentially around the cell, and as such, were thought to associate stably with Rod complexes (Garner et al. 2011; Domínguez-Escobar et al. 2011). PBP1, an aPBP, had also been reported to be recruited to MreB structures, although this observation had been made with older, oligomerization-prone fluorescent proteins (Kawai et al. 2009) (Fig. 5.1), and within the old context of a contiguous, cell spanning spiral of MreB.

On the other hand, in *E. coli*, no PBP, or component of the Rod complex other than MreB had been found to display circumferential, MreB-like motion. Indeed, one study, examining the motions of PBP2 saw only diffusive motion, with no change in motion upon inhibition of transpeptidase activity. This led to an entirely different model for the organization of peptidoglycan synthesis in *E. coli*, where PBP2 molecules diffused rapidly over the surface of the cell, yet interacted transiently with MreB filaments to cross-link peptidoglycan and drive the motion of MreB (Lee et al. 2014) (Fig. 5.2).

In Chapter 3, our studies provided clear support for a unified view: in both *E. coli* and *B.*

subtilis, the overall spatial organization of cell wall synthesis is similar (Figs 5.1 and 5.2). The Rod system and aPBPs constitute spatially distinct machineries that do not require each other to function (Cho et al. 2016). In both species, RodA and bPBP molecules associate with the Rod complex for long, measurable periods of time as evidenced by a) their circumferential motion around the rod and b) the dependence of MreB motion on their activity. On the other hand, aPBPs do not interact stably with Rod complexes in both species, instead displaying two types of motion, 1) transient immobility on the timescale of seconds, and 2) rapid, diffusive motion, an observation later verified by the Huang group (Cho et al. 2016; Lee et al. 2016).

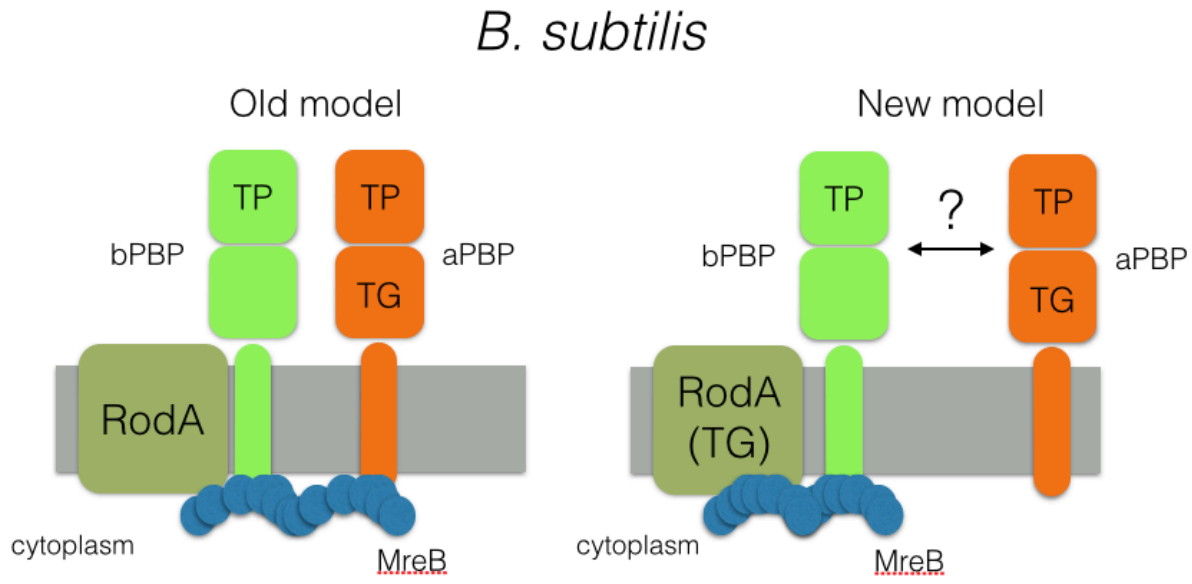


Figure 5.1. Old and revised models of cell wall synthesis in *B. subtilis*. In the old model (left), the Rod complex contained bifunctional aPBPs with both transpeptidase (TP) and transglycosylase (TG) domains, monofunctional bPBPs with a TP domain, and RodA, a conserved SEDS family protein of unknown function. In the revised model (right), the Rod complex contains bPBPs only, and RodA is the source of TG activity. aPBPs are depicted as spatially distinct, and it is unknown whether there is collaboration/interaction between them and the Rod system via second messengers or structural cues.

Cell diameter of *B. subtilis* arises from a balance between two independent cell wall synthesis machineries

Our finding, along with concurrently published *in vitro* evidence (Meeske et al. 2016), indicated that RodA is a transglycosylase enzyme that works together with bPBPs led us to a new model for how cell diameter is determined. We can infer something about the nature of the contribution of the two cell wall biogenesis machineries from their subcellular dynamics: aPBPs create bulk material homogeneously over the cylindrical surface of the cell, while the Rod system creates tightening, squeezing radial hoops of peptidoglycan. In Chapter 4, we showed that the relative levels of these two activities have predictable effects on the steady-state diameter of cells. Moreover, our results suggested that when present in excess, RodA and PBP2A are in fact capable of polymerizing peptidoglycan outside of Rod complexes, and also showed that outside the complex, RodA requires bPBP activity to increase cell diameter and size.

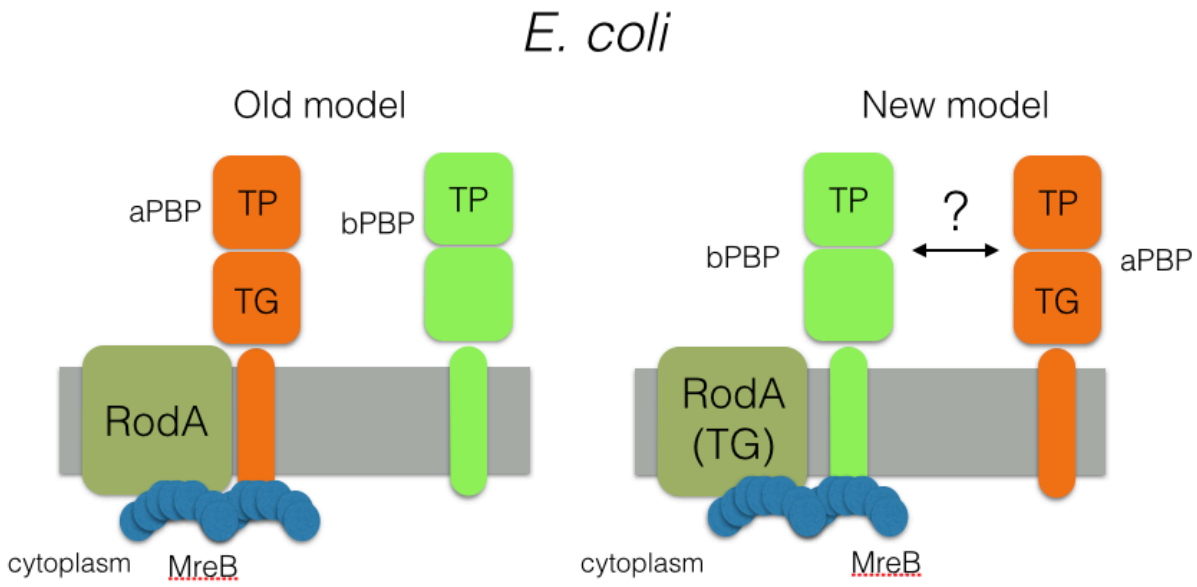


Figure 5.2. Old and revised models of cell wall synthesis in *E. coli*. In the old model (left), the Rod complex contained bifunctional aPBPs and RodA, while bPBPs were thought to be spatially distinct enzymes that interacted only transiently with MreB. In the revised model (right), the Rod complex contains bPBPs instead, and RodA is the source of TG activity. aPBPs are depicted as spatially distinct, and it is unknown whether there is collaboration/interaction between them and the Rod system.

New questions about the relationship between the two cell wall synthesis machineries

The findings from Chapters 3 and 4 lead to several other questions that are important in building a complete understanding of cell wall synthesis. Although the two machineries appear to be at least semi-autonomous, they are intrinsically dependent on the same underlying pool of peptidoglycan precursors. We still lack a clear understanding of how the cell controls the activities of the two machineries, and whether it is capable of altering the relative levels or activity of each in response to environmental or other stresses. However, MreB function is linked to precursor synthesis: depletion of precursors causes depolymerization of MreB filaments and therefore halts the functioning of the Rod system (Schirner et al. 2014). The mechanism that

causes MreB depolymerization is as yet undiscovered. Moreover, we do not yet understand if there exists a similar regulatory mechanism for aPBPs - do they also alter their activity based on the availability of precursors? Finally, given a set amount of Lipid II, is there a hierarchy or difference in preference between the two systems, or is the pool of precursors equally available to both?

An accurate systems-level model of cell wall synthesis will be invaluable for the development of new antibiotics. For example, our understanding of how beta-lactams kill cells has gradually evolved over the decades: the latest model posits that the inhibition of PBPs by beta-lactam induces their partner transglycosylases to enter a futile cycle of synthesis and degradation, thereby depleting the cell of resources (Cho et al. 2014). To rationally design combination therapies that target different components of the cell wall synthesis pathway, we need to understand how they relate to each other, and how inhibition of one might in fact lead to stimulation of another - and what ultimate consequence this has on the physiology of the cell.

The enigmatic ultrastructure of the cell wall - and why have aPBPs at all?

The numerous outstanding questions regarding the ultrastructure of the sacculus are linked to another fundamental question: what is the function of aPBPs?

First, are there ultrastructural/topological differences between peptidoglycan that is synthesized by the Rod system versus by spatially unorganized enzymes? And although RodA/PBP2A are capable of synthesizing peptidoglycan outside of Rod complexes (as aPBPs do), is this part of their normal function? That is, are native levels of RodA/PBP2A in excess to MreBCD levels, or is this activity merely limited to conditions of stress, such as lack of all aPBPs (Meeske et al. 2016) or artificial overexpression, as in Chapter 4?

Second, we still lack the methods capable of discerning the true nature of the topology of glycan strands. Beyond that of the chemical structure of the disaccharide-pentapeptide monomer unit itself, there is no understanding of how different glycan strands relate to each other: how are they aligned, and what is the nature and extent of connectivity between glycan strands? Third, we lack detailed information about how and where in the sacculus structure hydrolysis takes place, and to what degree it is coordinated with new insertion of material, if at all, as depletion of the 2 essential hydrolases in *B. subtilis* does not cause MreB motion to change until the point of cell death (Meisner et al. 2013)

The model described in Chapter 4 posits that the Rod system provides the basic radially arranged structural framework of the sacculus, while aPBPs provide unorganized bulk material to either fill gaps, or fix holes arising from damage or uncontrolled hydrolase activity. But if RodA/bPBPs can indeed synthesize peptidoglycan outside the context of the Rod system, then why did aPBPs evolve at all? Indeed, there do exist some species of bacteria that lack aPBP-like glycosyltransferases entirely, relying solely on SEDS proteins as a source of glycan strands (Meeske et al. 2016).

Lastly, the Rod system still contains several mysteries. It is highly likely that all the components of the peptidoglycan synthesis machinery have now been identified, yet many of them still have no assigned biochemical/biophysical function: MreC, MreD, and RodZ are all essential for rod-shape maintenance, and identifying their contributions will be crucial in developing a complete understanding of the operation of the Rod system.

APPENDIX

Supplementary materials for Chapter 3: Two spatially distinct cell wall synthesis machineries

---

Acknowledgements

The authors would like to thank all members of the Bernhardt, Rudner, and Garner labs for helpful advice and discussions. We also thank Piet de Boer and Cynthia Hale for the gift of the *mreB*::*galK* strain for constructing sandwich fusions. We thank Luke Lavis for his generous gift of JF dyes. This work was supported by the National Institutes of Health (R01AI083365 to TGB, AI099144 to TGB, CETR U19 AI109764 to TGB, and DP2AI117923 to ECG). ECG was also supported by a Smith Family Award and a Searle Scholar Fellowship. PDAR was supported in part by a pre-doctoral fellowship from CHIR. JAM was supported by Dana-Farber Strategic Research Initiative.

Methods

Media, bacterial strains, plasmids, and culture conditions for *E. coli* strains.

Cells were grown in LB (1% tryptone, 0.5% yeast extract, 0.5% NaCl) or minimal M9 medium supplemented with 0.2% casamino acids (CAA) and carbon source (0.4% glycerol or 0.2% glucose or maltose) as indicated. The bacterial strains and plasmids used in this study are listed in Tables A.2 and A.3, respectively, and a description of their construction or isolation in the genetic selection is given below.

Construction of *E. coli* strains with multiple deletions

E.coli strains with multiple deletion mutations were made by sequential introduction of each deletion from the Keio mutant collection (Baba et al. 2006) via P1 transduction followed by removal of the *aph* cassette using FLP expressed from pCP20, leaving a *frt* scar sequence at each deletion locus. Correct orientation of the DNA flanking *frt* sequences in multiple deletion mutants was confirmed for all the deletions in each mutant.

Construction of an MTSES-sensitive *E. coli* PBP1b variant

To test the effect of aPBP inhibition on cell wall synthesis and turnover, we sought a way to rapidly block the PGT activity of aPBPs. Moenomycin, a known inhibitor of the PGT activity of aPBPs, is not ideal for aPBP inhibition in WT *E.coli* because it cannot cross the outer membrane layer to access aPBPs. Instead, it was recently shown that a small cysteine-reactive molecule, MTSES [sodium (2-sulfonatoethyl)methanethiosulfonate], can be used in conjunction with a cysteine-substitution mutant to specifically block the activity of a surface exposed enzyme (Sham et al. 2014). PBP1B was chosen for the development of a MTSES-blockable aPBP system because it is the major aPBP in *E.coli* and a structural information was also available for this protein (Sung et al. 2009). Thirteen cysteine substitution variants of PBP1b were constructed with changes mapping within the moenomycin binding surface of PBP1B (Sung et al. 2009). Alleles encoding each variant were cloned under control of the *lac* promoter in the CRIM plasmid pHC872 backbone (*attHK022*, P_{lac}::*ponB*) and the resulting plasmids were integrated into HC518 [Δ*ponA*::*frt* P_{ara}::*ponB*]. The functionality of each *ponB* allele was assessed by testing their ability to correct the PBP1a- PBP1b- synthetic lethality of HC518 grown on M9 glucose minimal medium supplemented with 100 μM IPTG.

Cysteine substitution mutants that were functional were further screened for the loss of activity upon MTSES treatment. This screen utilized the rapid lysis phenotype manifested in cells inhibited for aPBP activity in combination with 10 μg/mL cephalexin.
Treatment of WT *E.coli* with 10 μg/mL cephalexin causes continued growth as cell filaments. However, lysis is observed in 20 min when aPBPs are also inhibited. We therefore screened the functional PBP1b cysteine substitution mutants for their response to treatment with 10 μg/mL cephalexin with or without 1mM MTSES using a VersaMax microplate reader (Molecular Devices). PBP1b(S247C) was identified as a variant that supports the growth similar to WT PBP1b but specifically leads to rapid lysis when cells producing the variant as the main aPBP are treated with 10 μg/mL cephalexin and 1mM MTSES.

Introducing *ponB(S247C)* mutation at the native *E. coli* locus

Allele exchange of *ponB(247C)* at the native locus was performed by using a temperature-sensitive plasmid pMAK700 as described (Cho et al. 2011). Eighteen hundred bases of DNA flanking the *ponB(S247C)* mutation were PCR amplified from pHC873 using primers 5'-GCTA*ATCGAT*GAAAATCGGGCTTTTGCGCCTGAATATTGC-3' and 5'-GCTA*GCTAGC*AGATTTACCGTCGGCACGTTCATCG-3'. The resulting PCR product was digested with NheI and ClaI and ligated with pMAK700 digested with the same enzymes to generate pHC878. Plasmid integration and excision events at the *ponB* locus were selected utilizing the temperature-sensitive replication initiation of pHC878 to obtain strains with *ponB(S247C)* mutation at the native chromosomal locus.

Introduction of the *imp4213* allele

The *imp4213* allele was introduced into recipient strains by P1 transduction using its genetic linkage to *leu* marker. First, a *leu::Tn10* marker was introduced into the recipient strains by selecting for tetracycline resistance. Then, *imp4213* was introduced into the *leu* auxotrophs by P1 transduction followed by selection for leucine prototrophy on M9-glucose agar plates. For efficient P1 lysate preparation from an *imp4213* strain, a strain that has a suppressor mutation at the *bamA* locus in addition to *imp4213* (JAB027) was used. The resulting P1 transductants were screened for the sensitivity to 10 μg/mL erythromycin to identify isolates that acquired *imp4213* allele along with the WT *leu* locus.

Generation of *mreB* sandwich fusions at the native *E. coli mre* locus

Sandwich fluorescent protein fusions of *mreB* were introduced at the native locus using the recombineering strain CH138/pCX16, which harbors a defective lambda prophage as a temperature-inducible source of the recombination genes (Warming et al. 2005). CH138/pCX16 is also deleted for native *galK* and has a *galK* cassette inserted in the middle of *mreB* (replacing the codon for G228). The strain is viable due to suppression of the Rod system defect by elevated FtsZ levels promoted by *sdiA* on pCX16. Fragments with one kb of sequence flanking *mNeonGreen* or *mCherry* in plasmid-borne *mreB*-fluorescent protein sandwich fusions were amplified with the primers 5'-AACGGTGTGGTTTACTCCTCTTCTGTG-3' and 5'-TTCCAGTGCAACCATTACCGCGCTCAC-3' using pFB262 or pHC892 as templates. After the recombineering with the resulting PCR products, cells that replaced *galK* with fluorescent protein fusions at the *mreB* locus were selected on M9 minimal agar containing 0.2% 2-deoxy-galactose, which is converted to toxic 2-deoxy-galactose-1-phosphate if cells remain GalK+.

Generation of *E. coli ΔrodA::aph*

A *rodA* deletion was constructed similar to deletions in the Keio collection (Baba et al. 2006) using a TB10(attHKCS8) recombineering strain that expresses *rodA* under control of the *lac* promoter. A PCR product for *ΔrodA::aph* construction was amplified using pKD13 (Datsenko & Wanner 2000) as a template with the primers 5'-AAAATCCAGCGGTTGCCGCAGCGGAGGACCATTAATCATGATTCCGGGGATCCGTCGACC-3' and 5'-CTTACGCATTGCGCACCTCTTACACGCTTTTCGACAACATTGTAGGCTGGAGCTGCTTCG-3' and recombineering was performed as described previously (Yu et al. 2000).

***E. coli* plasmid construction**

pHC872 and pHC873

The *ponB* gene was amplified with primers 5'-GTCA*TCTAGA*GAAAATCGGGCTTTTGCGCCTG-3' and 5'-GTCA*CTCGAG*ATGGGATGTTATTTTACCGGATGGC-3'. The resulting fragment was digested with XbaI and XhoI and ligated to pTB183 digested with XbaI and SalI to generate pMM15. The *bla* antibiotic resistance cassette of pMM15 was replaced with a *cat* cassette from pHC514 by replacing the NotI-XbaI fragment to generate pHC872. The *ponB(S247C)* mutation was introduced in pHC872 using QuikChange mutagenesis with the primer 5'-CATGATGGAATCAGTCTCTACTGCATCGGACGTGCGGTGCTGGCA-3' to generate pHC873.

pHC897

The *mCherry* sequence of pFB262 was replaced with *E.coli* codon-optimized *mNeonGreen* (IDT synthesis) using XhoI and AscI to generate pHC892. The *mreB-*^{SW}*mNeon* fragment of pHC892 was removed with XbaI and HindIII and cloned under control of the *lac* promoter of a pHC514 derivative to generate pHC897.

pHC929

The *mreB-*^{SW}*mNeon* fragment was liberated from pHC892 by digestion with XbaI and HindIII and *tetR*-P_{tetA} (IDT synthesis) digested with BglI and XbaI were assembled in a pTB183 derivative using BglII and HindIII to generate pHC929.

pHC938

pHC938 was generated by introducing the *rodA(D262N)* mutation into pHC857 using an overlap extension mutagenesis protocol. *rodA(D262N)* was amplified using primers 5'-AAATCC*GGTACC*GCTCAGGTC-3' and 5'-GTATCGGTGAT*AAGCTT*CTGC-3' and a mutagenizing primer set 5'-CCGAACGCCATACT**A**ACTTTATCTTCGCGGTACTGG-3' and 5'-GCGAAGATAAAGTT**T**AGTATGGCGTTCGGGGAGAAATTC-3'. The mutated base is indicated in bold. The resulting PCR product for *rodA(D262N)* was digested with KpnI and HindIII and ligated to pHC857 digested with the same enzymes to generate pHC938.

pHC933

The *sfgfp* fragment was liberated from pTB230 with XbaI and BamHI digestion and *rodA* amplified with 5'-GTCA*GGATCC*GAGGCCATTACGGCCATGACGGATAATCCGAATAAAAAAACATTCTGGG-3' and 5'-GTCA*GTCGAC*TTATTATTGGCCGAGGCGGCCTTACACGCTTTTC-3' and digested with BamHI and SalI. The fragments were assembled in pNP20 using XbaI and SalI to generate pHC933.

pHC942, pHC943, and pPR104

E.coli codon-optimized *msfgfp* (IDT synthesis) digested with XbaI and BamHI, and the *ponB* sequence amplified with 5'-GTAC*GGATCC*CCGCGCAAAGGTAAGGG-3' and 5'-GTCA*CTCGAG*ATGGGATGTTATTTTACCGGATGGC-3' and digested with BamHI and XhoI were assembled in pNP20 by using XbaI and SalI to generate pHC942. The *ponB* of pHC942 was then replaced with *pbpA* sequence amplified with 5'-GCTA*GGATCC*AAACTACAGAACTCTTTTCGCGACTATACG-3' and 5'-CTTCACGTTCGCTCGCGTATCGGTG-3' using BamHI and HindIII to generate pHC943. pPR104 was constructed by replacing *ponB* of pHC942 with *ponA* sequence amplified with 5'-GCTA*GGATCC*AAGTTCGTAAAGTATTTTTTGATCC-3' and 5'-GCTA*AAGCTT*AGAACAATTCCTGTGCCTCGCCAT-3' using BamHI and HindIII.

pHC949

HaloTag sequence was amplified by using pDHL940 as a template with 5'-GCTATCTAGATTTAAGAAGGAGATATACATATGGCAGAAATCGGTACTGGCTTTCCA

TTC-3' and 5'-GCTAGGATCCGGAAATCTCCAGAGTAGACAGC-3'. The resulting PCR product was digested with XbaI and BamHI, and ligated to pHC942 digested with the same enzymes to replace msfgfp sequence with HaloTag sequence.

Measurement of PG synthesis and turnover

The effect of blocking aPBP activity with MTSES on PG synthesis and turnover in beta-lactam-treated *E.coli* cells was examined essentially as described previously [15]. HC533(attλHC739), a *ΔlysA ΔampD* strain which expresses PBP1b(S247C) as a sole aPBP, was grown overnight in M9-glycerol medium supplemented with 0.2% casamino acids. The overnight culture was diluted to an OD_{600} = 0.04 in the same medium and grown to an OD_{600} between 0.26 - 0.3. Then, divisome formation was blocked by inducing *sulA* expression for 30 min from a chromosomally integrated P_{tac}::*sulA* construct (pHC739) by adding IPTG to 1 mM. After adjusting the culture OD_{600} to 0.3, MTSES (1mM), A22 (10 μg/mL), mecillinam (10 μg/mL), and/or cefsulodin (100 μg/mL) were added to the final concentrations indicated and cells were incubated for 5 min. Following drug treatment, 1 μCi of [^{3}H]-meso-2,6-Diaminopimelic acid (mDAP) was added to 1mL of each drug-treated culture and incubated for 10 min to label the newly synthesized PG and its turnover products. After the labeling, cells were pelleted, resuspended in 0.7 ml water, and heated at 90°C for 30 min to extract water-soluble compounds. After the hot water extraction, insoluble material was pelleted by ultracentrifugation (200,000 x g for 20 min at 4^{o}C). The resulting supernatant was then removed, lyophilized, and resuspended in 0.1% formic acid for HPLC analysis and quantification of turnover products as described previously [15]. To determine [^{3}H]-mDAP incorporated into the PG matrix, the pellet fraction was washed with 0.7 mL buffer A (20 mM Tris-HCl, pH 7.4, 25 mM

NaCl) and resuspended in 0.5 mL buffer A containing 0.25 mg lysozyme. The suspensions were incubated overnight at 37°C. Insoluble material was then pelleted by centrifugation (21,000 x g for 30 min at 4°C), and the resulting supernatant was mixed with 10 mL EcoLite (MP biomedicals) scintillation fluid and quantified in Microbeta Trilux 1450 liquid scintillation counter (Perkin-Elmer).

Quantification of MTSES labeling of PBP1b(S247C)

To quantify the efficiency of MTSES binding to PBP1b(S247C) under experimental growth conditions, a culture of HC533(attλHC739) (100 mL) was grown to OD_{600} = 0.3 in M9-glycerol medium supplemented with 0.2 % casamino acids at 30°C with *sulA* induction for 30 minutes. Then, the culture was split into two 50 mL portions and treated with either 1mM MTSES or DMSO for 5 min. Immediately after MTSES/DMSO treatment, cultures were cooled on ice and cells pelleted at 4,000 x g for 5 min at 4°C. The cell pellets were washed once with 1X ice-cold PBS, resuspended in 500 µL 1X PBS containing 10 mM EDTA and 20 mM 2-iodoacetamide, and incubated for 20 min at room temperature to alkylate the cysteine residues not modified by MTSES. After the 20 min incubation, 20kU of Ready-lyse lysozyme (Epicentre) was added to each cell suspension and incubation was continued for a further 10 min at room temperature. Cells were disrupted by sonication and membrane fractions were pelleted by ultracentrifugation at 200,000 X g for 20 min at 4°C. The membrane fractions were then washed with 1X PBS once and resuspended in 1 mL immunoprecipitation (IP) buffer (100mM Tris, pH7.4, 300mM NaCl, 2% Triton X-100). Ten micrometers of anti-PBP1b antiserum was added to the resuspension and the resuspension was incubated overnight in the cold room with gentle agitation. The samples were then mixed with 50 µL of IP buffer-equilibrated protein A/G

magnetic beads (Millipore) and incubated for further 4 hrs in the cold room with gentle agitation. Then, the beads were washed three times with IP buffer and then three times with a buffer containing 100mM Tris, pH7.4 and 300mM NaCl.

Proteins bound on the beads were fragmented by on-bead digestion with 0.1µg trypsin (#V511C, Promega) in 300µl buffer (20mM Tris-HCl, pH8, 150mM NaCl) overnight at 37°C with gentle agitation. After digestion, peptide samples were acidified with 10% TFA to a pH between 1-2, desalted using a 96-well plate embedded with C18 resin (Thermo Scientific) and dried by vacuum centrifugation. Samples were resolubilized in 20 µl of 0.1% TFA and 5 µl of each sample was analyzed by nanoLC-MS/MS (Ficarro et al. 2009) with a HPLC gradient (NanoAcquity UPLC system, Waters; 5%–35% B in 110min; A=0.1% formic acid in water, B=0.1% formic acid in acetonitrile). Peptides were resolved on a self-packed analytical column (50cm Monitor C18, Column Engineering) and introduced to the mass spectrometer (Q Exactive HF) at a flow rate of 30 nl/min (ESI spray voltage=3.5kV). The mass spectrometer was programmed to operate in data dependent mode such that the ten most abundant precursors in each full MS scan (resolution=120K; target=5e5; maximum injection time=500ms; scan range= 300 to 2,000 m/z) were subjected to HCD (resolution=15K; target=5e4; maximum injection time=200ms; isolation window=1.6m/z; NCE=27, 30; dynamic exclusion=15seconds). MS/MS spectra were matched to peptide sequences using Mascot (version 2.2.1) after conversion of raw data to .mgf using multiplierz scripts (Askenazi et al. 2009). Search parameters specified trypsin digestion with up to two missed cleavages, as well as variable oxidation of methionine and carbamidomethylation of cysteine residues. Precursor and product ion tolerances were 10 ppm and 25 mmu, respectively. Targeted scan experiments were performed in a similar fashion while dynamic exclusion was disabled and inclusion was enabled for the following peptides:

HFYEHDGISLYCIGR (carbamidomethyl cysteine: z=4, m/z=467.4703; z=3, m/z=622.9579; z=2, m/z=933.9332), HFYEHDGISLYCIGR (MTSES-cysteine: z=4, m/z=488.2050; z=3, m/z=650.6042; z=2, m/z=975.4026), VWQLPAAVYGR (z=2, m/z=630.3484), LLEATQYR (z=2, m/z=497.2718), QFGFFR (z=2, m/z=401.2058), DSDGVAGWIK (z=2, m/z=524.2589). Peak area integration was carried out using the Thermo Xcalibur Qual Browser (version 3.0.63, Thermo Fisher Scientific).

Bocillin-binding assays

Cultures of HC545, HC596(attHKHC943), and HC576(attHKHC942) were grown overnight at 37°C in M9-glucose medium supplemented with 0.2% casamino acids, with induction of *msfgfp-pbpA* or *msfgfp-ponB* with 25 μM IPTG. Cells in the overnight cultures were washed to remove IPTG and diluted to an OD_{600} = 0.001 in 15 ml of M9-glucose medium supplemented with 0.2% casamino acids and the indicated concentrations of IPTG. The cultures were then incubated at 37°C until the OD_{600} reached 0.4 to 0.5. A subset of cultures were treated with 10 μg/mL mecillinam (specific for PBP2) or 100 μg/mL cefsulodin (specific for PBP1b) for 5 min prior to harvesting. Cells were then harvested by centrifugation at 4°C, washed with ice-cold 1X phosphate-buffered saline (PBS) twice, resuspended in 500 μL 1X PBS containing 10 mM EDTA and 15 μM Bocillin (Invitrogen), and incubated at room temperature for 15 min. After the incubation, the cell suspensions were washed with 1X PBS once, resuspended in 500 μL 1X PBS, and disrupted by sonication. After a brief spin for 1 min at 4,000 X g to remove undisrupted cells, membrane fractions were pelleted by ultracentrifugation at 200,000 X g for 20 min at 4°C. The membrane fractions were then washed with 1X PBS and resuspended in 50 μL 1X PBS. Resuspended samples were mixed with 50 μL 2X Laemmli sample buffer and boiled

for 10 min at 95°C. After measuring the total protein concentrations of each sample with NI-protein assay (G-Biosciences), 25 μg of total protein for each sample was then separated on a 10% SDS-PAGE gels and the labeled proteins were visualized using a Typhoon 9500 fluorescence imager (GE Healthcare) with excitation at 488 nm and emission at 530 nm.

Bocillin-binding assays for *Bacillus subtilis* strains were performed basically in the same way as in *E.coli* strains. Overnight cultures grown in CH medium at room temperature were diluted to OD_{600} = 0.04 - 0.07 in 5 mL fresh CH medium containing the indicated concentrations of IPTG and incubated at 37°C. When the cultures reached exponential phase, cells were pelleted, washed with ice-cold 1X PBS, and resuspended with 100 μL 1X PBS containing 15 μM Bocillin (Invitrogen), and incubated for 15 min at room temperature. Then, cells were washed in 1X PBS, resuspended 0.5 mL 1X PBS containing 20kU Ready-lyse lysozyme (Epicentre), and incubated for 15 min at room temperature. The cells were disrupted by sonication and the membrane fraction was isolated by ultracentrifugation. A total of 16 μg of protein for each sample was separated on a 10% SDS-PAGE gels and visualized as described above for *E. coli*.

Microscopy of *E. coli* cells

Overnight cultures with strain-specific inducer levels were diluted in fresh culture medium and grown for at least 3 hours at 37 °C to an OD_{600} below 0.6. Cells were concentrated by centrifugation at 7,200 x *g* for 3 min and applied to No. 1.5 cover glass under 5 % agarose pads with culture medium, except for microscopy with MTSES, which was performed using the CellASIC ONIX microfluidic platform from EMD Millipore.

For msfGFP-PBP2 tracking, M9-glucose-CAA medium was used with 25 μM IPTG. For sfGFP-RodA tracking, M9-maltose-CAA medium was used with 80 μM IPTG. For msfGFP-PBP1b imaging, M9-glucose-CAA medium was used with a beginning concentration of 20 μM IPTG, diluted to 13 μM final IPTG before expansion at 37 °C. For MreB-^{SW}Neon tracking with MTSES treated cells, M9-glucose-CAA medium was used with 100 μM.

For MreB-^{SW}Neon tracking following RodA(WT) or RodA(D262N) overproduction, M9-maltose-CAA medium was used with the addition of 0.8 ng/μL anhydrotetracycline before growth at 37 °C. For experiments following the effect of RodA variant production after 210 min induction, cells were first grown in liquid culture for 120 min under inducing conditions (1mM IPTG) before concentration and imaging. IPTG (1 mM) was included in the agarose pads used for imaging.

Microscopy of *B. subtilis* cells

Overnight cultures grown in CH medium were diluted in fresh medium and grown for at least 3 hours at 37 °C to an OD_{600} below 0.3. Cells were concentrated by centrifugation at 6000 x *g* for 30 seconds and applied to No. 1.5 cover glass under 2 % agarose pads with CH medium. For PBP1 imaging, no inducer was added to the cultures; leaky expression of mNeonGreen-PBP1 was sufficient for particle tracking experiments. All cells were imaged at 37 °C under an agar pad with the top surface exposed to air.

For measurements of growth rate, overnight cultures grown in LB medium were diluted in fresh medium and grown for at least 3 hours at 37 °C and to an OD_{600} below 0.3. The culture was diluted to an OD_{600} of 0.07, and its growth curve was measured in a Growth Curves USA Bioscreen-C Automated Growth Curve Analysis System.

For measurements of cell widths, overnight cultures grown in CH medium were diluted in fresh medium (with addition of 10 μM IPTG where indicated) for at least 3 hours at 37 °C and to an OD_{600} below 0.3. Cells were stained with FM 5-95 (ThermoFisher Scientific) and imaged under agarose pads as described above.

Particle Tracking Microscopy

Total internal reflection fluorescence microscopy (TIRF-M) and phase contrast microscopy were performed using a Nikon Eclipse Ti equipped with a Nikon Plan Apo λ 100X 1.45 objective and a Hamamatsu ORCA-Flash4.0 V2 (C11440-22CU) sCMOS camera. Except where specified, fluorescence time-lapse images were collected by continuous acquisition with 1,000 ms exposures. Microscopy was performed in a chamber heated to 37 °C.

Widefield Epifluorescence Microscopy

Widefield epifluorescence microscopy was performed on the instrument described above, and for some samples, on a DeltaVision Elite Microscope equipped with an Olympus 60x Plan Apo 60x 1.42 NA objective and a PCO.edge sCMOS camera. Cell contours and dimensions were calculated using the Morphometrics software package {Ursell:vg}.

Particle tracking

Particle tracking was performed using the software package FIJI (Schindelin et al. 2012; Schneider et al. 2012) and the TrackMate plugin. For calculation of particle velocity, the scaling exponent α, and track orientations relative to the midline of the cell, only tracks persisting for 7 frames or longer were used. Particle velocity for each track was calculated from nonlinear least

squares fitting using the equation $MSD(t) = 4Dt + (vt)^2$, where MSD is mean squared displacement, t is time interval, D is the diffusion coefficient, and v is speed. The maximum time interval used was 80 % of the track length. Tracks were excluded from further evaluation if the contribution of directional motion to the MSD was less than 0.01 nm/s. Tracks were also excluded if R^2 for log MSD versus log t was less than 0.9, indicating a poor ability to fit the MSD curve. For PBP2, R^2 and speed filtering together resulted in the exclusion of ~50 % of detected tracks. Track overlays in figures include all tracks 7 frames or longer to illustrate the performance of the track detection algorithms.

Track angles relative to the cell axis were taken to be the direction of the line produced by orthogonal least squares regression using all of the points in each track; cell axis angles were determined by finding cell outlines and axes using the Morphometrics software package (Ursell et al. 2014).

Analysis of PBP1 diffusion.

Tracking of *B. subtilis* mNeon-PBP1 in strains MK210 and MK287 was performed using the u-track 2.0 software package (Jaqaman et al. 2008). Resulting trajectories were then manually filtered to minimize particle detection and linking errors. The frame-to-frame vector displacements along these trajectories were then calculated. The magnitude of each of the displacements was taken, and the cumulative distribution function (CDF) of the pool of displacements across all movies in a condition was calculated. The CDF of the displacement magnitudes was then fit to an analytical function describing a diffusion process whereby one or more unique states of diffusion were occurring. The analytical form of the two-state model used in the results is:

$$P(r, \Delta t) = 1 - we^{-\left(\frac{r^2}{4D_1 \Delta t}\right)} - (1 - w)e^{-\left(\frac{r^2}{4D_2 \Delta t}\right)}$$

where P(r, Δt) is the cumulative probability of a displacement of magnitude *r* given the observation period Δt, diffusion coefficients D_1, D_2, and the relative fractions between those two states *w*. For a simpler, one-state model, *w* = 1.

The fitting was performed in MATLAB using a nonlinear least-squares algorithm with 500 restarts to the initial parameters so as to find a close approximation to the true parameters of the model. Residuals of the model fit were calculated and used in the determination of the number of distinct diffusive species present within the dataset.

***B. subtilis* strain construction**

For MK005 [Δ*ponA*] construction, the homology region upstream of *ponA* was amplified from Py79 DNA using oligos oMK001 and oMK002. The *cat* cassette was amplified from pGL79 using oligos oJM28 and oJM29. The homology region downstream of *ponA* was amplified from Py79 DNA using oligos oMK006 and oMK013. The three fragments were fused using isothermal assembly (Gibson et al. 2009) and transformed into Py79 to give MK005 by selecting on chloramphenicol agar.

For MK095, a native functional fusion of mNeonGreen to PBP1 was constructed by isothermal assembly (Gibson et al. 2009) and was recombined into the chromosome of Py79 using counterselection to produce a marker-less strain without any remaining scars. The homology region upstream of *ponA*, fused to the first 30 bases of the coding sequence of mNeonGreen, was amplified from Py79 DNA using oMK001 and oMK027. The *cat* cassette, the P_{xyl} promoter sequence, and the *mazF* coding sequence were amplified as a fused fragment from template DNA using primers oMK047 and oMK086. The coding sequence of mNeonGreen was

amplified from a gBlock using primers oMK078 and oMK087. The downstream homology region encoding a portion of the PBP1 (*ponA*) coding sequence was amplified from Py79 DNA using oMK009 and oMK050. These fragments were fused using isothermal assembly and transformed into Py79 to give MK093 upon selection for chloramphenicol resistance. Since the primers oMK078 and oMK009 contained the sequence for a 15-amino acid flexible linker, the fused product encoded an mNeonGreen-PBP1 fusion protein. The presence of a fragment of the mNeonGreen coding region upstream of *cat* provided a direct repeat to allow for spontaneous removal of the *cat-mazF* sequence by recombination. MK093 was grown in LB medium for 4 hours to allow time for recombination, and 200 µl cells were plated on a LB plate containing 30 mM xylose. This selected for cells in which removed the *cat-mazF*, yielding a scar-less functional fusion protein under the control of the native PBP1 promoter.

Strains MK210 and MK287 encoding an inducible version of the mNeonGreen-PBP1 fusion protein were constructed by isothermal assembly (Gibson et al. 2009). The homology region upstream of *amyE*, the *erm* cassette, and the *LacI*-$P_{hyperspank}$ promoter construct were amplified as a fused fragment from template DNA using primers oMD191 and oMD232. The mNeonGreen-PBP1 coding sequence was amplified from MK095 DNA using primers oMK100 and oMK138. The homology region downstream of *amyE* was amplified from Py79 DNA using oMD196 and oMD197. The fragments were fused using isothermal assembly and transformed into Py79 to give MK210. Genomic DNA from MK005 (Δ*ponA*::cat) was transformed into MK210 to give MK287, a strain in which the mNeonGreen-PBP1 fusion protein was the only copy of PBP1.

Table A.1. Mass spectrometry analysis of MS-PBP1b modification by MTSES.

peptide sequence[1]	mono-isotopic mass	m/z (charge)	peak integration (DMSO)[2]	peak integration (MTSES)[2]	signal intensity ratio (MTSES/DMSO)
HFYEHDGISLYca**C**IGR[3]	1865.8519	933.9332 (+2)	1.03E+09	n.d.[8]	0
HFYEHDGISLYca**C**IGR[3]	1865.8519	622.9579 (+3)	4.76E+09	4.04E+07	0.008
HFYEHDGISLYca**C**IGR[3]	1865.8519	467.4703 (+4)	1.27E+09	n.d.[8]	0
HFYEHDGISLYse**C**IGR[3]	1948.79	975.4026 (+2)	n.d.[8]	1.56E+09	-
HFYEHDGISLYse**C**IGR[3]	1948.79	650.6042 (+3)	n.d.[8]	2.76E+09	-
VWQLPAAVYGR[4]	1258.6822	630.3484 (+2)	1.71E+10	1.71E+10	1.00
LLEATQYR[5]	992.5291	497.2718 (+2)	4.59E+07	4.21E+07	0.919
QFGFFR[6]	800.387	401.2058 (+2)	2.03E+10	1.76E+10	0.866
DSDGVAGWIK[7]	1046.5033	524.2589 (+2)	7.58E+08	7.93E+08	1.05

[1] ca**C** stands for carbamidomethylated cysteine generated by iodoacetamide treatment used to protect Cys-containing peptides during sample preparation. se**C** stands for sulfonatoethyl sulphide-linked cysteine generated by MTSES treatment.
[2] Signals corresponding to the peptides of the indicated m/z were integrated from the extracted ion chromatograms of DMSO-treated and MTSES-treated samples, respectively. The identity of each peak was further confirmed by tandem mass spectra.
[3] Peptide corresponding to PBP1b amino acids 236-250. Contains S247C substitution.
[4] Peptide corresponding to PBP1b amino acids 99-109.
[5] Peptide corresponding to PBP1b amino acids 127-134.
[6] Peptide corresponding to PBP1b amino acids 191-196.
[7] Peptide corresponding to PBP1b amino acids 829-838.
[8] not detected

Table A.2. Bacterial strains used in this study.

Strain	Genotype[a]	Source/Reference[b]
E.coli strains		
MG1655	*rph ilvG rfb*-50	(Guyer et al., 1981)
TB10	*rph1 ilvG rfb-50* lD*cro-bio nad::Tn10*	(Johnson et al, 2004)
TB28	MG1655 D*lacIZYA*::*frt*	(Bernhardt and de Boer, 2004)
MC4100	*F- araD139 Δ(argF-lac)169 rpsL150 relA1 flB5301 deoC1 pstF25 rbsR*	Lab Stock
TU116	MG1655 D*lacIZYA*::*frt* D*ponB::aph*	(Paradis-Bleau et al, 2010)
HC439/pHC817	MG1655 D*pbpA::aph* / P_{lac}::*pbpA*	(Cho et al, 2014)
HC534(attHKCS8)	TB10 D*rodA::aph (*P_{lac}*::rodA*)	This Study
HC516	MG1655 D*lysA*::*frt* D*ampD*::*frt*	This Study
HC518	MG1655 D*lysA*::*frt* D*ponA*::*frt aph*-P_{ara}::*ponB*	This Study
HC523	MG1655 D*lysA*::*frt* D*ponA*::*frt* D*pbpC*::*frt* D*mtgA*::*frt*	This Study
HC526	MG1655 D*lysA*::*frt* D*ponA*::*frt* D*pbpC*::*frt* D*mtgA*::*frt* D*ampD*::*frt*	This Study
HC532	MG1655 D*lysA*::*frt* D*ponA*::*frt* D*pbpC*::*frt* D*mtgA*::*frt ponB(S247C)*	This Study
HC533	MG1655 D*lysA*::*frt* D*ponA*::*frt* D*pbpC*::*frt* D*mtgA*::*frt ponB(S247C)* D*ampD*::*frt*	This Study
HC545	MG1655 D*ponA*::*frt* D*pbpC*::*frt* D*mtgA*::*frt*	This Study
HC546	MG1655 D*ponA*::*frt* D*pbpC*::*frt* D*mtgA*::*frt ponB(S247C)*	This Study
CH138/pCX16	TB28 D*galK* [lc1857 (*cro-bioA*)::TetAR] *mreB*::P_{EM7}-*galK* D*yhdE::cat* / P_{aadA}::*sdiA*	gift from de Boer lab
HC582	HC546 *mreB'-mCherry-'mreB* D*yhdE::cat*	This Study
HC583	HC546 *mreB'-mNeonGreen-'mreB* D*yhdE::cat*	This Study
JAB027	MC4100 *imp4213 bamA6*	This Study

Table A.2. (continued) Bacterial strains used in this study.

Strain	Genotype[a]	Source/Reference[b]
HC590	MG1655 D*lysA*::*frt* D*ponA*::*frt* D*pbpC*::*frt* D*mtgA*::*frt imp4213*	P1(JAB027) X HC523-*leu::Tn10*
HC591	MG1655 D*lysA*::*frt* D*ponA*::*frt* D*pbpC*::*frt* D*mtgA*::*frt ponB(S247C) imp4213*	P1(JAB027) X HC532-*leu::Tn10*
HC595(attHKHC933)	TB28 D*rodA::aph* (P_{lac}::*sfgfp-rodA*)	P1(HC534) X TB28(attHKHC933)
HC596(attHKHC943)	HC545 D*pbpA::aph* (P_{lac}::*msfgfp-pbpA*)	P1(HC439) X HC545(attHKHC943)
HC576(attHKHC942)	HC545 D*ponB::aph* (P_{lac}::*msfgfp-ponB*)	P1(TU116) X HC545(attHKHC942)
HC576(attHKHC949)	HC545 ΔponB::aph (P_{lac}::Halo-ponB)	P1(TU116) X HC545(attHKHC949)
PR71(attHKPR104)	HC545 D*ponB::aph* (P_{lac}::*msfgfp-ponA*)	P1(TU116) X HC545(attHKPR104)
PR70	MG1655 D*lysA*::*frt* D*pbpC*::*frt* D*mtgA*::*frt* D*ampD*::*frt* D*ponB::aph*	This Study
HC527	MG1655 D*lysA*::*frt* D*pbpC*::*frt* D*mtgA*::*frt* D*ampD*::*frt*	This Study
B. subtilis strains		
PY79	WT	Garner lab stock
MK005	PY79 *ΔponA*	This Study
MK095	PY79 *ponA::mNeonGreen-ponA*	This Study
MK210	PY79 *amyE*::$P_{hyperspank}$-*mNeonGreen-ponA*	This Study
MK287	PY79 *ΔponA*, *amyE*::$P_{hyperspank}$-*mNeonGreen-ponA*	This Study

[a] The *aph* and *cat* cassette are flanked by *frt* sites for removal by FLP recombinase. An *frt* scar remains following removal of the cassette using FLP expressed from pCP20.

[b] Strain constructions by P1 transduction are described using the shorthand: P1(donor) x recipient.

Table A.3. Plasmids used in this study.

Plasmid	Genotype[a]	ori	Source/Reference
pKD13	*bla, aph* cassette flanked by *frt* sequence for recombineering	R6K	(Datsenko and Wanner, 2000)
pCP20	*cat bla cI857* P_R::*FLP*	pSC101(*ts*)	(Datsenko and Wanner, 2000)
pHC739	attλ *cat lacI*^{q} P_{tac}::*sulA*	R6K	(Cho et al, 2014)
pCX16	*aadA sdiA*	pSC101	(Bendezu and de Boer, 2008)
pCS8	*attHK022 bla lacI*^{q} P_{lac}::*rodA*	R6K	(Sham et al, 2014)
pMM15	*attHK022 bla lacI*^{q} P_{lac}::*ponB*	R6K	This Study
pHC872	*attHK022 cat lacI*^{q} P_{lac}::*ponB*	R6K	This Study
pHC873	*attHK022 cat lacI*^{q} P_{lac}::*ponB(S247C)*	R6K	This Study
pHC878	*cat ponB(S247C)*	pSC101(*ts*)	This Study
pFB262	*bla lacI*^{q} P_{lac}::*mreB'-mCherry-'mreB*	ColE1	(Bendezu et al, 2009)
pHC892	*bla lacI*^{q} P_{lac}::*mreB'-mNeonGreen-'mreB*	ColE1	This Study
pHC897	*attλ cat lacI*^{q} P_{lac}::*mreB'-mNeonGreen-'mreB*	R6K	This Study
pHC929	*attHK022 bla lacI*^{q} P_{tetA}::*mreB'-mNeonGreen-'mreB*	R6K	This Study
pHC817	*cat* P_{lac}::*pbpA*	ColE1	(Cho et al, 2014)
pHC857	*cat* P_{lac}::*pbpA-rodA*	ColE1	(Cho et al, 2014)
pHC938	*cat* P_{lac}::*pbpA-rodA(D262N)*	ColE1	This Study
pHC933	*attHK022 tetAR lacI*^{q} P_{lac}::*sfgfp-rodA*	R6K	This Study
pHC942	*attHK022 tetAR lacI*^{q} P_{lac}::*msfgfp-ponB*	R6K	This Study
pHC943	*attHK022 tetAR lacI*^{q} P_{lac}::*msfgfp-pbpA*	R6K	This Study
pDHL940	pUC19-HaloTag H7-FRT-Kan^R-FRT	pUC	(Ke et al., 2016)
pHC949	*attHK022 tetAR lacI*^{q} P_{lac}::*Halo-ponB*	R6K	This Study

Table A.4. *B. subtilis* primer list

primer name	sequence (5'-3')
oMD191	TTTGGATGGATTCAGCCCGATTG
oMK138	TCTTTCGGTAAGTCCCGTCTAGCCTTGCCCTCACCCCAAAGGTGACGGCTTTTTTGT
oMK100	ATAACAATTAAGCTTTAAGGAGGAACTACCATGGTTTCGAAAGGAGAGGAGG
oMK087	AAAATTAACGTACTGATTGGGTAGTCTAGAATGGTTTCGAAAGGAGAGGAGGATAATATG
oMK086	ATGGTTTCGAAAGGAGAGGAGGATAATATGCAGGGAGCACTGGTCAACTACCG
oMK078	TGGCCTGAGCCCGGTCCCTGGCCAGATCCCTCGAGCTTATAGAGTTCATCCATACCCATC
oMK050	GAGTCATCAATTTGTTCGTATGTGGACC
oMK047	TCTAGACTACCCAATCAGTACGTT
oMK027	AACATCTCAACCTTTCGTTAATCAACC
oMK013	GTAGTTGACCAGTGCTCCCTGTAAAACACAAACAAACTCATCATC
oMK009	CTGGCCAGGGACCGGGCTCAGGCCAAGGAAGCGGCATGTCAGATCAATTTAACAGCCGTG
oMK006	CGTGTACAAGCAAAGCAGAATGAAC
oMK002	CTGAGCGAGGGAGCAGAACATCTCAACCTTTCGTTAATCAACC
oMK001	GCCTTATCCTTTCCTCCGCC
oMD232	ggtagttcctccttaAAGCTTAATTGTTATCCGCTCACAAT
oMD197	TCACATACTCGTTTCCAAACGGATC
oMD196	GGGCAAGGCTAGACGGG
oJM29	CAGGGAGCACTGGTCAAC
oJM28	TTCTGCTCCCTCGCTCAG

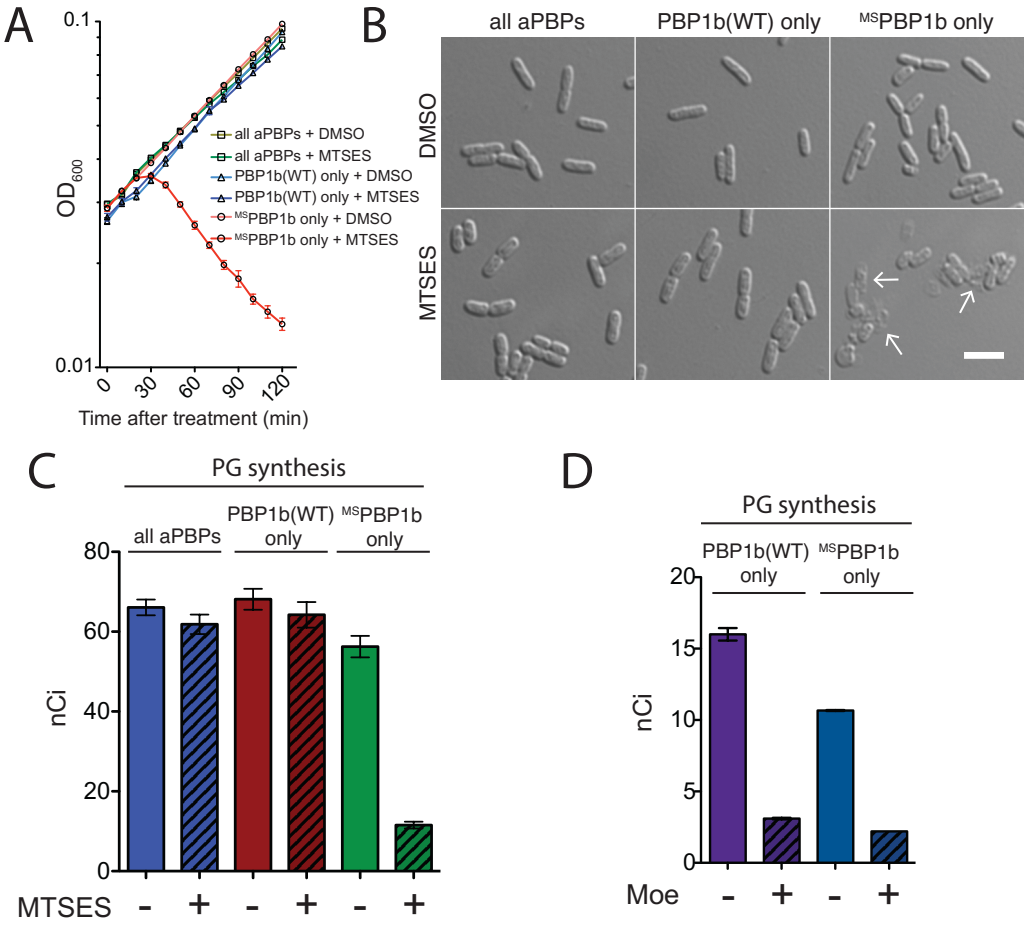

A
0.1
0.01
OD600
0
30
60
90
120
Time after treatment (min)
all aPBPs + DMSO
all aPBPs + MTSES
PBP1b(WT) only + DMSO
PBP1b(WT) only + MTSES
MSPBP1b only + DMSO
MSPBP1b only + MTSES
B
all aPBPs
PBP1b(WT) only
MSPBP1b only
DMSO
MTSES
C
PG synthesis
all aPBPs
PBP1b(WT) only
MSPBP1b only
nCi
80
60
40
20
0
MTSES - + - + - +
D
PG synthesis
PBP1b(WT) only
MSPBP1b only
nCi
20
15
10
5
0
Moe - + - +

Figure A.1.

Figure A.1 (continued). Functionality of ^{MS}PBP1b and specificity of inhibition with MTSES.
A. MTSES-sensitive growth is only observed for cells containing ^{MS}PBP1b as their sole aPBP. Cells of MG1655 [WT] (labeled all aPBPs), HC545 [Δ*ponA* Δ*pbpC* Δ*mtgA ponB(WT)*] (labeled PBP1b(WT) only), and HC546 [Δ*ponA* Δ*pbpC* Δ*mtgA* ^{MS}*ponB*] (labeled ^{MS}PBP1b only) were grown overnight in M9-glucose supplemented with 0.2% casamino acids at 37°C. The resulting cultures were diluted 1:100 in the same medium and grown at 37°C to exponential phase. The OD_{600} of each culture was adjusted to 0.1 with fresh medium and DMSO (control) or MTSES (1mM) were added as indicated. A small volume of each culture (150 µl) was then transferred to Corning 96-well plates (ref. 3598) and OD_{600} was monitored during growth with shaking at 37°C in a VersaMax microplate reader (Molecular Devices). Note, OD_{600} values from the plate reader are lower than those measured from cultures due to a difference in path length.
B. Effect of MTSES on cell morphology. Cells prepared from cultures grown similarly to those in (A) were harvested and fixed 45 min after treatment with DMSO (control) or MTSES (1mM). Fixed cells were then imaged on agarose pads using DIC optics. Scale bar equals 4 microns. Arrows point to lysed cells. **C. Specificity of PG synthesis inhibition by MTSES.** Overnight cultures of HC516 [Δ*lysA* Δ*ampD*] (labeled all aPBPs), HC526 [Δ*lysA* Δ*ampD* Δ*ponA* Δ*pbpC* Δ*mtgA ponB*(WT)] (labeled PBP1b(WT) only), and HC533 [Δ*lysA* Δ*ampD* Δ*ponA* Δ*pbpC* Δ*mtgA* ^{MS}*ponB*] (labeled ^{MS}PBP1b only) all harboring an integrated P_{tac}::*sulA* construct (attλC739) were diluted to OD_{600} = 0.04 in fresh M9-glycerol medium supplemented with 0.2% casamino acids. Cultures were then grown at 30°C to OD_{600} between 0.27-0.30, at which time IPTG (1 mM) was added to induce *sulA* expression. After 30 minutes of additional growth and an adjustment of each culture to an OD_{600} of 0.3, MTSES (1 mM) or an equivalent amount of DMSO was added. Following 5 additional minutes of growth, 0.5 ml of each culture was incubated with 1 µCi [^{3}H]-mDAP for 10 min at 30°C before mDAP incorporation was stopped by boiling the samples for 30 min at 90°C. The boiled samples were pelleted, washed, and digested with 250 µg HEW lysozyme overnight at 37°C. The radioactivity released by lysozyme treatment was quantified by scintillation counting. **D. PG synthesis is inhibited by moenomycin to a similar degree as MTSES-treatment of ^{MS}PBP1b-containing cells.** Cells of HC590 [*imp*4213 Δ*lysA* Δ*ponA* Δ*pbpC* Δ*mtgA ponB*(WT)] (labeled PBP1b(WT) only), and HC591 [*imp*4213 Δ*lysA* Δ*ponA* Δ*pbpC* Δ*mtgA* ^{MS}*ponB*] (labeled ^{MS}PBP1b only) harboring an integrated P_{tac}::*sulA* construct (attλC739) were grown and labeled with [^{3}H]-mDAP as above. However, in place of MTSES, cells were treated with 10 µg/mL moenomycin (Moe). Note that the strains used here are outer membrane compromised (*imp*4213) derivatives of the strains in (C) to allow for moenomycin entry.

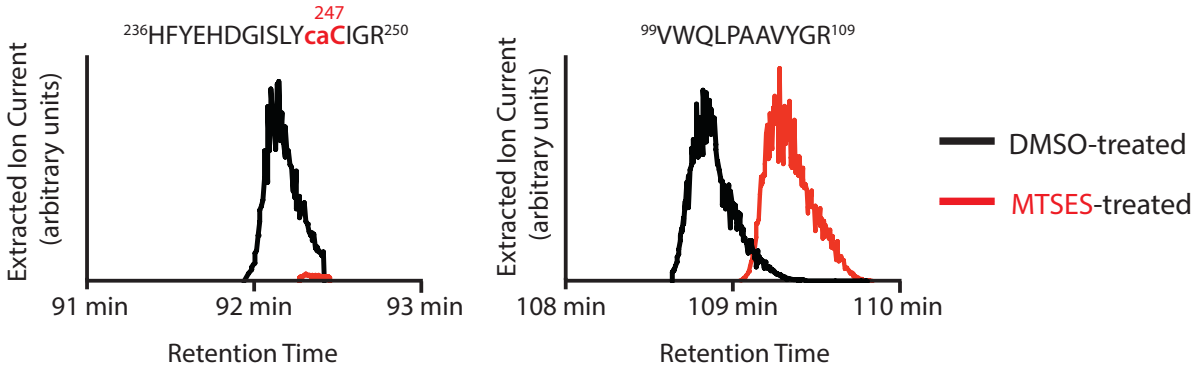
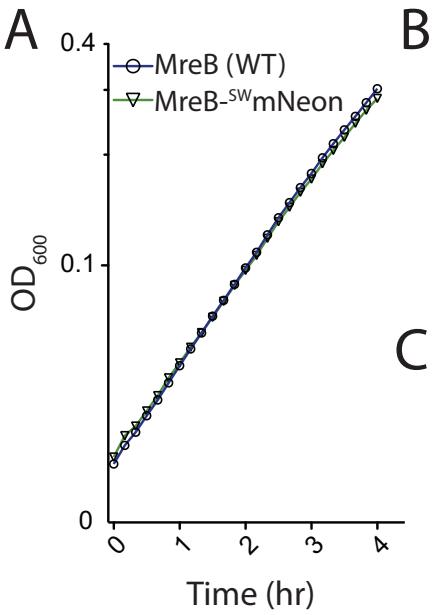
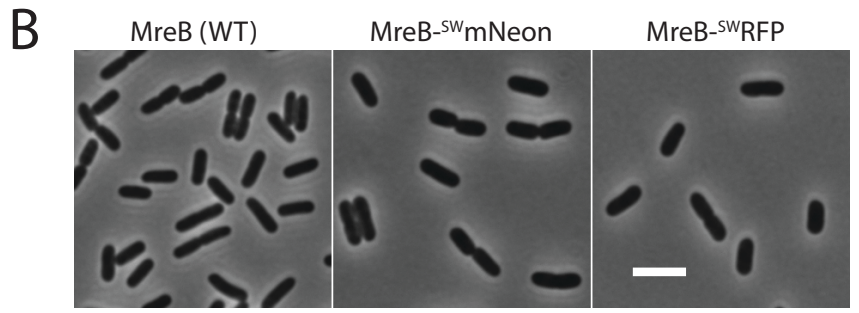


Figure A.2. Mass Spectrometry analysis of ^{MS}PBP1b modification by MTSES. Shown are extracted ion current (EIC) chromatograms for the indicated tryptic peptides of ^{MS}PBP1b prepared from cells with or without MTSES treatment. The Cys247-containing peptide was only detected in the mock (DMSO) treated sample, indicating virtually complete modification by MTSES. However, equivalent levels of the peptide from residue 99-109 were detected regardless of treatment. Note, **caC** indicates carbamidomethylated cysteine generated by iodoacetamide treatment used to protect Cys-containing peptides during sample preparation. Also see Table A.1.





C

mreB allele	length (mean ± std)	width (mean ± std)	measured cell number
mreB(WT)	2.91 ± 0.67 µm	0.89 ± 0.05 µm	327
mreB-SWmNeon	2.90 ± 0.61 µm	1.05 ± 0.05 µm	187
mreB-SWRFP	2.71 ± 0.53 µm	1.03 ± 0.07 µm	154

Figure A.3. Functionality of the MreB-SWmNeon fusion.
A. Growth of MreB-SWmNeon producing cells is normal. Cells of HC546 [Δ*ponA* Δ*pbpC* Δ*mtgA* MS*ponB*] and its derivative HC583 harboring *mreB-SW mNeon* replacing *mreB* at the native locus, were grown and OD_{600} was monitored as in Figure A.1A.

B-C. Cell morphology is largely normal in MreB-SWmNeon producing cells. Overnight cultures of the strains in (A) as well as HC582, also a derivative of HC546, but with *mreB-SW RFP* at the native *mre* locus, were diluted (1:100) in M9-glucose medium supplemented with 0.2% casamino acids and grown at 37°C to an OD_{600} of 0.3. Cells were then imaged on agarose pads using phase contrast optics. Scale bar, 4 microns. Panel (C) shows length and width measurements of cells imaged as in (B). Measurements were made using Oufti (1).

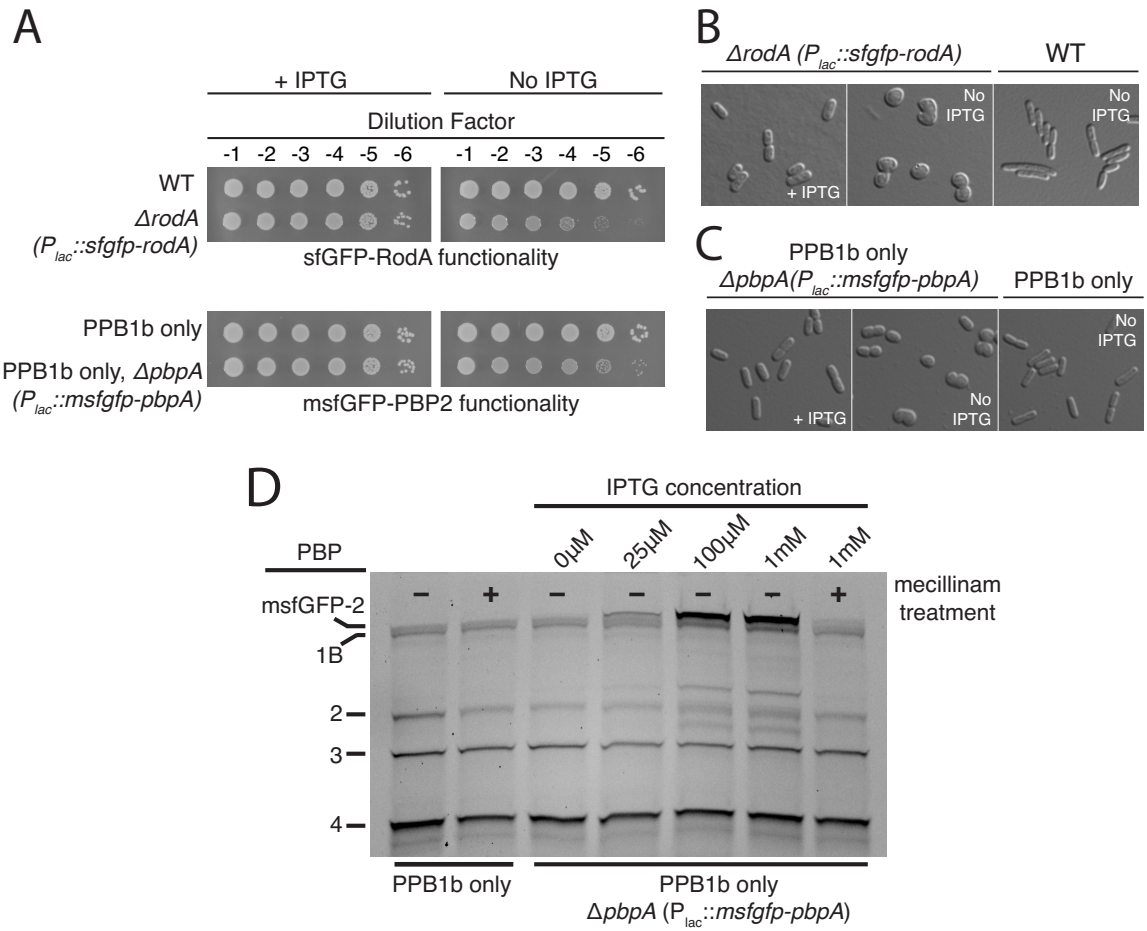


Figure A.4. Functionality of PBP2 and RodA fluorescent protein fusions.
A. RodA or PBP2 fusion production corrects the growth phenotypes of *rodA* or *pbpA* deletion mutants, respectively. Overnight cultures of TB28 [WT], HC595(*att*HKpHC933) [Δ*rodA* (P_{lac}::*sfgfp-rodA*)], HC545 [Δ*ponA* Δ*pbpC* Δ*mtgA*] (labeled PBP1b only) or HC596(*att*HKHC943) [PBP1b only Δ*pbpA* (P_{lac}::*msfgfp-pbpA*)] were serially diluted and spotted on M9 minimal maltose agar for the RodA functionality test or M9 minimal glucose agar for the PBP2 functionality test. Media was additionally supplemented with 0.2% casamino acids as well as IPTG as indicated (100 μM for *sfgfp-rodA* or 25 μM *msfgfp-pbpA).*
B-C. Cell morphology of the fluorescent protein fusion strains grown with or without induction of fluorescent protein fusions. Overnight cultures of the strains in (A) grown in the presence of IPTG were washed with M9 minimal medium, diluted to an OD_{600} of 0.001, and grown to exponential phase in M9 minimal medium with or without IPTG induction. Sugar, casamino acid, and IPTG supplementation were as in (A).
D. Measurement of relative msfGFP-PBP2 concentration by Bocillin binding. Overnight cultures of HC545 [Δ*ponA* Δ*pbpC* Δ*mtgA*] (labeled PBP1b only) or HC596(*att*HKHC943) [PBP1b only Δ*pbpA* (P_{lac}::*msfgfp-pbpA*)] were diluted and grown as in (B-C). Cells harvested from 15 ml of exponential cultures were labeled with Bocillin (see Methods). A subset of cultures were treated with 10 μg/mL mecillinam, which reacts with the TP active site of PBP2 and blocks Bocillin binding, 5 min prior to harvesting and labeling.

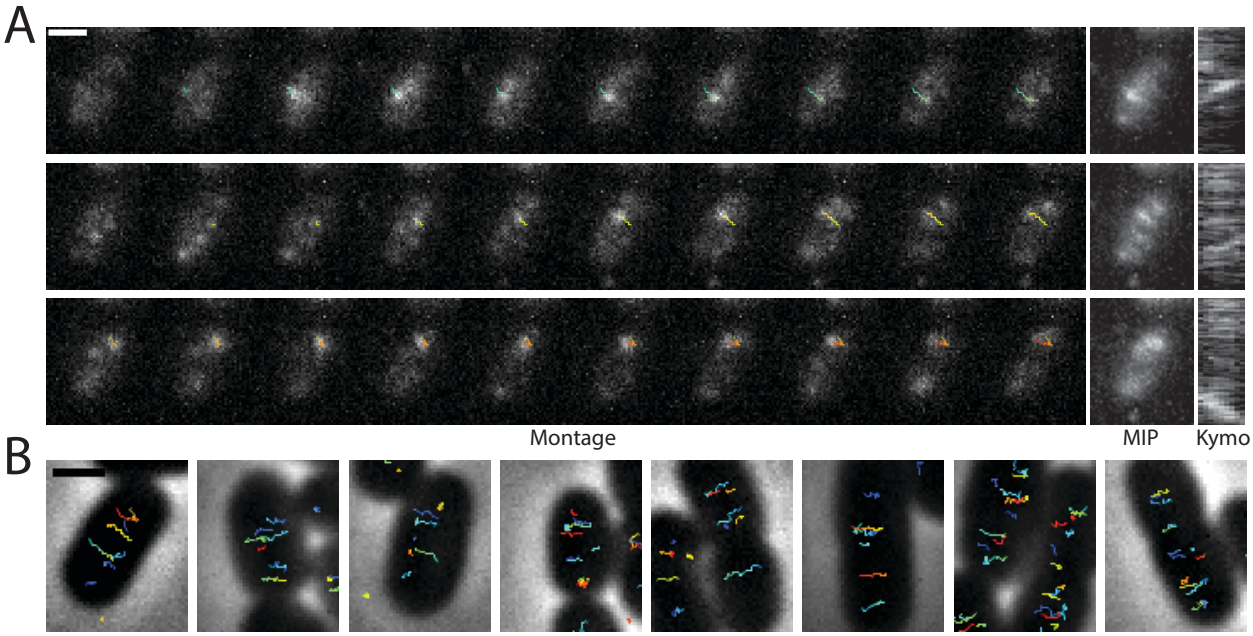


Figure A.5. RodA moves circumferentially around the the cell cylinder. A. Montage of RodA movement in HC595(attHKpHC933) [Δ*rodA* (P_{lac}::*sfgfp-rodA*)] shows directional motion. Maximal intensity projection (MIP) and kymograph (Kymo) frames were collected every 1 s, montage frames every 2 s. Displayed are raw trajectories not filtered for speed or log log fits to α. **B.** Phase contrast images with track overlays show additional examples of RodA directional motion. Scale bars are 1 μm.

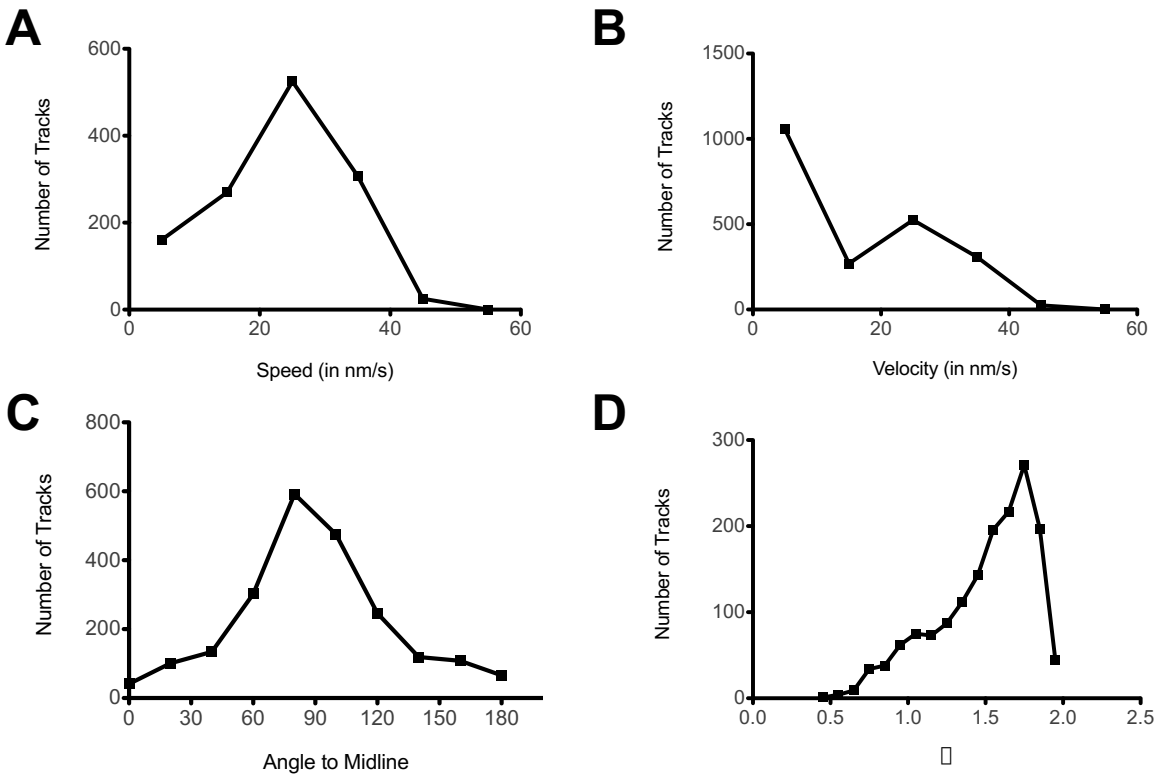


Figure A.6. PBP2 moves circumferentially around the the cell cylinder. A. Histogram of directionally moving particles (velocity > 0.01 nm/s) without filtering by α fit as described in Materials and Methods. **B.** Histogram of all velocities, including non-directional particles (velocity <0.01 nm/s). **C.** Histogram of all angles to the cell midline without filtering on R^2 fits to a line. **D.** Histogram of the scaling exponent α (filtered for linear fits to the log-log of α and velocity >0.01 nm/s as described in Materials and Methods) with a median value of 1.65, indicating directed motion.

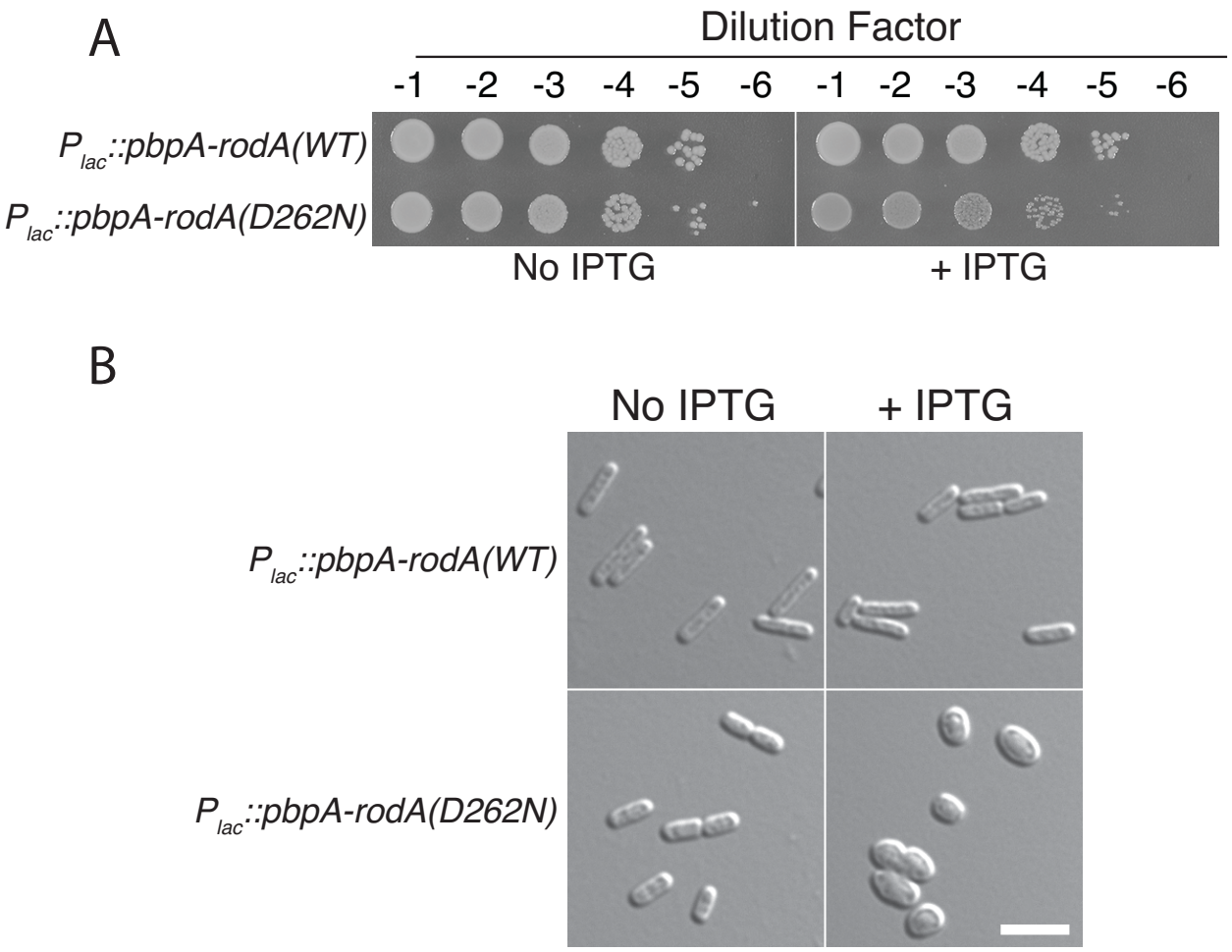


Figure A.7. Dominant-negative activity of RodA(D262N).
A. Overexpression of RodA(D262N) causes a growth defect. Cells of TB28 [WT] harboring both an integrated *P_{tetA}::mreB-^{SW}mNeon* construct (attHKHC929), and either pHC857 [*P_{lac}::pbpA-rodA(WT)*] or pHC938 [*P_{lac}::pbpA-rodA(D262N)*], were grown overnight at 37°C in M9-maltose supplemented with 0.2% casamino acids and 10 µg/mL chloramphenicol. Serial dilutions of these cultures were spotted onto agar plates of the same medium composition, with or without 1 mM IPTG.
B. Effect of RodA(D262N) overexpression on cell morphology. The cultures described in (A) were diluted to an OD_{600} of 0.05 and grown at 37°C until the OD_{600} reached between 0.2 and 0.3. These exponential-phase cultures were then further diluted (to an OD_{600} of 0.005) in the presence or absence of 1 mM IPTG. Cells were fixed when the OD_{600} reached between 0.1 and 0.15, then imaged on agarose pads using DIC optics. Scale bar, 4 microns.

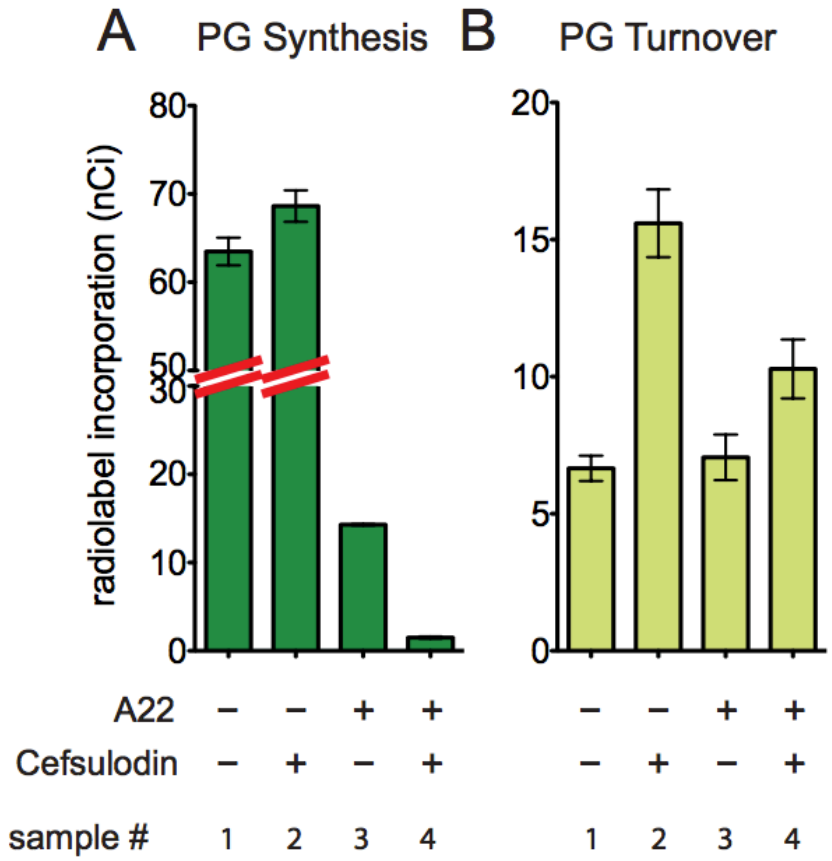


Figure A.8. PBP1a polymerizes PG without a functional cytoskeleton. A-B. PG matrix assembly and turnover were measured upon treatment of strain PR70(attHKHC739) [Δ*lysA* Δ*ampD* Δ*pbpC* Δ*mtgA* Δ*ponB* (P_{tac}::*sulA*)] with cefsulodin and/or A22. Measurements were made as described in Figure 2 and 4. Cefsulodin and A22 were used at 100 μg/ml and 10 μg/mL, respectively. Note that this strain produces PBP1a as its only aPBP. Significant PG synthesis activity is detected upon A22 treatment (sample 3), which inactivates MreB in cells already inactivated for FtsZ by SulA expression. This activity is converted to turnover by the PBP1a-specific beta- lactam cefsulodin (sample 4). We thus conclude that, like PBP1b, PBP1a remains active when all cytoskeletal elements are inactivated in *E. coli*. Results are the average of three independent experiments with the error bars representing the standard error of the mean.

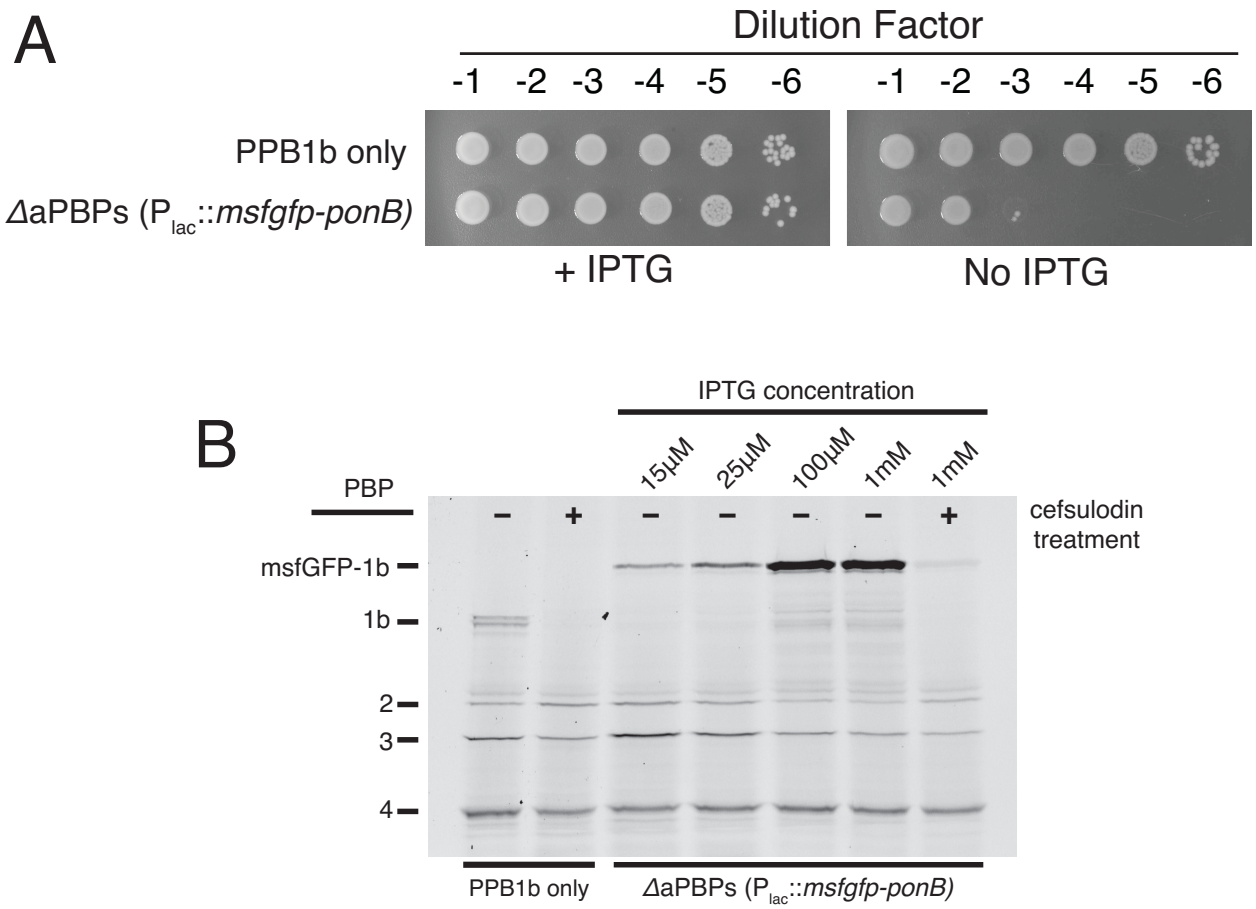
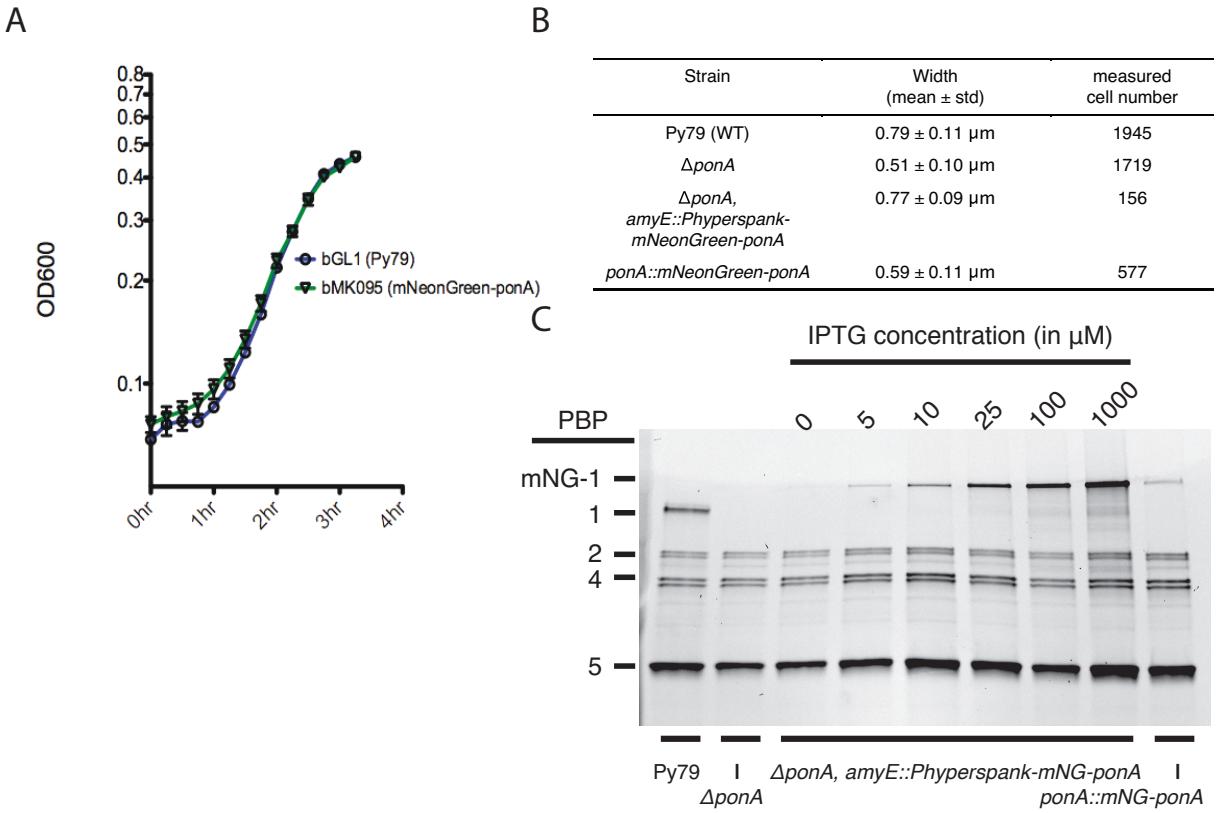


Figure A.9. Functionality of msfGFP-PBP1b.
A. msfGFP-PBP1b supports growth as the sole aPBP. Cultures of HC545 [Δ*ponA* Δ*pbpC* Δ*mtgA*] (labeled PBP1b only) and HC576(attHKHC942)[Δ*ponA* Δ*pbpC* Δ*mtgA* Δ*ponB* (P_{lac}::*msfgfp-ponB*)] (labeled ΔaPBPs) were grown overnight in M9-glucose medium supplemented with 0.2% casamino acids with 25 μM IPTG. Cell were then washed and serially diluted in the same medium lacking IPTG. Aliquots (5 μL) of each dilution were then spotted on M9-glucose agar supplemented with 0.2% casamino acids with or without 25 μM IPTG as indicated. The plates were incubated for 24 hrs at 37°C and imaged.
B. Measurement of relative msfGFP-PBP1b concentration by Bocillin binding. Cultures of the strains in (A) were diluted, grown, and labeled with Bocillin as in **Fig. A.3D**. Indicated cultures were treated with 100 μg/mL cefsulodin for 5 min prior to harvesting and labeling. Note that the doublet band for PBP1b in lane one corresponds to the alpha and gamma forms of PBP1b produced from alternate start codons. The msfGFP-PBP1b fusion is to the shorter gamma form.



Strain	Width (mean ± std)	measured cell number
Py79 (WT)	0.79 ± 0.11 μm	1945
Δ*ponA*	0.51 ± 0.10 μm	1719
Δ*ponA*, *amyE::Phyperspank-mNeonGreen-ponA*	0.77 ± 0.09 μm	156
ponA::mNeonGreen-ponA	0.59 ± 0.11 μm	577

Figure A.10. Functionality of mNeon-PBP1 fusion in *B. subtilis*. A. Growth curves of Py79 [WT] and MK095 [*ponA::mNeonGreen-ponA*] strains. **B.** Cell width measurements of Py79 [WT], MK005 [Δ*ponA*], MK287 [Δ*ponA; amyE::Phyperspank-mNeonGreen-ponA*], and MK095 [*ponA::mNeonGreen- ponA*], strains. For MK287, mNeon-PBP1 was induced by addition of 1mM IPTG. **Measurement of relative mNeon-PBP1 concentration by Bocillin binding. C.** Overnight cultures of strains Py79, MK005, MK287, and MK095 (left to right) were diluted into fresh CH medium, grown for two hours at 37 °C, and labeled with Bocillin as in **Fig. A.3D**. Note that the concentration of mNeon-PBP1 expressed from its native promoter (MK095, rightmost) is less than that in wild-type (Py79, leftmost), explain MK095's incomplete suppression of the width loss that follows *ponA* deletion.

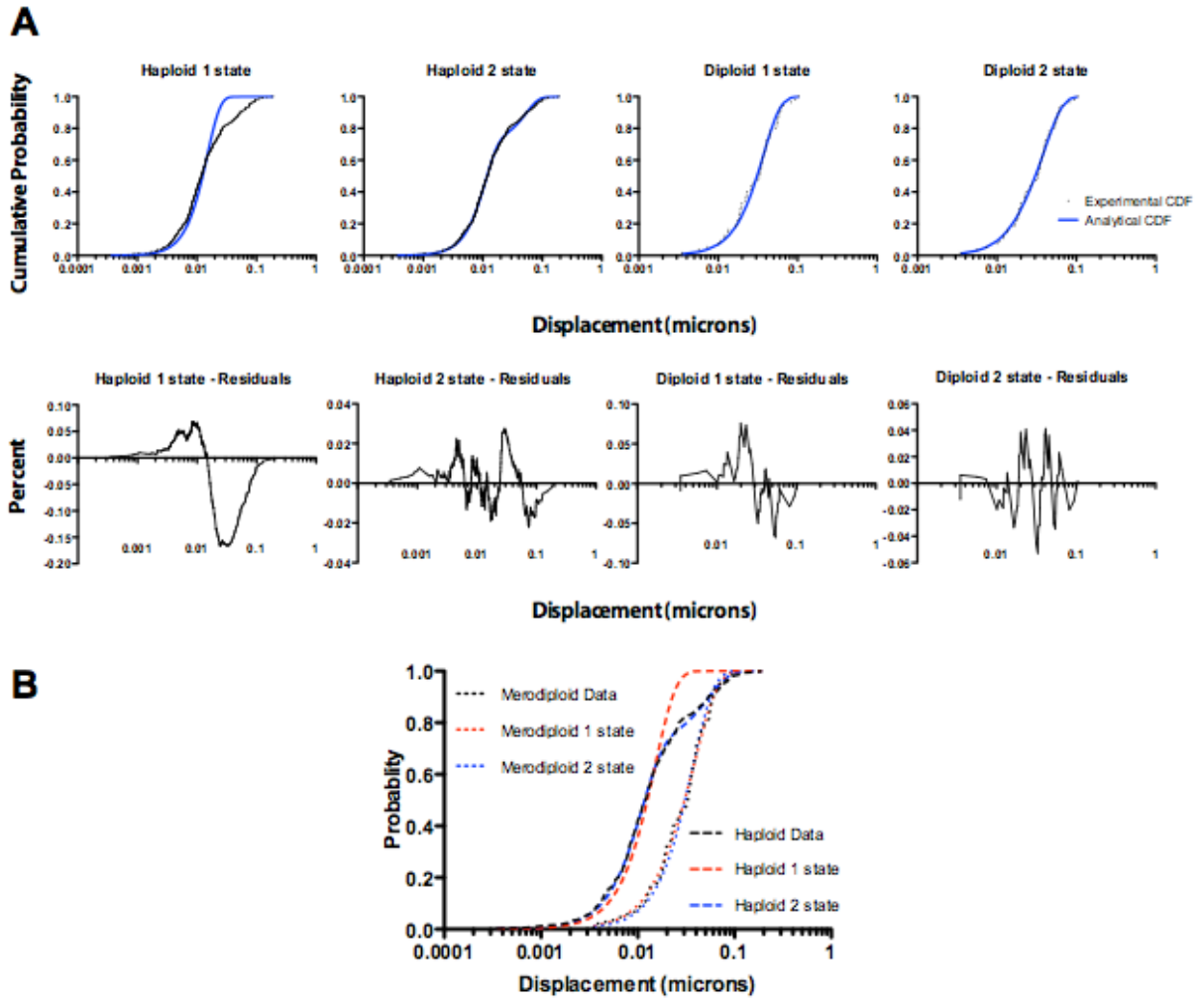


Figure A.11. A. Cumulative distribution function (CDF) fitting of PBP1 displacements reveals two-state diffusive behavior. Top row: the analytical (blue) and experimental (black) CDF curves for haploid (MK287) and merodiploid (MK210) strain datasets. Bottom row: respective residuals for CDF model fits corresponding to the above CDF plots. The single-state haploid fitting has considerable residuals corresponding to the location of where a faster state of diffusion manifests, necessitating the introduction of a second state of diffusion for this enzyme into the CDF fitting. **B.** Comparison of the CDF model fits between merodiploid and haploid strains. The characteristic displacement magnitude of the two-state haploid strain CDF where the residuals hit the maximum value in the one-state model closely corresponds to that of the fast state of the merodiploid strain, suggesting both of these fast states may result from the same underlying biological phenomena.

Supplementary materials for Chapter 4: Control of cell diameter in *Bacillus subtilis*

Acknowledgements

The authors would like to thank Carl Wivagg, Ye Jin Eun, and Thomas Bernhardt for helpful advice and discussions. We thank Yingjie Sun for assistance with growth rate analysis and construction of HaloTag-PBP2A strains. We also thank Luke Lavis for his generous gift of JF dyes.

Supplementary Experimental Procedures

Media, bacterial strains, and culture conditions

For all experiments, cells were grown overnight at room temperature in CH medium (for certain experiments, as indicated below, xylose and/or IPTG was also added). When this pre-culture reached exponential phase the next day, it was further diluted into fresh CH medium with the indicated concentration of xylose and/or IPTG, and grown for at least 3 hours at 37 °C. The bacterial strains used in this study are listed in Table A.5, and a description of their construction is provided below.

Construction of merodiploid *ponA* strains

To create an IPTG-inducible allele of *ponA*, we inserted a copy of the *ponA* gene under the control of the Phyperspank promoter at the non-essential allele *yhdH*. We amplified: the genomic region upstream of *yhdH* from Py79 gDNA template using primers 5'-

CCTGTTTCAGGTTCGGTGTATAC-3' and 5'-ACGAACGGTAGTTGACCAGTGCTCCCTGGCCAAGAACAGAAAAGAGGCGGCCTGTATGGC-3'; the *cat* resistance cassette, fused to *lacI*, and the Phyperspank promoter from a previously existing template using primers 5'-CAGGGAGCACTGGTCAAC-3' and 5'-GGTAGTTCCTCCTTAAAGCTTAATTGTTATCCGCTCACAAT-3'; the *ponA* coding region from Py79 gDNA template using primers 5'-ATAACAATTAAGCTTTAAGGAGGAACTACCATGTCAGATCAATTTAACAGCCGTG-3' and 5'-GAAAAGAGGCGGCCTGTATGGCCGTTAATTTGTTTTTTCAATGGATGATGAGTTTGTTTG-3'; the genomic region downstream of *yhdH* from Py79 gDNA template using primers 5'-CGGCCATACAGGCCG-3' and 5'-GCTGACGGTAAAATCGGCAATATC-3'.

These fragments were combined by isothermal assembly (Gibson et al. 2009) and used to transform the strain bGL12. Colonies were selected by screening for acquisition of chloramphenicol resistance and loss of spectinomycin resistance. A preparation of gDNA from the resultant strain was used to back-cross into Py79, to create the final strain bMD554. A similar procedure was used to create strain bMD594, with *ponA* fused to the Pspank promoter instead.

Generation of haploid inducible *ponA* strains

To generate a strain in which the Pspank-*ponA* allele was the sole source of PBP1, bMD594 gDNA was prepared and used to transform a null mutant strain (*ponA::kan*), producing strain bMD598.

Construction of a merodiploid *mreBCD* strain

To create an xylose-inducible allele of *mreBCD*, we inserted a copy of the *mreBCD* operon under the control of the Pxyl promoter at the non-essential allele *amyE*. We amplified: the genomic region upstream of *amyE* fused to the *erm* resistance cassette, *xylR*, and the Pxyl promoter, from a previously existing template using primers 5'-TTTGGATGGATTCAGCCCGATTG-3' and 5'-GGTAGTTCCTCCTTAATCGATCCATTCAAATACAGATGCATTTTATTTC-3'; the *mreBCD* coding region from Py79 gDNA template using primers 5'-TTTGAATGGATCGATTAAGGAGGAACTACCATGTTTGGAATTGGTGCTAGAGAC-3' and 5'-TTCTTTCGGTAAGTCCCGTCTAGCCTTGCCCTTACTCATCTCTCAATTCTTTCTTTAGAC-3'; the genomic region downstream of *amyE* from Py79 gDNA template using primers 5'-GGGCAAGGCTAGACGGG-3' and 5'-TCACATACTCGTTTCCAAACGGATC-3'.

These fragments were combined by isothermal assembly (Gibson et al. 2009) and used to transform Py79. Colonies were selected by screening for acquisition of erythromycin resistance to give strain bMK355.

Construction of an in-frame deletion of *mreBCD*

To generate a strain in which the previously described Pxyl-*mreBCD* allele was the sole source of MreB, MreC, and MreD in the genome, we wished to delete the endogenous alleles. However, because these genes are part of the larger *mreB-mreC-mreD-minC-minD* polygenic operon, we had to create an in-frame deletion that would not affect the downstream *minCD* genes. Moreover, because *mreB-mreC-mreD* are all essential genes, the deletion would have to be made in the bMK355 background, with Pxyl-*mreBCD* present as a second source.

First, a clean deletion of *mreB-mreC-mreD-minC-minD* was made; we amplified the region upstream of *mreB* using primers 5'-TTTCACCAGAAGAAAACGTCCAATG-3' and 5'-ATACGAACGGTAGTTGACCAGTGCTCCCTGATGTATGTATCTTCCTTTCTTAAAGC-3'; the *cat* resistance cassette using primers 5-'CAGGGAGCACTGGTCAAC-3' and 5'-TTCTGCTCCCTCGCTCAG-3'; the region downstream of *minD* using primers 5'-ATACGAACGGTACTGAGCGAGGGAGCAGAATGTGATAGAATCAAAGAGAAGAATCTGAC-3' and 5'-ACGCTTGATTCTCCAAGAAAAAAACAC-3'. These fragments were combined by isothermal assembly (Gibson et al. 2009) and used to transform bMK355 in the presence of 30mM xylose. Colonies were selected by screening for acquisition of chloramphenicol resistance to give strain bMD543.

Next, we reintroduced the *minC-minD* alleles to their native chromosomal loci in this strain. We amplified: the region upstream of *mreB*; the *spec* resistance cassette using primers 5-'CAGGGAGCACTGGTCAAC-3' and 5'-TGTTACATATTGCTGCTTTTTGGTCTTCACATGTATGTATCTTCCTTTCTTAAAGC-3'; the *minC-minD* genes using primers 5'-GTGAAGACCAAAAAGCAGCAATATG-3' and 5'-ATACGAACGGTACTGAGCGAGGGAGCAGAAAAAAACAAAAAAAACCTGACACAGCATATG-3'; the region downstream of *minD* using primers 5'-ATACGAACGGTAGTTGACCAGTGCTCCCTGTGTGATAGAATCAAAGAGAAGAATCTGAC-3' and 5'-ACGCTTGATTCTCCAAGAAAAAAACAC-3'. These fragments were combined by isothermal assembly (Gibson et al. 2009) and used to transform bMD543 in the presence of 30mM xylose. Colonies were selected by screening for acquisition of spectinomycin resistance to give strain bMD545.

Combination of inducible *ponA* and *mreBCD* alleles

The strain bMD620, which contained Pspank-*ponA* and Pxyl-*mreBCD* as the sole sources of PBP1, MreB, MreC, and MreD, was created via a series of intermediates. First, the haploid *mreBCD* strain bMD545 was transformed with bMD594 gDNA to create bMD619. *ponA* was then knocked out in bMD619 by transforming with bMD208 gDNA and selecting for kanamycin resistance. This produced bMD620.

The strain bMD622, which contained Pspank-*ponA* as the sole source of PBP1, but contained Pxyl-*mreBCD* in addition to the endogenous copy of *mreBCD* was created by transforming bMD598 with gDNA prepared from bMK355 and selecting for erythromycin resistance.

Construction of merodiploid *rodA* strain

To create an IPTG-inducible allele of *rodA*, we inserted a copy of the *rodA* gene under the control of the Phyperspank promoter at the non-essential allele *yhdH*. We amplified: the genomic region upstream of *yhdH* from Py79 gDNA template using primers 5'-CCTGTTTCAGGTTCGGTGTATAC-3' and 5'-ACGAACGGTAGTTGACCAGTGCTCCCTGGCCAAGAACAGAAAAGAGGCGGCCTGTATGGC-3'; the *cat* resistance cassette, fused to *lacI*, and the Phyperspank promoter from a previously existing template using primers 5'-CAGGGAGCACTGGTCAAC-3' and 5'-GGTAGTTCCTCCTTAAAGCTTAATTGTTATCCGCTCACAAT-3'; the *rodA* coding region from Py79 gDNA template using primers 5'-ATAACAATTAAGCTTTAAGGAGGAACTACCATGAGTCGATATAAGAAACAGCAAAGC-3' and 5'-

GAAAAGAGGCGGCCTGTATGGCCGTCAAGAATTAAAAAGATAACTTCTGTATTTCGT CAG-3'; the genomic region downstream of *yhdH* from Py79 gDNA template using primers 5'-CGGCCATACAGGCCG-3' and 5'-GCTGACGGTAAAATCGGCAATATC-3'.

These fragments were combined by isothermal assembly (Gibson et al. 2009) and used to transform Py79. Colonies were selected by screening for chloramphenicol resistance to create the strain bMD556.

Generation of haploid inducible *rodA* strains

To generate bMD580, in which the Phyperspank-*rodA* allele was the sole source of RodA, we knocked out the native allele of *rodA* in bMD556. To do this, we performed isothermal assembly of the following fragments: region downstream of *rodA* amplified using 5'-TGTTGTATGGATTTTCATCTTTACAGGTG-3' and 5-'ATACGAACGGTAGTTGACCAGTGCTCCCTGTCTATCCCGCCTTACATTTTCATCG-3'; *kan* resistance cassette amplified using 5'-CAGGGAGCACTGGTCAAC-3' and 5'-TTCTGCTCCCTCGCTCAG-3'; upstream region of *rodA* using 5'-ATACGAACGGTACTGAGCGAGGGAGCAGAATATGCAGACAGCCTTTACAGAGG-3' and 5'-GTTTTCGCTGCTATATGACTGATTAGC-3'; the assembled fragment was used to transform bMD556 and colonies were screened for kanamycin resistance.

To generate bMD592, in which the endogenous promoter of *rodA* was replaced with Pxyl, we amplified: region downstream of *rodA* amplified using 5'-TGTTGTATGGATTTTCATCTTTACAGGTG-3' and 5-'ATACGAACGGTAGTTGACCAGTGCTCCCTGTCTATCCCGCCTTACATTTTCATCG-3'; the *erm* resistance cassette fused to *xylR* fused to the Pxyl promoter amplified from a prexisting template using 5'-CAGGGAGCACTGGTCAAC-3' and 5'-

GGTAGTTCCTCCTTAATCGATCCATTCAAATACAGATGCATTTTATTTC-3'; region upstream of *rodA* using 5'-TTTGAATGGATCGATTAAGGAGGAACTACCATGAGTCGATATAAGAAACAGCAAAGC-3' and 5'-TGCACAAAAAAAGACAGCCTCTG-3'. These fragments were combined by isothermal assembly (Gibson et al. 2009) and used to transform Py79, selecting for erythromycin resistance in the presence of xylose.

The native *pbpH* allele was knocked out in bMD592 by transforming with gDNA from bMD400 and selecting for spectinomycin resistance, to give bMD627.

Construction of merodiploid *pbpA* strain

To create an IPTG-inducible allele of *pbpA*, we inserted a copy of the *pbpA* gene under the control of the Phyperspank promoter at the non-essential allele *yhdH*. We amplified: the genomic region upstream of *yhdH* from Py79 gDNA template using primers 5'-CCTGTTTCAGGTTCGGTGTATAC-3' and 5'-ACGAACGGTAGTTGACCAGTGCTCCCTGGCCAAGAACAGAAAAGAGGCGGCCTGTATGGC-3'; the *cat* resistance cassette, fused to *lacI*, and the Phyperspank promoter from a previously existing template using primers 5'-CAGGGAGCACTGGTCAAC-3' and 5'-GGTAGTTCCTCCTTAAAGCTTAATTGTTATCCGCTCACAAT-3'; the *pbpA* coding region from Py79 gDNA template using primers 5'-TAACAATTAAGCTTTAAGGAGGAACTACCATGAGGAGAAATAAACCAAAAAAGCAAAATC-3' and 5'-GAAAAGAGGCGGCCTGTATGGCCGTTAGTTATCAGAAGACGTTGTGTTTTCTG-3'; the genomic region downstream of *yhdH* from Py79 gDNA template using primers 5'-CGGCCATACAGGCCG-3' and 5'-GCTGACGGTAAAATCGGCAATATC-3'.

These fragments were combined by isothermal assembly (Gibson et al. 2009) and used to transform Py79. Colonies were selected by screening for chloramphenicol resistance to create the strain bMD563.

Generation of haploid inducible *pbpA* strains

To generate bMD572, in which the Phyperspank-*pbpA* allele was the sole source of PBP2A, we knocked out the native allele of *pbpA* in bMD563 by transforming with bEG118 gDNA and selecting for erythromycin resistance.

To generate bMD574, in which the Phyperspank-*pbpA* allele was the sole source of PBP2A, and in which PBPH was absent, we knocked out the native alleles of *pbpA* and *pbpH* in bMD563 by transforming with bEG118 gDNA and simultaneously selecting for erythromycin and spectinomycin resistance.

To generate bMD590, in which the endogenous promoter of *pbpA* was replaced with Pxyl, we amplified: region downstream of *pbpA* amplified using 5'-ATGGATCGATTAAATAGAAAAGGTGATGTTATGAGGAGAAATAAAC-3' and 5-'TTTTACAGCTGATCCCATAGCGTAG-3'; the *erm* resistance cassette fused to *xylR* fused to the Pxyl promoter amplified from a prexisting template using 5'-CAGGGAGCACTGGTCAAC-3' and 5'-GGTAGTTCCTCCTTAATCGATCCATTCAAATACAGATGCATTTTATTTC-3'; region upstream of *pbpA* using 5'-CAGCCGATAACCTTTTATTTGGCTG-3' and 5'-TACGAACGGTAGTTGACCAGTGCTCCCTGTTTACAGAAAGAAAAGACACTCAAGTA AGAG-3'. These fragments were combined by isothermal assembly (Gibson et al. 2009) and used to transform Py79, selecting for erythromycin resistance in the presence of xylose.

The native *pbpH* allele was knocked out in bMD590 by transforming with gDNA from

bMD400 and selecting for spectinomycin resistance, to give bMD597.

Combination of inducible *rodA* and *mreBCD* alleles

The strain bMD557 contains Phyperspank-*rodA* and Pxyl-*mreBCD* in addition the native copies of *rodA* and *mreBCD* was created by transforming bMD556 with gDNA prepared from bMK355, and selecting for erythromycin resistance.

Combination of inducible *pbpA* and *mreBCD* alleles

The strain bMD571 contains Phyperspank-*pbpA* and Pxyl-*mreBCD* in addition the native copies of *pbpA* and *mreBCD* was created by transforming bMD563 with gDNA prepared from bMK355, and selecting for erythromycin resistance.

Combination of inducible *rodA* and *pbpA* alleles

bEG118 was transformed with gDNA prepared from bMD592, and colonies were screened for erythromycin resistance. The resultant strain was bMD631.

Microscopy of *B. subtilis* cells

Measurements of cell diameter

Cultures were grown as described above until an OD_{600} below 0.3. Cells were stained with FM 5-95 (ThermoFisher Scientific) and then concentrated by centrifugation at 6000 x *g*. The cell pellet was resuspended in growth medium, and applied to No. 1.5 glass. All cells were imaged at 37 °C under an agar pad with the top surface exposed to air.

Measurements of single-cell growth rate

Cultures were grown as described above until an OD_{600} below 0.3. Cells were concentrated by centrifugation at 6000 x *g*. The cell pellet was resuspended in growth medium, and applied to glass bottomed dishes (MatTek Corporation). All cells were imaged at 37 °C under an agar pad with the top surface exposed to air. We used a custom-built package in MATLAB to perform segmentation on phase contrast time-lapse movies, and calculated the growth rate of the surface area of single *B. subtilis* chains.

TIRF microscopy of Halo-PBP2A

Cultures were grown as described above until an OD_{600} below 0.3. Cells were labelled with 10nM JF549 (Grimm et al. 2015) and then concentrated by centrifugation at 6000 x *g*. The cell pellet was resuspended in growth medium, and applied to No. 1.5 glass. All cells were imaged at 37 °C under an agar pad with the top surface exposed to air.

Equipment used for microscopy

Total internal reflection fluorescence microscopy (TIRF-M) and phase contrast microscopy were performed using a Nikon Eclipse Ti equipped with a Nikon Plan Apo λ 100X 1.45 objective and a Hamamatsu ORCA-Flash4.0 V2 (C11440-22CU) sCMOS camera. Microscopy was performed in a chamber heated to 37 °C.

Widefield epifluorescence microscopy, and phase contrast microscopy for single-cell growth rate measurements was performed using a Nikon Eclipse Ti equipped with a Nikon Plan Apo 100X 1.4 objective and an Andor camera. Microscopy was performed in a chamber heated

to 37 °C. Cell contours and dimensions were calculated using the Morphometrics software package (Ursell et al. 2014).

Particle tracking

Particle tracking and analysis of tracks was carried out as described in Chapter 3. All tracks with a lifetime shorter than 15 frames (that is, a duration of 5 seconds) were discarded because they could not be reliably tracked. Further, to filter for directionally moving tracks, we discarded those with a velocity lower than 0.1 nm/sec, with an R^2 lower than 0.9 for the linearity fit, and an R^2 lower than 0.95 for the linear fit to the MSD vs tau plot.

Table A.5. Bacterial strains used in this study.

Strain	Genotype	Source/Reference
PY79	WT	Garner Lab stock
bMK005	PY79 Δ*ponA::cat*	(Cho et al. 2016)
bMK355	PY79 *amyE*::P_{xyl}-*mreBCD*::*erm*	This Study
bMK385	PY79 *amyE*::P_{xyl}-*mreBCD*::*erm* Δ*mreBCD::spec pbpA::HaloTag-11aa-pbpA*	This Study
bEG118	PY79 *yhdG*::P_{spa}-*pbpA::phleo* Δ*pbpH::spec* Δ*pbpA::cat*	(Garner et al. 2011)
bGL12	PY79 *yhdH*::spec	Garner Lab stock
bGL153	Δ*pbpF* Δ*pbpG* Δ*pbpD ponA*::*kan*	(Meeske et al. 2016)
bGL155	Δ*pbpF* Δ*pbpG* Δ*pbpD amyE*::P_{hyp}-optRBS-*rodA-His10* (*spec*), *ponA*::*kan*	(Meeske et al. 2016)
bMD545	PY79 *amyE*::P_{xyl}-*mreBCD*::*erm* Δ*mreBCD::spec*	This Study
bMD554	PY79 *yhdH*:: P_{hyp}-*ponA*::*cat*	This Study
bMD556	PY79 *yhdH*:: P_{hyp}-*rodA*::*cat*	This Study
bMD557	PY79 *yhdH*:: P_{hyp}-*rodA*::*cat amyE*::P_{hyp}-*mreBCD*::*erm*	This Study
bMD563	PY79 *yhdH*:: P_{hyp}-*pbpA*::*cat*	This Study
bMD571	PY79 *yhdH*:: P_{hyp}-*pbpA*::*cat amyE*::P_{xyl}-*mreBCD*::*erm*	This Study
bMD572	PY79 *yhdH*:: P_{hyp}-*pbpA*::*cat* Δ*pbpA::erm*	This Study
bMD573	PY79 *yhdH*:: P_{hyp}-*pbpA*::*cat* Δ*pbpH::spec*	This Study
bMD574	PY79 *yhdH*:: P_{hyp}-*pbpA*::*cat* Δ*pbpA::erm* Δ*pbpH::spec*	This Study
bMD580	PY79 *yhdH*:: P_{hyp}-*rodA*::*cat* Δ*rodA::kan*	This Study
bMD590	PY79 *pbpA*:: P_{xyl}-*pbpA*::*erm*	This Study
bMD592	PY79 *rodA*:: P_{xyl}-*rodA*::*erm*	This Study

Table A.5. (continued) Bacterial strains used in this study.

Strain	Genotype	Source/Reference
bMD594	PY79 *yhdH*:: P_{spa}-*ponA*::*cat*	This Study
bMD597	PY79 *pbpA*:: P_{xyl}-*pbpA*::*erm* Δ*pbpH::spec*	This Study
bMD598	PY79 *yhdH*:: P_{spa}-*ponA*::*cat* Δ*ponA::kan*	This Study
bMD620	PY79 *amyE*::P_{xyl}-*mreBCD*::*erm* Δ*mreBCD::spec yhdH*:: P_{spa}-*ponA*::*cat* Δ*ponA::kan*	This Study
bMD622	PY79 *amyE*::P_{xyl}-*mreBCD*::*erm yhdH*:: P_{spa}-*ponA*::*cat* Δ*ponA::kan*	This Study
bMD627	PY79 *rodA*:: P_{xyl}-*rodA*::*erm* Δ*pbpH::spec*	This Study
bMD631	PY79 *rodA*:: P_{xyl}-*rodA*::*erm yhdG*::P_{spa}-*pbpA::phleo* Δ*pbpH::spec*	This Study

P_{xyl} refers to the P_{xylose} inducible promoter, P_{spa} refers to the IPTG-inducible P_{spank} promoter, and P_{hyp} refers to the IPTG-inducible $P_{hyperspank}$ promoter.

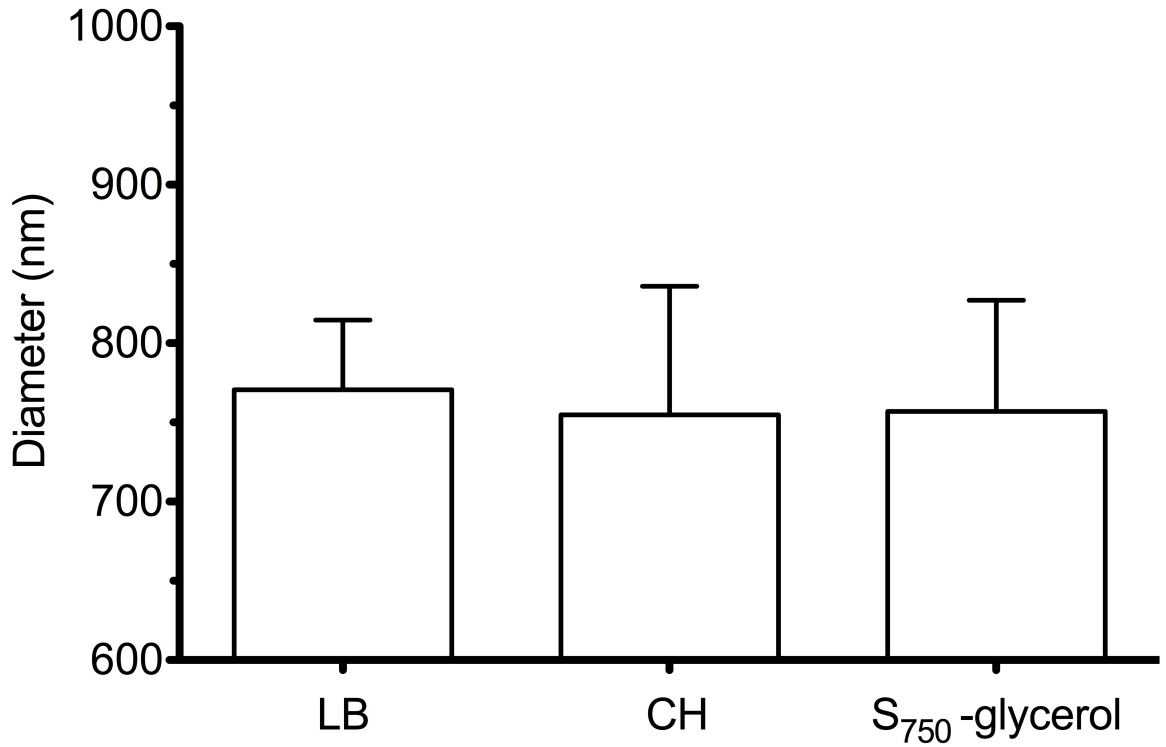


Figure A.12. Cell diameter of *B. subtilis* in different growth media. The steady state diameter of *B. subtilis* in exponential phase in three different media was measured by performing FM-595 staining and widefield epifluorescence microscopy. Error bars represent standard deviation.

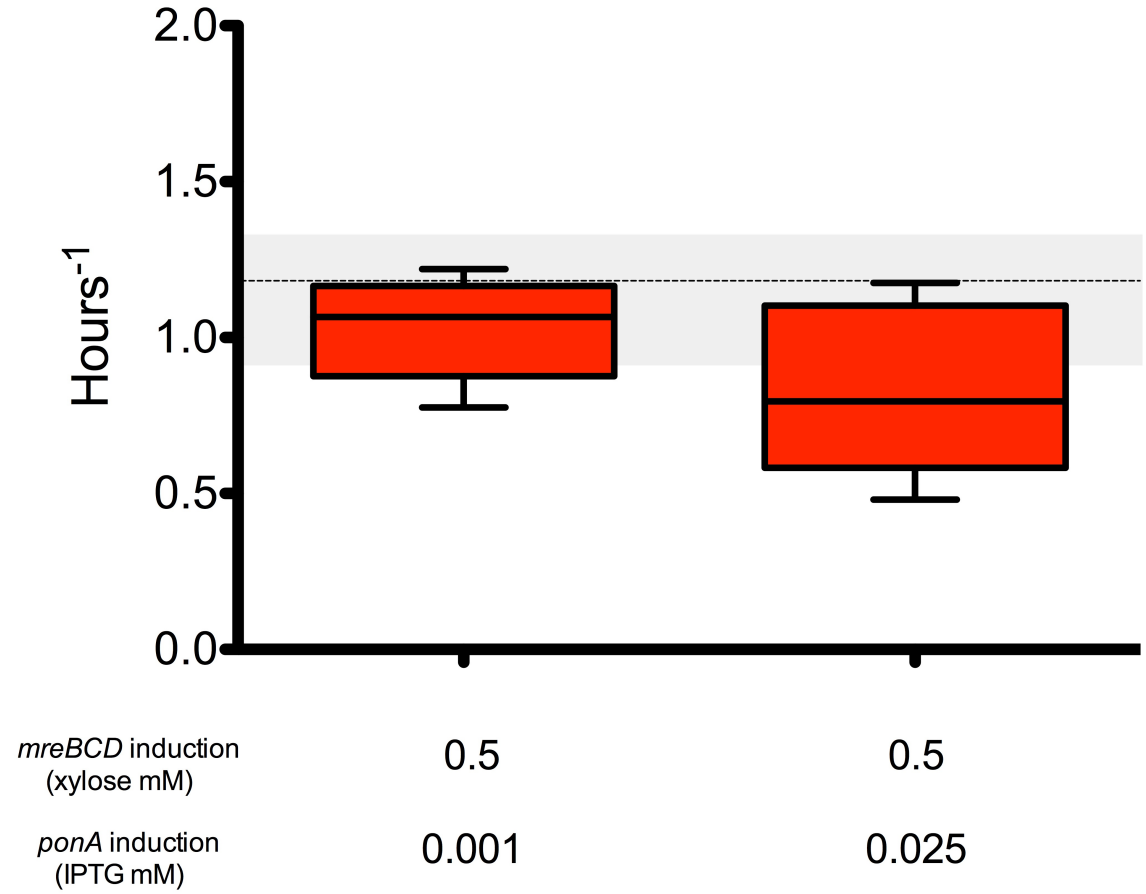


Figure A.13. An imbalance between aPBPs and the Rod system can cause growth defects. When both *mreBCD* and *ponA* expression levels are low, a slight imbalance between them can lead to a growth defect. The dashed line and gray shaded areas represent the mean and 10^{th}-90^{th} percentile of the data respectively for PY79 cells.

REFERENCES

Adams, D.W. & Errington, Jeff, 2009. Bacterial cell division: assembly, maintenance and disassembly of the Z ring. *Nature Reviews Microbiology*, 7(9), pp.642–653.

Addinall, S.G. et al., 2005. New temperature-sensitive alleles of ftsZ in Escherichia coli. *Journal of bacteriology*, 187(1), pp.358–365.

Anderson, D.E., Gueiros-Filho, F.J. & Erickson, H.P., 2004. Assembly dynamics of FtsZ rings in Bacillus subtilis and Escherichia coli and effects of FtsZ-regulating proteins. *Journal of bacteriology*, 186(17), pp.5775–5781.

Arumugam, S. et al., 2012. Surface topology engineering of membranes for the mechanical investigation of the tubulin homologue FtsZ. *Angewandte Chemie (International ed. in English)*, 51(47), pp.11858–11862.

Askenazi, M., Parikh, J.R. & Marto, J.A., 2009. mzAPI: a new strategy for efficiently sharing mass spectrometry data. *Nature methods*, 6(4), pp.240–241.

Aylett, C.H.S. & Löwe, J., 2012. Superstructure of the centromeric complex of TubZRC plasmid partitioning systems. *Proceedings of the National Academy of Sciences of the United States of America*, 109(41), pp.16522–16527.

Baba, T. et al., 2006. Construction of Escherichia coli K-12 in-frame, single-gene knockout mutants: the Keio collection. *Molecular Systems Biology*, 2, p.2006.0008.

Banzhaf, M. et al., 2012. Cooperativity of peptidoglycan synthases active in bacterial cell elongation. *Molecular microbiology*, 85(1), pp.179–194.

Barrett, D. et al., 2007. Analysis of glycan polymers produced by peptidoglycan glycosyltransferases. *The Journal of biological chemistry*, 282(44), pp.31964–31971.

Bean, G.J. & Amann, K.J., 2008. Polymerization properties of the Thermotoga maritima actin MreB: roles of temperature, nucleotides, and ions. *Biochemistry*, 47(2), pp.826–835.

Becker, E. et al., 2006. DNA segregation by the bacterial actin AlfA during Bacillus subtilis growth and development. *The EMBO journal*, 25(24), pp.5919–5931.

Bi, E.F. & Lutkenhaus, J., 1991. FtsZ ring structure associated with division in Escherichia coli. *Nature*, 354(6349), pp.161–164.

Bisicchia, P. et al., 2013. MinC, MinD, and MinE drive counter-oscillation of early-cell-division proteins prior to Escherichia coli septum formation. *MBio*, 4(6), pp.e00856–13.

Cabeen, M.T. & Jacobs-Wagner, C., 2010. The bacterial cytoskeleton. *Annual review of genetics*, 44(1), pp.365–392.

Campbell, C.S. & Mullins, R.D., 2007. In vivo visualization of type II plasmid segregation: bacterial actin filaments pushing plasmids. 179(5), pp.1059–1066. Available at: http://www.jcb.org/cgi/doi/10.1083/jcb.200708206.

Carballido-Lopez, R. et al., 2006. Actin homolog MreBH governs cell morphogenesis by localization of the cell wall hydrolase LytE. *Developmental cell*, 11(3), pp.399–409.

Cavalier-Smith, T., 2014. The neomuran revolution and phagotrophic origin of eukaryotes and cilia in the light of intracellular coevolution and a revised tree of life. *Cold Spring Harbor Perspectives in Biology*, 6(9), p.a016006.

Chastanet, A. & Carballido-Lopez, R., 2012. The actin-like MreB proteins in Bacillus subtilis: a new turn. *Frontiers in bioscience (Scholar edition)*, 4, pp.1582–1606.

Chen, Y. et al., 2005. A rapid fluorescence assay for FtsZ assembly indicates cooperative assembly with a dimer nucleus. *Biophysical journal*, 88(1), pp.505–514.

Cho, H. et al., 2016. Bacterial cell wall biogenesis is mediated by SEDS and PBP polymerase families functioning semi-autonomously. *Nature Microbiology*, 1, p.16172.

Cho, H. et al., 2011. Nucleoid occlusion factor SlmA is a DNA-activated FtsZ polymerization antagonist. *Proceedings of the National Academy of Sciences of the United States of America*, 108(9), pp.3773–3778.

Cho, H., Uehara, T. & Bernhardt, T.G., 2014. Beta-lactam antibiotics induce a lethal malfunctioning of the bacterial cell wall synthesis machinery. *Cell*, 159(6), pp.1300–1311.

Curtis, N.A. et al., 1979. Affinities of penicillins and cephalosporins for the penicillin-binding proteins of Escherichia coli K-12 and their antibacterial activity. *Antimicrobial agents and chemotherapy*, 16(5), pp.533–539.

Dam, M. & Gerdes, K., 1994. Partitioning of plasmid R1. Ten direct repeats flanking the parA promoter constitute a centromere-like partition site parC, that expresses incompatibility. *Journal of molecular biology*, 236(5), pp.1289–1298.

Daniel, R.A. & Errington, Jeff, 2003. Control of cell morphogenesis in bacteria: two distinct ways to make a rod-shaped cell. *Cell*, 113(6), pp.767–776.

Datsenko, K.A. & Wanner, B.L., 2000. One-step inactivation of chromosomal genes in Escherichia coli K-12 using PCR products. *Proceedings of the National Academy of Sciences*, 97(12), pp.6640–6645.

De Pedro, M.A. & Schwarz, U., 1981. Heterogeneity of newly inserted and preexisting murein in the sacculus of Escherichia coli. *Proceedings of the National Academy of Sciences*, 78(9), pp.5856–5860.

Defeu Soufo, H.J. & Graumann, P.L., 2004. Dynamic movement of actin-like proteins within bacterial cells. *EMBO reports*, 5(8), pp.789–794.

Denome, S.A. et al., 1999. Escherichia coli mutants lacking all possible combinations of eight penicillin binding proteins: viability, characteristics, and implications for peptidoglycan synthesis. *Journal of bacteriology*, 181(13), pp.3981–3993.

Derman, A.I. et al., 2009. Phylogenetic analysis identifies many uncharacterized actin-like proteins (Alps) in bacteria: regulated polymerization, dynamic instability and treadmilling in Alp7A. *Molecular microbiology*, 73(4), pp.534–552.

Desmarais, S.M. et al., 2015. High-throughput, Highly Sensitive Analyses of Bacterial Morphogenesis Using Ultra Performance Liquid Chromatography. *Journal of Biological Chemistry*, 290(52), pp.31090–31100.

Divakaruni, A.V. et al., 2005. The cell-shape protein MreC interacts with extracytoplasmic proteins including cell wall assembly complexes in Caulobacter crescentus. *Proceedings of the National Academy of Sciences*, 102(51), pp.18602–18607.

Doi, M. et al., 1988. Determinations of the DNA sequence of the mreB gene and of the gene products of the mre region that function in formation of the rod shape of Escherichia coli cells. *Journal of bacteriology*, 170(10), pp.4619–4624.

Domínguez-Escobar, J. et al., 2011. Processive movement of MreB-associated cell wall biosynthetic complexes in bacteria. *Science*, 333(6039), pp.225–228.

Duman, R. et al., 2013. Structural and genetic analyses reveal the protein SepF as a new membrane anchor for the Z ring., 110(48), pp.E4601–10. Available at: http://eutils.ncbi.nlm.nih.gov/entrez/eutils/elink.fcgi?dbfrom=pubmed&id=24218584&retmode=ref&cmd=prlinks.

Dye, N.A. et al., 2011. Mutations in the nucleotide binding pocket of MreB can alter cell curvature and polar morphology in Caulobacter. *Molecular microbiology*, 81(2), pp.368–394.

Egan, A.J.F. & Vollmer, W., 2013. The physiology of bacterial cell division. *Annals of the New York Academy of Sciences*, 1277, pp.8–28.

Emami, K. et al., 2017. RodA as the missing glycosyltransferase in Bacillus subtilis and antibiotic discovery for the peptidoglycan polymerase pathway. *Nature Microbiology*, 2, p.16253.

Erickson, H.P., 1995. FtsZ, a prokaryotic homolog of tubulin? *Cell*, 80(3), pp.367–370.

Erickson, H.P. et al., 1996. Bacterial cell division protein FtsZ assembles into protofilament sheets and minirings, structural homologs of tubulin polymers. *Proceedings of the National Academy of Sciences*, 93(1), pp.519–523.

Erickson, H.P., Anderson, D.E. & Osawa, M., 2010. FtsZ in bacterial cytokinesis: cytoskeleton and force generator all in one. *Microbiology and molecular biology reviews : MMBR*, 74(4), pp.504–528.

Errington, Jeffery, 2003. Dynamic proteins and a cytoskeleton in bacteria. *Nature cell biology*, 5(3), pp.175–178.

Esue, O., Wirtz, D. & Tseng, Y., 2006. GTPase activity, structure, and mechanical properties of filaments assembled from bacterial cytoskeleton protein MreB. *Journal of bacteriology*, 188(3), pp.968–976.

Eun, Y.-J. et al., 2015. Bacterial filament systems: towards understanding their emergent behavior and cellular functions. *Journal of Biological Chemistry*.

Fay, A., Meyer, P. & Dworkin, J., 2010. Interactions between late-acting proteins required for peptidoglycan synthesis during sporulation. *Journal of molecular biology*, 399(4), pp.547–561.

Ficarro, S.B. et al., 2009. Improved electrospray ionization efficiency compensates for diminished chromatographic resolution and enables proteomics analysis of tyrosine signaling in embryonic stem cells. *Analytical chemistry*, 81(9), pp.3440–3447.

Fraipont, C. et al., 2011. The integral membrane FtsW protein and peptidoglycan synthase PBP3 form a subcomplex in Escherichia coli. ... *microbiology*, 157(Pt 1), pp.251–259.

Fu, G. et al., 2010. In vivo structure of the E. coli FtsZ-ring revealed by photoactivated localization microscopy (PALM). *PloS one*, 5(9), p.e12682.

Garber, K., 2015. A β-lactamase inhibitor revival provides new hope for old antibiotics. *Nature Reviews Drug Discovery*, 14(7), pp.445–447.

Garner, E.C. et al., 2011. Coupled, circumferential motions of the cell wall synthesis machinery and MreB filaments in B. subtilis. *Science*, 333(6039), pp.222–225.

Garner, E.C. et al., 2007. Reconstitution of DNA segregation driven by assembly of a prokaryotic actin homolog. *Science*, 315(5816), pp.1270–1274.

Garner, E.C., Campbell, C.S. & Mullins, R.D., 2004. Dynamic instability in a DNA-segregating prokaryotic actin homolog. *Science*, 306(5698), pp.1021–1025.

Gayathri, P. et al., 2012. A bipolar spindle of antiparallel ParM filaments drives bacterial plasmid segregation. *Science*, 338(6112), pp.1334–1337.

Geissler, B., Shiomi, D. & Margolin, W., 2007. The ftsA* gain-of-function allele of Escherichia coli and its effects on the stability and dynamics of the Z ring. ... *microbiology*, 153(Pt 3), pp.814–825.

Gibson, D.G. et al., 2009. Enzymatic assembly of DNA molecules up to several hundred kilobases. *Nature methods*, 6(5), pp.343–345.

Gitai, Z., 2005. The New Bacterial Cell Biology: Moving Parts and Subcellular Architecture. *Cell*.

Goley, E.D. et al., 2011. Assembly of the Caulobacter cell division machine. *Molecular microbiology*, 80(6), pp.1680–1698.

Graumann, P.L. & Defeu Soufo, H.J., 2004. An intracellular actin motor in bacteria? *BioEssays : news and reviews in molecular, cellular and developmental biology*, 26(11), pp.1209–1216.

Grimm, J.B. et al., 2015. A general method to improve fluorophores for live-cell and single-molecule microscopy. *Nature methods*, 12(3), pp.244–50– 3 p following 250.

Guberman, J.M. et al., 2008. PSICIC: noise and asymmetry in bacterial division revealed by computational image analysis at sub-pixel resolution. *PLoS computational biology*, 4(11), p.e1000233.

Gundogdu, M.E. et al., 2011. Large ring polymers align FtsZ polymers for normal septum formation., 30(3), pp.617–626. Available at: http://eutils.ncbi.nlm.nih.gov/entrez/eutils/elink.fcgi?dbfrom=pubmed&id=21224850&retmode=ref&cmd=prlinks.

Harold, F.M., 2007. Bacterial morphogenesis: learning how cells make cells. *Current Opinion in Microbiology*, 10(6), pp.591–595.

Harris, L.K., Dye, N.A. & Theriot, J.A., 2014. A Caulobacter MreB mutant with irregular cell shape exhibits compensatory widening to maintain a preferred surface area to volume ratio. *Molecular microbiology*.

Henriques, A.O. et al., 1998. Control of cell shape and elongation by the rodA gene in Bacillus subtilis. *Molecular microbiology*, 28(2), pp.235–247.

Holden, S.J. et al., 2014. High throughput 3D super-resolution microscopy reveals Caulobacter crescentus in vivo Z-ring organization. *Proceedings of the National Academy of Sciences of the United States of America*, 111(12), pp.4566–4571.

Hoskins, J. et al., 1999. Gene disruption studies of penicillin-binding proteins 1a, 1b, and 2a in Streptococcus pneumoniae. *Journal of bacteriology*, 181(20), pp.6552–6555.

Höltje, J.V., 1996. A hypothetical holoenzyme involved in the replication of the murein sacculus of Escherichia coli. ... *microbiology*, 142 (Pt 8), pp.1911–1918.

Höltje, J.V., 1998. Growth of the stress-bearing and shape-maintaining murein sacculus of Escherichia coli. *Microbiology and molecular biology reviews : MMBR*, 62(1), pp.181–203.

Hörger, I. et al., 2008. FtsZ bacterial cytoskeletal polymers on curved surfaces: the importance of lateral interactions., 94(11), pp.L81–3. Available at: http://eutils.ncbi.nlm.nih.gov/entrez/eutils/elink.fcgi?dbfrom=pubmed&id=18359798&retmode=ref&cmd=prlinks.

Jaqaman, K. et al., 2008. Robust single-particle tracking in live-cell time-lapse sequences. *Nature methods*, 5(8), pp.695–702.

Jones, L.J., Carballido-Lopez, R. & Errington, J., 2001. Control of cell shape in bacteria: helical, actin-like filaments in Bacillus subtilis. *Cell*, 104(6), pp.913–922.

Kawai, Y., Daniel, R.A. & Errington, J., 2009. Regulation of cell wall morphogenesis in Bacillus subtilis by recruitment of PBP1 to the MreB helix. *Molecular microbiology*, 71(5), pp.1131–1144.

Kim, S.Y. et al., 2006. Single molecules of the bacterial actin MreB undergo directed treadmilling motion in Caulobacter crescentus. *Proceedings of the National Academy of Sciences of the United States of America*, 103(29), pp.10929–10934.

Kirchhausen, T., 2012. Bending membranes. *Nature cell biology*, 14(9), pp.906–908.

Koch, A.L., 2000. The bacterium's way for safe enlargement and division. *Applied and environmental microbiology*, 66(9), pp.3657–3663.

Kraemer, J.A. et al., 2012. A phage tubulin assembles dynamic filaments by an atypical mechanism to center viral DNA within the host cell. *Cell*, 149(7), pp.1488–1499.

Lan, G. et al., 2009. Condensation of FtsZ filaments can drive bacterial cell division. *Proceedings of the National Academy of Sciences of the United States of America*, 106(1), pp.121–126.

Landgraf, D. et al., 2012. Segregation of molecules at cell division reveals native protein localization. *Nature methods*, 9(5), pp.480–482.

Larsen, R.A. et al., 2007. Treadmilling of a prokaryotic tubulin-like protein, TubZ, required for plasmid stability in Bacillus thuringiensis. *Genes & development*, 21(11), pp.1340–1352.

Leaver, M. & Errington, Jeff, 2005. Roles for MreC and MreD proteins in helical growth of the cylindrical cell wall in Bacillus subtilis. *Molecular microbiology*, 57(5), pp.1196–1209.

Lebar, M.D. et al., 2014. Reconstitution of peptidoglycan cross-linking leads to improved fluorescent probes of cell wall synthesis. *Journal of the American Chemical Society*, 136(31), pp.10874–10877.

Lee, J.-C. & Stewart, G.C., 2003. Essential nature of the mreC determinant of Bacillus subtilis. *Journal of bacteriology*, 185(15), pp.4490–4498.

Lee, T.K. et al., 2014. A dynamically assembled cell wall synthesis machinery buffers cell growth. *Proceedings of the National Academy of Sciences of the United States of America*.

Li, Z. et al., 2007. The structure of FtsZ filaments in vivo suggests a force-generating role in cell division. *The EMBO journal*, 26(22), pp.4694–4708.

Ling, L.L. et al., 2015. A new antibiotic kills pathogens without detectable resistance. *Nature*.

Loose, M. & Mitchison, T.J., 2014. The bacterial cell division proteins FtsA and FtsZ self-

organize into dynamic cytoskeletal patterns. *Nature cell biology*, 16(1), pp.38–46.

Loose, M. et al., 2008. Spatial regulators for bacterial cell division self-organize into surface waves in vitro. *Science*, 320(5877), pp.789–792.

Löwe, J. & Amos, L.A., 1998. Crystal structure of the bacterial cell-division protein FtsZ. *Nature*, 391(6663), pp.203–206.

Lu, C., Reedy, M. & Erickson, H.P., 2000. Straight and curved conformations of FtsZ are regulated by GTP hydrolysis. *Journal of bacteriology*, 182(1), pp.164–170.

Ma, X., Ehrhardt, D.W. & Margolin, W., 1996. Colocalization of cell division proteins FtsZ and FtsA to cytoskeletal structures in living Escherichia coli cells by using green fluorescent protein. *Proceedings of the National Academy of Sciences*, 93(23), pp.12998–13003.

Margolin, W., 1998. A green light for the bacterial cytoskeleton. *Trends in Microbiology*, 6(6), pp.233–238.

Mayer, J.A. & Amann, K.J., 2009. Assembly properties of the Bacillus subtilis actin, MreB. *Cell motility and the cytoskeleton*, 66(2), pp.109–118.

McKenna, M., 2013. Antibiotic resistance: the last resort. *Nature*, 499(7459), pp.394–396.

McPherson, D.C. & Popham, D.L., 2003. Peptidoglycan synthesis in the absence of class A penicillin-binding proteins in Bacillus subtilis. *Journal of bacteriology*, 185(4), pp.1423–1431.

Meeske, A.J. et al., 2015. MurJ and a novel lipid II flippase are required for cell wall biogenesis in Bacillus subtilis. *Proceedings of the National Academy of Sciences of the United States of America*.

Meeske, A.J. et al., 2016. SEDS proteins are a widespread family of bacterial cell wall polymerases. *Nature*, 537(7622), pp.634–638.

Meier, E.L. & Goley, E.D., 2014. Form and function of the bacterial cytokinetic ring. *Current opinion in cell biology*, 26, pp.19–27.

Michie, K.A. et al., 2006. Trapping of a spiral-like intermediate of the bacterial cytokinetic protein FtsZ. *Journal of bacteriology*, 188(5), pp.1680–1690.

Mohammadi, T. et al., 2011. Identification of FtsW as a transporter of lipid-linked cell wall precursors across the membrane. *The EMBO journal*, 30(8), pp.1425–1432.

Montabana, E.A. & Agard, D.A., 2014. Bacterial tubulin TubZ-Bt transitions between a two-stranded intermediate and a four-stranded filament upon GTP hydrolysis. *Proceedings of the National Academy of Sciences of the United States of America*, 111(9), pp.3407–3412.

Muchová, K., Chromiková, Z. & Barák, I., 2013. Control of Bacillus subtilis cell shape by RodZ.

Environmental microbiology, 15(12), pp.3259–3271.

Mukherjee, A. & Lutkenhaus, J., 1994. Guanine nucleotide-dependent assembly of FtsZ into filaments. *Journal of bacteriology*, 176(9), pp.2754–2758.

Murray, T., Popham, D.L. & Setlow, P., 1998. Bacillus subtilis cells lacking penicillin-binding protein 1 require increased levels of divalent cations for growth.

Møller-Jensen, J. et al., 2003. Bacterial mitosis: ParM of plasmid R1 moves plasmid DNA by an actin-like insertional polymerization mechanism. *Molecular cell*, 12(6), pp.1477–1487.

Møller-Jensen, J. et al., 2007. Structural analysis of the ParR/parC plasmid partition complex. *The EMBO journal*, 26(20), pp.4413–4422.

Niu, L. & Yu, J., 2008. Investigating intracellular dynamics of FtsZ cytoskeleton with photoactivation single-molecule tracking. *Biophysical journal*, 95(4), pp.2009–2016.

Nurse, P. & Marians, K.J., 2013. Purification and characterization of Escherichia coli MreB protein. *Journal of Biological Chemistry*, 288(5), pp.3469–3475.

Olshausen, P.V. et al., 2013. Superresolution imaging of dynamic MreB filaments in B. subtilis--a multiple-motor-driven transport? *Biophysical journal*, 105(5), pp.1171–1181.

Orlova, A. et al., 2007. The structure of bacterial ParM filaments. *Nature structural & molecular biology*, 14(10), pp.921–926.

Osawa, M. & Erickson, H.P., 2011. Inside-out Z rings - constriction with and without GTP hydrolysis. 81(2), pp.571–579. Available at: http://doi.wiley.com/10.1111/j.1365-2958.2011.07716.x.

Osawa, M., Anderson, D.E. & Erickson, H.P., 2009. Curved FtsZ protofilaments generate bending forces on liposome membranes. *The EMBO journal*, 28(22), pp.3476–3484.

Osawa, M., Anderson, D.E. & Erickson, H.P., 2008. Reconstitution of contractile FtsZ rings in liposomes. *Science*, 320(5877), pp.792–794.

Paik, J. et al., 1999. Mutational analysis of the Streptococcus pneumoniae bimodular class A penicillin-binding proteins. *Journal of bacteriology*, 181(12), pp.3852–3856.

Park, J.T. & Uehara, T., 2008. How bacteria consume their own exoskeletons (turnover and recycling of cell wall peptidoglycan). *Microbiology and molecular biology reviews : MMBR*, 72(2), pp.211–27– table of contents.

Pazos, M., Peters, K. & Vollmer, W., 2017. Robust peptidoglycan growth by dynamic and variable multi-protein complexes. *Current Opinion in Microbiology*, 36, pp.55–61.

Petek, N.A. & Mullins, R.D., 2014. Bacterial actin-like proteins: purification and characterization of self-assembly properties. *Methods in enzymology*, 540, pp.19–34.

Poggio, S. et al., 2010. A protein critical for cell constriction in the Gram-negative bacterium Caulobacter crescentus localizes at the division site through its peptidoglycan-binding LysM domains., 77(1), pp.74–89. Available at: http://eutils.ncbi.nlm.nih.gov/entrez/eutils/elink.fcgi?dbfrom=pubmed&id=20497503&retmode=ref&cmd=prlinks.

Polka, J.K. et al., 2009. The Structure and Assembly Dynamics of Plasmid Actin AlfA Imply a Novel Mechanism of DNA Segregation. *Journal of bacteriology*, 191(20), pp.6219–6230.

Polka, J.K., Kollman, J.M. & Mullins, R.D., 2014. Accessory factors promote AlfA-dependent plasmid segregation by regulating filament nucleation, disassembly, and bundling. *Proceedings of the National Academy of Sciences of the United States of America*, 111(6), pp.2176–2181.

Popham, D.L. & Setlow, P., 1996. Phenotypes of Bacillus subtilis mutants lacking multiple class A high-molecular-weight penicillin-binding proteins. *Journal of bacteriology*, 178(7), pp.2079–2085.

Raskin, D.M. & de Boer, P.A., 1999. Rapid pole-to-pole oscillation of a protein required for directing division to the middle of Escherichia coli., 96(9), pp.4971–4976. Available at: http://eutils.ncbi.nlm.nih.gov/entrez/eutils/elink.fcgi?dbfrom=pubmed&id=10220403&retmode=ref&cmd=prlinks.

Reimold, C. et al., 2013. Motion of variable-length MreB filaments at the bacterial cell membrane influences cell morphology. *Molecular biology of the cell*, 24(15), pp.2340–2349.

Renner, L.D. et al., 2013. Studying biomolecule localization by engineering bacterial cell wall curvature. *PloS one*, 8(12), p.e84143.

Rice, L.B. et al., 2009. Role of class A penicillin-binding proteins in the expression of beta-lactam resistance in Enterococcus faecium. *Journal of bacteriology*, 191(11), pp.3649–3656.

Romberg, L., Simon, M. & Erickson, H.P., 2001. Polymerization of Ftsz, a bacterial homolog of tubulin. Is assembly cooperative? *The Journal of biological chemistry*, 276(15), pp.11743–11753.

Rudner, D.Z. & Losick, R., 2010. Protein Subcellular Localization in Bacteria. *Cold Spring Harbor Perspectives in Biology*, 2(4), pp.a000307–a000307.

Rueff, A.-S. et al., 2014. An early cytoplasmic step of peptidoglycan synthesis is associated to MreB in Bacillus subtilis. *Molecular microbiology*, 91(2), pp.348–362.

Salje, J. et al., 2011. Direct membrane binding by bacterial actin MreB. *Molecular cell*, 43(3), pp.478–487.

Sauvage, E. et al., 2008. The penicillin-binding proteins: structure and role in peptidoglycan biosynthesis. *FEMS Microbiology Reviews*, 32(2), pp.234–258.

Schindelin, J. et al., 2012. Fiji: an open-source platform for biological-image analysis. *Nature methods*, 9(7), pp.676–682.

Schirner, K. et al., 2014. Lipid-linked cell wall precursors regulate membrane association of bacterial actin MreB. *Nature chemical biology*.

Schneider, C.A., Rasband, W.S. & Eliceiri, K.W., 2012. NIH Image to ImageJ: 25 years of image analysis. *Nature methods*, 9(7), pp.671–675.

Schumacher, M.A. et al., 2007. Segrosome structure revealed by a complex of ParR with centromere DNA. 450(7173), pp.1268–1271. Available at: http://www.nature.com/doifinder/10.1038/nature06392.

Sham, L.-T. et al., 2014. Bacterial cell wall. MurJ is the flippase of lipid-linked precursors for peptidoglycan biogenesis. *Science*, 345(6193), pp.220–222.

Sharpe, M.E. et al., 1998. Bacillus subtilis cell cycle as studied by fluorescence microscopy: constancy of cell length at initiation of DNA replication and evidence for active nucleoid partitioning. *Journal of bacteriology*, 180(3), pp.547–555.

Shih, Y.-L., Kawagishi, I. & Rothfield, L., 2005. The MreB and Min cytoskeletal-like systems play independent roles in prokaryotic polar differentiation. *Molecular microbiology*, 58(4), pp.917–928.

Si, F. et al., 2013. Organization of FtsZ filaments in the bacterial division ring measured from polarized fluorescence microscopy. *Biophysical journal*, 105(9), pp.1976–1986.

Smith, T.J., Blackman, S.A. & Foster, S.J., 2000. Autolysins of Bacillus subtilis: multiple enzymes with multiple functions. ... *microbiology*, 146(2), pp.249–262.

Stachowiak, J.C. et al., 2012. Membrane bending by protein-protein crowding. *Nature cell biology*, 14(9), pp.944–949.

Sung, M.-T. et al., 2009. Crystal structure of the membrane-bound bifunctional transglycosylase PBP1b from Escherichia coli. *Proceedings of the National Academy of Sciences of the United States of America*, 106(22), pp.8824–8829.

Swulius, M.T. et al., 2011. Long helical filaments are not seen encircling cells in electron cryotomograms of rod-shaped bacteria. *Biochemical and biophysical research communications*, 407(4), pp.650–655.

Szwedziak, P. et al., 2014. Architecture of the ring formed by the tubulin homologue FtsZ in bacterial cell division. *eLife*, 4.

Szwedziak, P. et al., 2012. FtsA forms actin-like protofilaments. *The EMBO journal*, 31(10), pp.2249–2260.

Tan, Q., Awano, N. & Inouye, M., 2011. YeeV is an Escherichia coli toxin that inhibits cell

division by targeting the cytoskeleton proteins, FtsZ and MreB. *Molecular microbiology*, 79(1), pp.109–118.

Thanbichler, M. & Shapiro, L., 2006. MipZ, a spatial regulator coordinating chromosome segregation with cell division in Caulobacter., 126(1), pp.147–162. Available at: http://eutils.ncbi.nlm.nih.gov/entrez/eutils/elink.fcgi?dbfrom=pubmed&id=16839883&retmode=ref&cmd=prlinks.

Tinsley, E. & Khan, S.A., 2006. A novel FtsZ-like protein is involved in replication of the anthrax toxin-encoding pXO1 plasmid in Bacillus anthracis. *Journal of bacteriology*, 188(8), pp.2829–2835.

Tropini, C. et al., 2014. Principles of bacterial cell-size determination revealed by cell-wall synthesis perturbations. *Cell reports*, 9(4), pp.1520–1527.

Typas, A. et al., 2012. From the regulation of peptidoglycan synthesis to bacterial growth and morphology. *Nature Reviews Microbiology*, 10(2), pp.123–136.

Uehara, T. & Park, J.T., 2008. Growth of Escherichia coli: significance of peptidoglycan degradation during elongation and septation. *Journal of bacteriology*, 190(11), pp.3914–3922.

Ursell, T.S. et al., 2014. Rod-like bacterial shape is maintained by feedback between cell curvature and cytoskeletal localization. *Proceedings of the National Academy of Sciences of the United States of America*, 111(11), pp.E1025–34.

Vadia, S. & Levin, P.A., 2015. Growth rate and cell size: a re-examination of the growth law. *Current Opinion in Microbiology*, 24, pp.96–103.

van den Ent, F. et al., 2010. Bacterial actin MreB assembles in complex with cell shape protein RodZ. *The EMBO journal*, 29(6), pp.1081–1090.

van den Ent, F. et al., 2014. Bacterial actin MreB forms antiparallel double filaments M. Laub, ed. *eLife*, 3, p.e02634.

van den Ent, F., Amos, L.A. & Löwe, J., 2001. Prokaryotic origin of the actin cytoskeleton. *Nature*, 413(6851), pp.39–44.

van Teeffelen, S. et al., 2011. The bacterial actin MreB rotates, and rotation depends on cell-wall assembly. *Proceedings of the National Academy of Sciences of the United States of America*, 108(38), pp.15822–15827.

Varma, A., De Pedro, M.A. & Young, K.D., 2007. FtsZ directs a second mode of peptidoglycan synthesis in Escherichia coli. *Journal of bacteriology*, 189(15), pp.5692–5704.

Vollmer, W. & Seligman, S.J., 2010. Architecture of peptidoglycan: more data and more models. *Trends in Microbiology*, 18(2), pp.59–66.

Vollmer, W., Blanot, D. & De Pedro, M.A., 2008. Peptidoglycan structure and architecture. *FEMS Microbiology Reviews*, 32(2), pp.149–167.

Vrljic, M. et al., 2002. Translational diffusion of individual class II MHC membrane proteins in cells. *Biophysical journal*, 83(5), pp.2681–2692.

Wang, S. et al., 2014. Characterization and development of photoactivatable fluorescent proteins for single-molecule-based superresolution imaging. *Proceedings of the National Academy of Sciences of the United States of America*, 111(23), pp.8452–8457.

Warming, S. et al., 2005. Simple and highly efficient BAC recombineering using galK selection. *Nucleic acids research*, 33(4), p.e36.

White, C.L., Kitich, A. & Gober, J.W., 2010. Positioning cell wall synthetic complexes by the bacterial morphogenetic proteins MreB and MreD. *Molecular microbiology*, 76(3), pp.616–633.

Wu, L.J. & Errington, Jeff, 2012. Nucleoid occlusion and bacterial cell division. *Nature Reviews Microbiology*, 10(1), pp.8–12.

Yakhnina, A.A. & Gitai, Z., 2012. The small protein MbiA interacts with MreB and modulates cell shape in Caulobacter crescentus. *Molecular microbiology*, 85(6), pp.1090–1104.

Young, K.D., 2007. Bacterial morphology: why have different shapes? *Current Opinion in Microbiology*, 10(6), pp.596–600.

Young, K.D., 2010. Bacterial Shape: Two-Dimensional Questions and Possibilities. *Annual Review of Microbiology*, 64(1), pp.223–240.

Yousif, S.Y., Broome-Smith, J.K. & Spratt, B.G., 1985. Lysis of Escherichia coli by beta-lactam antibiotics: deletion analysis of the role of penicillin-binding proteins 1A and 1B. *Journal of general microbiology*, 131(10), pp.2839–2845.

Yu, D. et al., 2000. An efficient recombination system for chromosome engineering in Escherichia coli. *Proceedings of the National Academy of Sciences*, 97(11), pp.5978–5983.

Zehr, E.A. et al., 2014. The structure and assembly mechanism of a novel three-stranded tubulin filament that centers phage DNA. *Structure (London, England : 1993)*, 22(4), pp.539–548.

Zieske, K. & Schwille, P., 2014. Reconstitution of self-organizing protein gradients as spatial cues in cell-free systems. *eLife*, 3.